# University of Crete

---

# Advanced Single-Photon Sources Based on Innovative Semiconductor Nanostructures

---

*by*

Nikolaos G. Chatzarakis

*Submitted to*

Department of Materials Science and Technology

*In fulfillment of the requirements*
*for the degree of Doctor of Philosophy*

Supervisor

Prof. Nikolaos T. Pelekanos

September 2023

Heraklion, Greece

# Advanced Single-Photon Sources Based on Innovative Semiconductor Nanostructures

Thesis author: Nikolaos G. Chatzarakis

Principal Advisor: Prof. Nikolaos T. Pelekanos

Examination committee: Prof. Kopidakis George
Dr. Deligeorgis George
Prof. Kafesaki Maria
Prof. Kioseoglou George
Prof. Iliopoulos Eleftherios
Dr. Emmanouil Dimakis

Department of Materials Science and Technology

University of Crete

September 2023

Heraklion, Greece

# Abstract

In a rapidly evolving technological world, where quantum information processing will soon become a necessity, an ideal artificial quantum system that offers great potential in manipulating the electronic properties of matter, is the semiconductor quantum dot (QD). Quantum information processing and quantum computing developments depend crucially on the availability of efficient, controllable, and cost-effective sources of single and entangled photons. In this thesis, having in mind to develop practical QD-based single photon emitters, operating at non-cryogenic temperatures with enhanced characteristics, we have focused on self-assembled InAs/GaAs QDs grown by molecular beam epitaxy in the Stranski-Krastanov growth mode on (211)B GaAs substrates. This QD system combines all the benefits of (100) InAs/GaAs QDs with another important feature, which is the presence of a large piezoelectric (PZ) field along the growth axis of the QDs. One of the advantages that the PZ field offers is that the symmetry of the confinement potential is maintained inside the QD, leading to small fine-structure splittings, something essential for producing entangled photons. In addition, due to the PZ field, large exciton-biexciton splittings are generated, making this system suitable for high-temperature single photon applications. In our case, to achieve high-temperature operation, the InAs/GaAs QDs were incorporated in between GaAs/AlAs short-period superlattices. The resulting strong confinement of the carriers in the dots, drastically improved the temperature stability of the photoluminescence and allowed for single-photon emission at the elevated temperature of 230K. This is a high enough temperature, allowing for the first time, the noncryogenic operation of a single-photon emitter based on III-arsenide QDs. Furthermore, the multi-exciton lines of these strongly-confined InAs QDs have been thoroughly characterized. The observed redshifts of the biexciton and trion lines were attributed to the strong confinement and accompanying correlation effects. Our results suggest an attractive mechanism to tailor the transition energies of a single semiconductor QD by appropriate band-gap engineering of the surrounding barriers. It is important to note that this mechanism not only relates to the particular case of (211)B InAs QDs, but can be applied to any semiconductor QD system, including for instance the standard (100) InAs/GaAs QDs.

An alternative way to make high-efficiency nano-emitters is the utilization of the plasmonic effect. Hybrid plasmonic nano-systems have been receiving great

attention in the last 10-15 years, as they are able to provide significant enhancements in the optical properties of the nano emitters when they come in proximity of a metal. Although great progress has been made to understand how the plasmons interact with an emitter, there are still open questions and practical difficulties such as the control of the relative position of the nano emitter with respect to the metal, that require complex processing techniques. Here, the interaction between a nanowire emitter and a gold surface is experimentally studied as a function of their relative distance. Epitaxially grown GaAs/AlGaAs and GaAs/InAlAs core-shell nanowires are used as emitters, positioned on relatively flat gold surfaces of prepatterned templates. To controllably increase the emitter-metal distance, a Hafnia ($HFO_2$) layer of varying thickness deposited by Atomic Layer Deposition, is used as spacer. A strong enhancement of the photoluminescence intensity (up to a factor of 40) is observed when the nanowire is lying directly on the metal surface, accompanied by a strong reduction of the carrier recombination lifetime by a factor of 2, that we interpret as due to the interaction between the nanowire emitter and surface plasmons.

As prospective work of this thesis, we performed a quantum-confined Stark effect study on single $CsPbBr_3$ nanocrystals. This nanocrystal system is particularly promising for cost-effective high-temperature nanophotonic applications, as these nanocrystals are chemically-synthesized and solution-processed, and exhibit excellent quantum yields (close to unity) and single photon emission at room temperature. In our study, we only observed tiny Stark shifts, suggesting that some very efficient screening mechanism exists in our nanocrystals. Finally, we demonstrated an alternative photon-collection scheme using half-ball lenses, increasing the collection efficiencies by a factor between 2 and 6, depending on the specifics of the emitter's dielectric environment.

# Acknowledgements

It was an unforgettable experience to complete my PHD thesis at FORTH, in the Microelectronics Research Group under the supervision of Prof. Nikolaos T. Pelekanos. He taught me many things about quantum optics, but more importantly he taught me how to do proper research by thinking out of the box every time a difficulty strikes. I also thank him because every single time he was there for me for every kind of problem I had. It was a great honor for me to collaborate with many great scientists such as, Dr. George Deligeorgis, Dr. George Konstantinidis, Dr. Emmanouil Dimakis, Prof. Maksym Kovalenko, Dr. Gabriele Raino from groups in Greece, Germany and Switzerland giving me the opportunity to exchange knowledge and ideas, helping me go further towards my final research goal.

I would like to thank every member of the MRG group (current or former) that I have collaborated with, but especially I would like to thank Maria Androulidaki for all the kinds of support that she has provided to me over the years, Ioannis Thyris for teaching me every last experimental detail at the beginning of my thesis, Yianis Balas for spending many hours talking about science and having fun doing our research, Thanasis Kostopoulos, Antonios and George Stavrinidis for all the sample processing, Katerina Tsagaraki for providing me with excellent SEM pictures and Maria Kayabaki for helping me with any kind of electrical measurements.

Also, I would like to thank Nikolaos Papadakis, Michael Sfendourakis and Emmanouil Verikokidis for the technical support all these years, regarding the experimental equipment in the laboratory. Their help proved “life-saving” in many difficult situations.

Finally, I would like to say a big thank you to my family for supporting me all these years in every possible way and also special thanks to Christina Siaitanidou for being there for me in every single moment of this journey.

# Contents

# List of Abbreviation

| | |
|---|---|
| QD | Quantum dot |
| $E_g$ | Energy Band Gap |
| DOS | Density of states |
| QW | Quantum well |
| NW | Nano Wire |
| NC | Nano Crystal |
| 1D, 2D, 3D | One, Two and Three dimensional |
| MBE | Molecular Beam Epitaxy |
| SK | Stranski Krastanov growth method |
| PZ | Piezoelectric or Piezoelectricity |
| FSS | Fine Structure Splitting |
| QCSE | Quantum Confined Stark Effect |
| PL | Photoluminescence |
| μPL | Micro-Photoluminescence |
| SP | Surface Plasmon |
| SPP | Surface Plasmon Polariton |
| LSP | Localized Surface Plasmon |
| LDOS | Local Density of Photonic states |
| MHP | Metal Halide Perovskites |
| LED | Light Emitting Diode |
| WL | Wetting Layer |
| SSL | Short Period Superlattice |

# Table of figures

# 1 Introduction

## 1.1 Introduction to quantum dots

Semiconductor technology is one of the most rapidly evolving scientific fields with significant contribution to nanoscale research. We live in a constantly evolving world where further knowledge of semiconductors can lead to higher performance and smaller devices in electronic, photonic, and optoelectronic applications. The need of ease of transport, processing power and storage capacity is continuously growing, pushing the size limits further and further. Already typical structure sizes in microprocessors are in the range of nanometers, where there are billions of transistors integrated in a single circuit. As the size of transistors decreases, quantum effects start to become dominant, and a physical limit is about to be reached. An ideal quantum laboratory to study the fundamental properties of semiconductors in the nanoscale is the semiconductor quantum dots (QDs). A semiconductor QD is a nanosized semiconductor structure embedded in a matrix of another semiconductor material with a wider band gap. There are different fabrication techniques for QDs involving lithography, chemical synthesis and self-assembly by epitaxial growth techniques. The latter technique is used the most, because of its flexibility, control, and the possibility to use a big variety of semiconductor alloys during the growth, covering the full spectral range from ultraviolet to near infrared.

### 1.1.1 Band structure

Quantum dots are nanosized particles of a semiconductor with energy band gap $E_g^1$ embedded in the matrix of a higher band gap $E_g^2$ semiconductor. In general, QDs can be considered as a reduced dimensionality system. In contrast with bulk semiconductors, the carriers inside a reduced dimensional system are spatially confined in one or all three dimensions. Every semiconductor has a different Bohr radius for its charge carriers. When the size of the semiconductor crystallite becomes smaller than this radius, the mobility of the carriers is limited inside the matrix and quantum confinement effects start to become dominant.

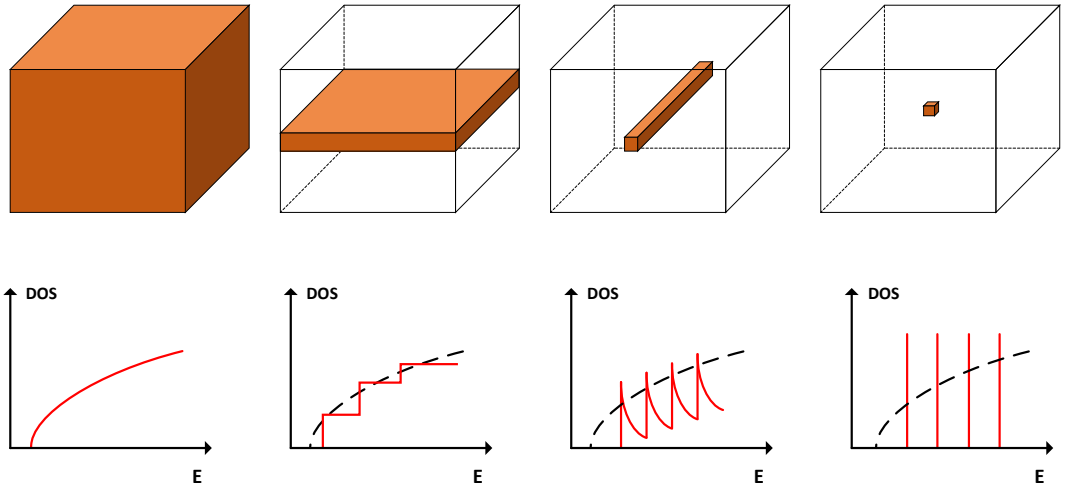


*Figure 1.1: Schematic illustration for the density of states (DOS) of a bulk semiconductor, quantum well, quantum wire and quantum dot. The quantum dot has discrete DOS while in the other three cases is continuous.*

Nanostructures can be classified in three categories according to their number of confined dimensions: Quantum wells (QWs), where the carriers are confined in one dimension along the growth axis and are free to move in the planar region, Quantum wires or nanowires (NWs), where the carriers are confined in two dimensions and can move only in one dimension (along the wire axis) and quantum dots (QDs) where the carriers are confined in all three dimensions. As a result, QWs can be characterized as two-dimensional (2D), Quantum wires as one-dimensional (1D) and QDs as zero-dimensional (0D) system respectively. In **Figure 1.1** the density of states (DOS) of each reduced-dimensionality system is shown. In the case of quantum well and nanowire nanostructure the DOS is continuous where in quantum dot is very similar to delta function. This implies that the carriers inside the QD have discrete energy levels, similar to an atom.

### 1.1.2 Quasiparticles inside a QD

In **Figure 1.2** the energy band diagram of a QD is depicted where a potential well is formed because of the band discontinuity between two different materials. Carriers can be pumped when non-resonant excitation occurs above the band gap $E_g^1$ and "fall" into the quantum well with band gap $E_g^2$. If an electron hole pair is generated, the two opposite charges are attracted by their Coulomb interaction and the two carriers are captured inside the QD potential well forming an electron-hole pair which is a quasiparticle called **exciton (X)**. Discrete energy states are formed inside the QD confinement potential, whose energy positions depend on the carrier effective masses,

the confinement potential, and the morphology of the QD. For n=0 quantum number, the electrons and holes in the QD are in ground state ($e_0$, $h_0$) and for n=1, 2,.. are in excited states ($e_1$, $h_1$ , $e_2$, $h_2$,…).

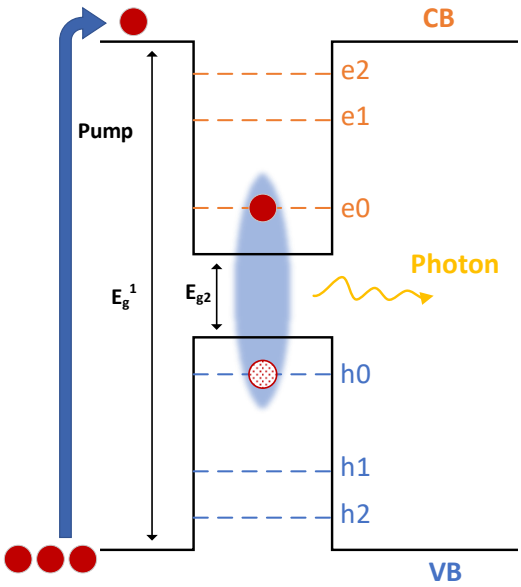


*Figure 1.2: Schematic illustration of one dimensional QD electronic structure where carriers are pumped after non resonant excitation and relaxation inside the potential well.*

In general, there are two types of excitons according to the strength of the Coulomb interaction between the electron and hole. When the interaction is strong, we get the Frenkel exciton which can be found in materials with small dielectric constants such as alkali halide crystals and inorganic molecular crystals. On the other hand, for weakly-bound electron-holes there is the Wannier-Mott exciton, which is of interest to this work.

To describe a two-particle system such as an electron and a hole in the conduction and valence band respectively we can use a Hamiltonian H:

$$H = H_e + H_h \qquad 1\text{-}1$$

When the electron and hole bind together to form a bound exciton state the Hamiltonian $H_X$ taking into account Coulomb interaction can be written as follows,

$$H_X = H_e + H_h + H_{coulomb} \qquad 1\text{-}2$$

The energy of a bound exciton state is lower than the energy of a free electron-hole pair and the energy difference is called the exciton binding energy, often called exciton Rydberg energy ($R_y$). By using the effective mass approximation, the exciton transition energy in a bulk semiconductor is given by:

$$E_X(n) = E_g - \frac{R_y}{n^2} \qquad 1\text{-}3$$

Where n=1,2,.. is the quantum number of the exciton state, $R_y(n) = \frac{\mu e^2}{2\hbar^2 \varepsilon^2}$ is the Rydberg energy required to ionize the exciton, where $\mu$ is the reduced mass and $\varepsilon$ is the dielectric constant.

QDs also referred as artificial atoms, follow Pauli's exclusion principle, according to which two electrons at most, with opposite spins, can occupy the conduction band ground state. If we have two confined electrons in the conduction band and two holes in the valence band, a new quasiparticle is formed which is called **biexciton (XX)**.

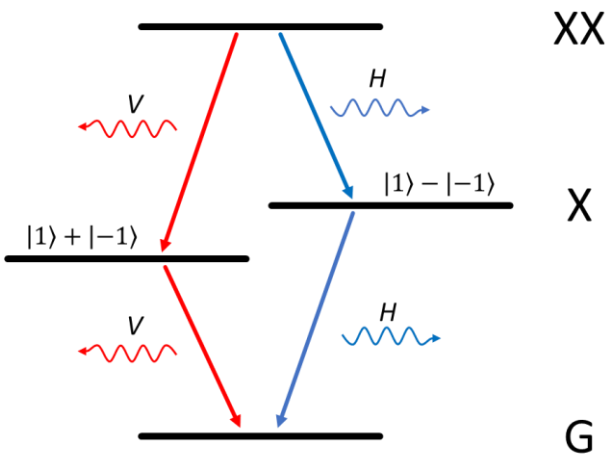


*Figure 1.3: Schematic of biexciton (XX) cascade emission through the intermediate exciton (X) state which generates a polarized photon pair (vertical or horizontal polarization) due to the presence of exchange interaction. The two paths are distinguishable because of the fine structure splitting (FSS).*

**Figure 1.3** shows the recombination paths of a biexciton inside a QD. The XX decays to the X state, through the recombination of one electron-hole pair, emitting a photon of energy $\hbar\omega_{XX}$. Finally, the remaining electron-hole pair can recombine normally emitting a photon of energy $\hbar\omega_X$. The energy difference between $\hbar\omega_X$ and $\hbar\omega_{XX}$ is

called biexciton binding energy, which is typically non-zero as the recombination of the first electron-hole pair takes place under the influence of the other two carriers and differs from the simple exciton recombination. The total process leads to the generation of a linearly polarized photon pair based on the splitting of the intermediate exciton state caused by the presence of Fine-Structure Splitting (FSS) which is discussed later in this chapter.

There are also other occupation combinations in the QD ground state that involves odd number of electrons and holes. These quasiparticles are called trions, involving a combination of either two electrons and one hole resulting to a negatively-charged exciton or **negative trion ($X^-$)**, or two holes and one electron leading to a positively charged exciton or **positive trion ($X^+$)**. Both recombine radiatively and emit photons with energy $\hbar\omega_{X^-}$ and $\hbar\omega_{X^+}$, respectively. The lines of these quasiparticles are frequently present in single QD spectra and their identification is relatively simple.

### 1.1.3 Fabrication method

In this thesis, we focus mainly on epitaxially grown QDs and their optoelectronic properties. The piezoelectric QDs are grown by molecular beam epitaxy (MBE) with Stranski-Krastanov (SK) method on (211)B GaAs substrates. The letter B indicates that the crystal is terminated with the As face. In this method, different materials with a lattice mismatch between them, are deposited on top of each other. In our case, the InAs and GaAs lattice mismatch is about 7%. The growth starts by depositing InAs on top of GaAs and after reaching a critical thickness, which in our case is ~1.4ML, the formation of InAs islands begins due to the elastic relaxation caused by the mechanical stress that GaAs applies to the InAs. The thus epitaxially grown QDs take the shape of truncated pyramids with typical base diameter of ~15-20nm and thickness of ~1.5-2.5nm. There are some critical conditions that contribute to the optical properties of the grown QDs. One of the main parameters is the substrate temperature which changes before the InAs QD growth from 620˚C to 480˚C, in order to form InAs QDs along the (211B) orientation. Also, the flux of the materials should be carefully controlled. The combination of growth parameters can affect the shape and size of the QDs and also define the number of Ga atoms that exchange places with In atoms, strongly affecting the optical properties. Finally, optimal growth conditions determine

the crystal purity of the InAs/GaAs interface during growth, reducing the non-radiative recombination centers. Detailed growth conditions will be given in the next chapters.

### 1.1.4 Piezoelectric effect

The main attribute of the (211) QDs that we used is piezoelectricity. This characteristic is manifested as an intrinsic piezoelectric field along the growth direction when heterostructure QDs are grown on a (211) GaAs substrate. Here, we briefly explain why the piezoelectric effect is created and how this affects the optoelectronic properties of the QDs. The (211) crystallographic orientation of Zinc Blende structure belongs to the family of high index (N11) crystallographic orientations, which are able to produce piezoelectric field when strain is applied to the system **Figure 1.4** shows schematically how piezoelectricity appears in such high index crystallographic orientations.

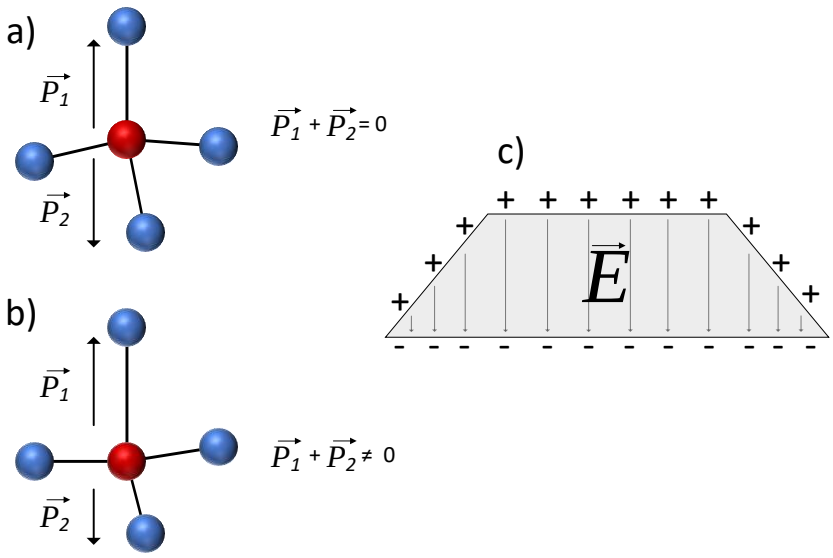


*Figure 1.4: (a) Tetrahedron from a zinc-blende structure under no stress where the total polarization is zero. (b) Perturbed tetrahedron geometry under epitaxial stress resulting to nonzero total polarization. The tetrahedra of this schematic are oriented along the (111) orientation, but similar effect occur in (211) or (N11) configurations (c) The positive charges of the dipole chain inside the bulk QD cancel out the negative charge from the adjacent ones, leading only to surface charges on the surface of the QD producing piezoelectric field.*

When InAs QDs are epitaxially grown on a high-index polar GaAs substrate, a mechanical deformation of the III-V covalent bonds of InAs is created due to the strain, generated by the lattice mismatch of these different materials. This deformation creates a net polarization along the growth axis. In a zinc blende unit cell, when no strain is applied to the lattice, the III-V ions form a tetrahedron. As **Figure 1.4a** shows, the total

contribution of the three bottom bonds cancels the contribution from the top, resulting to zero total net polarization. This balance is changed radically when lattice-mismatch induced strain is applied, as the four bonds are now deformed, and an induced dipole moment is created along the (111) direction of the tetrahedron shown in **Figure 1.4b**. The case of the (211) direction follows the same logic, as the (211) orientation differs from the (111) orientation by an angle of φ=19.5º explaining schematically the presence of piezoelectric field in our quantum dots.

In **Figure 1.4c**, we assume that a large number of dipoles exist in a QD structure along the growth direction. In each dipole, the positive charge is compensated by the negative charge of the adjacent dipole in the lattice of a piezoelectric quantum dot. As a result, only surface charges are created at the base and the apex of the QD with opposite sign giving rise to piezoelectric field. Such a field is predicted to be maximum in the (111) orientation and slightly weaker (60% of the (111) value) for the (211) [1]. However, the fabrication of (111) QDs is complex and requires special growth methods [2,3]. In order to understand in depth how the piezoelectric effect is generated in strained heterostructures, one must take into account the ionic and electronic response to the applied strain as well [4]. However, the simple pictorial model of **Figure 1.4** provides a good base to understand how piezoelectricity is created in high index (N11) crystallographic orientations.

### 1.1.5 Fine Structure Splitting (FSS)

The exciton energy levels inside the QD are determined by the spin configurations of electrons and holes. The exciton state is formed by the superposition of an electron and a heavy hole with angular momentum of $J_e = \pm\frac{1}{2}$ and $J_h = \pm\frac{3}{2}$ respectively. Two types of excitons can be produced with total angular momentum $M_{dark} = \pm 2$ (dark state) and $M_{bright} = \pm 1$ (bright state) [5]. An exciton in the bright state ($M = \pm 1$) decays radiatively and a photon of spin $\pm 1$ is emitted. On the other hand, the dark state ($M = \pm 2$) cannot emit photons. These four states are normally degenerate but under the influence of electron hole exchange interaction, the bright states split from the dark states leading to bright ($|1\rangle \pm |-1\rangle$) and dark ($|2\rangle \pm |-2\rangle$) doublets. When there is anisotropy in the confinement potential the degeneracy of the bright doublet is lifted, leading to two different well defined energy states as **Figure**

**1.5b** shows. The energy difference between the bright exciton states is the Fine Structure Splitting (FSS) which is a measure of the confinement of symmetry inside the quantum dot. The biexciton cannot have a fine structure splitting, because the total spin of the carriers is zero. Furthermore, the FFS of a positively and negatively charged exciton state is zero as well, because each charge state can be considered as an electron or hole interacting with a spin-singlet electron-hole pair [6].

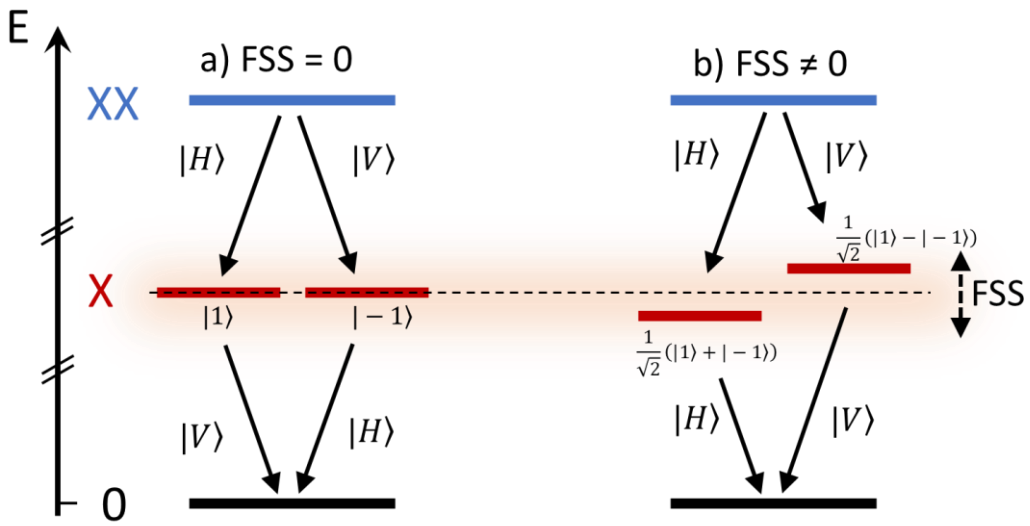


*Figure 1.5: Schematic illustration of the XX-X cascade emission a) in the absence of FSS, where the recombination paths become indistinguishable creating entangled photon pairs and b) when FSS is non-zero the X level is split removing the "which-path" uncertainty.*

The fine structure splitting is very important in the biexciton cascade because it creates two identifiable well-defined recombination paths if the value is nonzero (**Figure 1.5b**). Each path produces photons with the same polarization in the linear basis and is perpendicular to the polarization of the other path. In the case where the FSS is zero, these two paths become indistinguishable and the produced photons are polarization-entangled (**Figure 1.5a**), which is crucial for applications in quantum optics and quantum communication experiments.

### 1.1.6 Quantum Confined Stark Effect

The quantum-confined Stark effect (QCSE) describes the effect of an external electric field to the absorption and emission properties of a quantum well. Electrons and holes inside the QW occupy discrete energy levels with energy difference at the ground states, $E_1$. When external electric field is applied there is a band bending of the

conduction and valence bands as **Figure 1.6** shows. This separates spatially the electrons and holes, decreasing the overlap integral and oscillator strength of the corresponding transitions. Also, the energy difference of the electron and hole ground states decreases resulting to a new reduced band gap $E_1' < E_1$ and a redshift of transition energy [7].

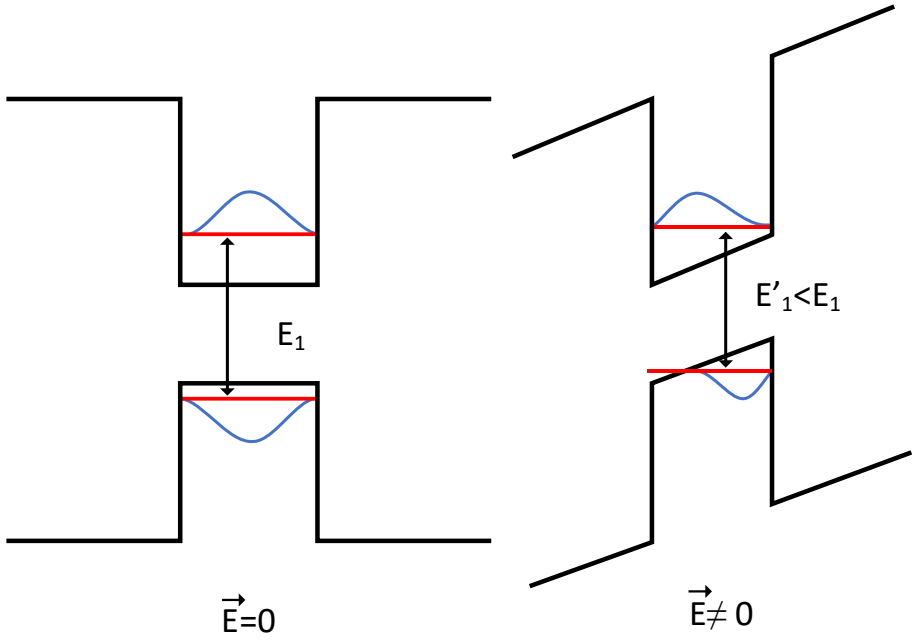


*Figure 1.6: Schematic illustration of the quantum confined stark effect (QCSE). The external electric field causes band bending and the electron and hole wavefunctions are realigned causing changes to the transition energy.*

In the (211)B PZ QDs of this work there is enhanced quantum confined stark effect originating from the built-in PZ field. This results to all the prementioned QCSE effects without the use of external electric field. Moreover, one can expect the biexciton transition energy to be at higher energies than the exciton transition energy due to the increased screening of carriers [8] resulting to **negative biexciton binding energies**. This effect can be also attributed to the repulsive Coulomb interactions of the electron-electron and hole-hole quasiparticles which is larger than the electron-hole attraction. In (111) and (211)B InAs/GaAs QDs the internal PZ fields are expected to be in the order of hundreds kV/cm [9] resulting to large biexciton antibinding energies.

### 1.1.7 Single photon emission at elevated temperatures

In order to have single photon emission (SPE) at high temperatures, the energy difference $\Delta E$ between the exciton and biexciton should be larger than the

homogeneous linewidth of each emission line at the same temperature. If this condition is met then the two lines can be distinguished at elevated temperatures.

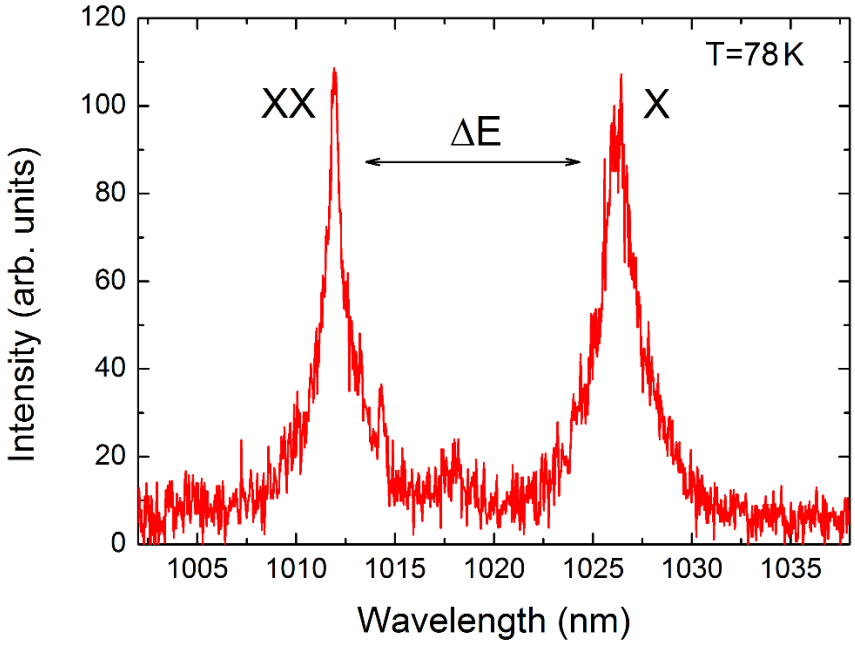


*Figure 1.7: μPL spectrum from a single PZ QD. The energy difference is much larger than the linewidths and the X line does not interfere with the XX at 78K.*

A typical value for the homogeneous linewidth for a GaAs exciton at room temperature is about ~6-7meV. The GaAs-based systems are well studied over the years contrarily to the Nitride systems. Nitride based systems present larger piezoelectric fields but their drawback is that they cannot be easily electrically injected, unlike the GaAs ones. In the next chapter, especially designed PZ QDs are studied and their Photoluminescence (PL) and single photon emission results are discussed. Also, for the first time single photon emission is recorded up to 230K.

## 1.2 Introduction to Plasmonics

Plasmonics is the intersection of materials science and electromagnetism and focuses on the study of plasmons. From the classical perspective, plasmons are collective excitations of the free-electron gas density with respect to the fixed positive ions inside a metal. At metallic surfaces plasmons have the ability to couple with the electromagnetic waves, giving rise to surface plasmon polaritons (SPPs) [10–12]. One of

the most interesting properties of surface plasmons is their ability to confine light beyond the limit of conventional optics [13]. This feature is responsible for extreme field enhancements [14,15], modification of emitter decay and excitation rates [16]. Surface plasmon polaritons propagate along the surface of the metal and can exchange energy with the emitter. The properties of the surface plasmons depend strongly on the dielectric functions of the metal that supports them and the surrounding material. During the last decades great effort has been made to manipulate the emitter properties in the vicinity of metallic properties, such as the fluorescence intensity and recombination dynamics of the carriers despite the lack of clear understanding how exactly plasmons interact with the emitter. In many works, complex hybrid metal-emitter structures have been realized and the effect of plasmons has been studied in order to clearly understand this interaction. In this work, a simple hybrid structure approach is followed in order to investigate the plasmonic effect in the emission of NWs coupled to a metallic surface.

### 1.2.1 Surface plasmons and surface plasmon polaritons

Metals are conductors which are a regular array of atoms. Free electrons from each atom are shared from all atoms in the material and are free to move around which is the main reason why metals are such good conductors of electricity. All free electrons in a metal can be considered as a “gas” which is free to move around the crystal lattice. A plasmon is a quasiparticle which can be described as a collective oscillation of the electrons. A special category of plasmons are those that occur at the surface of the metal. They can be described as collective oscillations of the surface electron gas. Surface plasmons (SPs) were first predicted by R.H Ritchie *et al.* [17] and extensively studied by many researchers. Any interaction or energy transfer by means of SPs can be categorized as “plasmonics” [18]. For a closed surface of a small metallic particle, we refer to “localized surface plasmons (LSPs).

The charge motion of an SP at a metal - dielectric interface coupled with electromagnetic waves travelling parallel to the interface outside the metal constitute a new quasiparticle termed the “surface plasmon polariton” (SPP). The simplest form of a SPP is an electromagnetic excitation that propagates like a wave along the metal-dielectric interface as shown in **Figure 1.8** and its amplitude decays exponentially in both media with the distance from the interface [19–21]. This makes the SPP a quasiparticle

with confined electromagnetic field near the vicinity of the interface, leading to an enhancement of the electromagnetic field amplitude. For that reason, the SPPs are very sensitive to the surface conditions (shape, roughness).

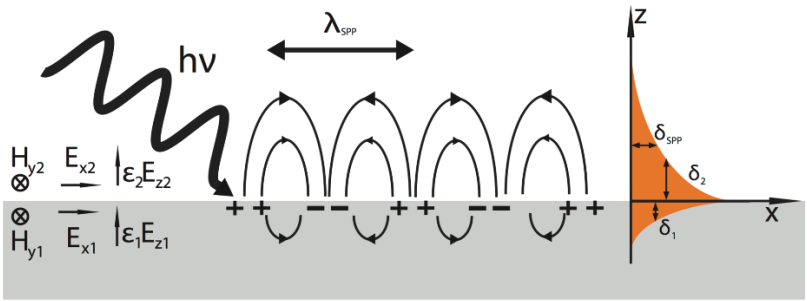


*Figure 1.8: Left Schematic illustration of the electron density wave that propagates along the interface of the metal/dielectric. Right The intensity of the propagating electromagnetic field is exponentially dependent on the distance away from the interface [wiki]*

SPPs can be excited by photons or electrons. For photonic excitation, both photon and SPP should in principle have the same momentum and frequency. However, the momentum of a free space photon with frequency ω, is less than the momentum of the SPP because of their different dispersion relations. Because of their difference in momentum, a free space photon cannot be coupled directly with a SPP and for this reason an SPP from a smooth metallic surface cannot emit energy as a free space photon to the dielectric. To couple SPPs with free-space photons the usage of a coupling medium such as a prism or other dielectric medium is necessary in order to match the SPP and photon wavevectors.

### 1.2.2 Interaction between plasmons and emitters

Surface plasmons have the ability to spatially confine light, which results to a strong local field enhancement leading to enhanced emitter properties, which is beneficial for many applications.[22–26] In this section, a brief theoretical description of a hybrid system between plasmonic structures and nano-emitters is discussed.

Emission results from excited electrons at high states that relax back to the ground state by emitting a photon. This relaxation process can be divided into radiative and non-radiative transitions, depending on whether a photon is emitted or not. The total decay rate that includes all relaxation process from an excited state to the ground can be written:

$$\gamma_{tot} = \gamma_{rad} + \gamma_{nr} \qquad 1\text{-}4$$

Where $\gamma_{rad}$ is the radiative decay rate and $\gamma_{nr}$ is the non-radiative decay rate. Because relaxation is a random selection process, the radiative and non-radiative channels are competing between them.

Fluorescence quantum yield, $Y$ , can be defined as the ratio of radiative decay rate to the total decay rate. For an emitter in free space, we can define the quantum yield as follows:

$$Y^{free} = \frac{\gamma_{rad}^{free}}{\gamma_{rad}^{free} + \gamma_{nr}^{free}} \qquad 1\text{-}5$$

For excitation below saturation, the emission rate can be written as:

$$\gamma_{em} = \gamma_{ex} \cdot Y \qquad 1\text{-}6$$

Where $\gamma_{ex}$ is the excitation rate, which is given by Fermi's golden rule [27] as:

$$\gamma_{ex} = \frac{2\pi}{\hbar} |\langle f|E(\boldsymbol{r},\omega) \cdot \boldsymbol{p}|i\rangle|^2 \rho(E_f) \qquad 1\text{-}7$$

Where $\boldsymbol{p}$ is the transition dipole moment, $\langle f|E(\boldsymbol{r},\omega) \cdot \boldsymbol{p}|i\rangle$ is the transition matrix element from the initial $\boldsymbol{i}$ ground state to the final $\boldsymbol{f}$ excited state, $E(\boldsymbol{r},\omega)$ is the local field and $\rho(E_f)$ is the density of states of the final excited state. From the above equation 1-7, we can assume that the excitation rate depends on local excitation field and thus $\gamma_{ex} \propto |E(\boldsymbol{r},\omega) \cdot \boldsymbol{p}|^2$.

When a nano-emitter is placed in the vicinity of a metallic surface, the local electric field changes, because of the local surface-plasmon resonance (LSPR), affecting the excitation rate and the emission properties. This happens only if the excitation wavelength of the metal-emitter matches the surface plasmon polariton resonance (SPPR) and is thus able to generate SPPs. Also, the radiative and non-radiative decay rates can be changed, modifying the fluorescence lifetime and quantum yield. The photonic local density of states (LDOS) of the metal nanostructure, which depend on the magnitude of the enhanced electromagnetic field, can be used as possible decay channels for the nano-emitter, leading to either fluorescence enhancement or

quench,[28] depending critically on the distance between the metal and the emitter and the relative polarization direction of the dipole emitter. In case of fluorescence enhancement, this could be attributed to an increase of the excitation efficiency and an enhancement of the emission rate (Purcell effect) [29]. On the other hand, in addition to the intrinsic non-radiative channels of the emitter, there is another possible non-radiative decay channel through the energy transfer of the emitter's excited state to the metal, which can lead to PL quenching. The interaction of the emitter-plasmon will be discussed experimentally in Chapter 4.

## 1.3 Introduction to Metal halide perovskites

A large progress in understanding the properties of various nanomaterials has been accomplished over the last decades, in view of high impact applications in photovoltaics, catalysis, data storage and biotechnology[33]. During the last decade, metal halide perovskites (MHPs), an alternative semiconductor material, has emerged because of its extraordinary optical properties, especially adapted to photovoltaic applications. Their development ranges from bulk material down to small size nanoparticles whose properties are strongly size dependent opening new directions in various fields. For instance, Perovskite nanocrystals (NCs) often have greater photoluminescence properties compared to their bulk counterparts [34]. All inorganic perovskite nanocrystals such CsPbX3 (X=halide ions), have emerged as a group of promising light emitters because of their size and composition dependent tunable energy band gap, emitting light from the ultra-violet to near infrared, and exhibiting very narrow emission linewidths [35,36]. Furthermore, their ligand structure offers surface protection and tackles the current challenges of bulk perovskites regarding their stability and charge transfer processes especially in thin films where there is a large number of grain boundaries [37]. Many light-emitting diodes at various colors have been realized and their quantum efficiency is constantly increasing through device optimization [38–42]. Perovskite NCs have been studied as alternative quantum emitters only recently, since 2015. Their appealing features are the large exciton binding energies, the widely tunable band gap and the observation of single photon emission even at room temperature.[43]

### 1.3.1 Crystal structure

The term perovskite was given after L.A Perovski to a new material class with crystal structure similar to calcium titanate with chemical formula $CaTiO_3$. Metal halide perovskites have a general formula of $ABX_3$. Where A is an organic cation such as methylammonium ($MA^+$) and formamidinium ($FA^+$) or inorganic such as cesium ($Cs^+$). In B there is a metal cation such as lead or tin and X is a halide such as iodide, bromide or chloride. All the chemical components are held together by ionic bonds which is the main reason of the relatively easy fabrication of perovskites at room temperature [44]. An indication of stability and distortion of the crystal can be assessed by the Goldschmidt tolerance factor $t$, which is defined by the ratio of the ionic radius of each atomic component by following the equation:

$$t = \frac{r_A + r_X}{\sqrt{2}(r_B + r_X)} \qquad 1\text{-}8$$

Where $r_A$ is the A cation radius, $r_B$ is the B cation radius and $r_X$ is the X anion radius. For $t = 1$ the cubic structure is perfect. Metal halide perovskites have $t$ in the range of 0.9-1 to maintain a very good cubic structure with some minor geometric strains and crystal distortions. Out of this range there are other crystal forms such as hexagonal, tetragonal or orthorhombic structures [45]. For MHPs there is a limit in the number of A cations, such as Cs, MA, FA that can form a stable cubic phase.

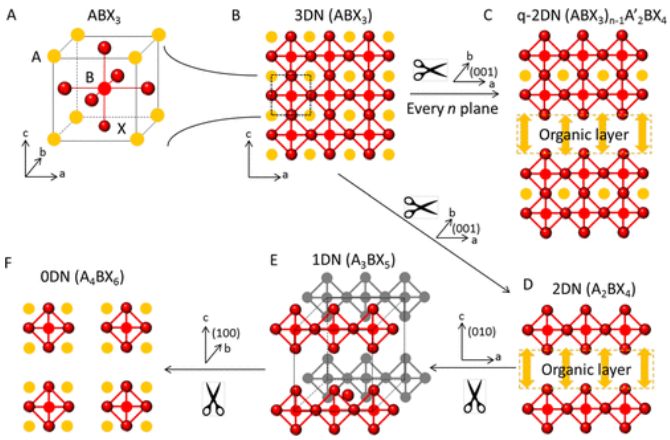


*Figure 1.9: Schematic illustration of a) cubic crystal structure of perovskite unit cell, b-f) different reduced dimensionality perovskite structures. Reprinted from [46].*

In addition to the cubic $ABX_3$ structure (3D perovskite), the cations A and anions B can be rearranged in order to form other low dimensional structures such as 2D layered perovskite, 1D or 0D (NCs) perovskites, where the cation A is sandwiched between the face and the edge of the $BX_6$ octahedral plane. A bulk perovskite can be

sliced in a specific crystallographic orientation forming a 2D perovskite structure. Further perpendicular slicing of the 2D structure can form 1D and 0D accordingly. **Figure 1.9** shows where the different perovskite structures can be sliced in order for their dimensionality to be reduced [46]. These low dimensional perovskites have larger exciton binding energy due to the strong quantum confinement which is favorable in applications that require radiative exciton recombination.

### 1.3.2 Optical properties

Metal halide perovskites (MHPs) have great optical properties which is crucial for applications in optoelectronic devices such as photovoltaic and light emitting diodes (LED). They have large absorption coefficients and their specific absorption peaks can be engineered to cover the entire visible spectrum. By changing the metal ions or halides the conduction and valence band energy positions can be changed resulting to different MHP band gaps [47–49]. The band structure can be also affected by the organic cation because the change in the A site results to different length and angle of the B-X ionic bond. For example, in $MAPbI_3$ perovskite the band gap can be changed from 1.64eV to 1.43eV by changing the MA cation with FA [50]. Furthermore, MHP exhibit very good light emitting properties with low non-radiative recombination channels [51]. Their photoluminescence quantum yield can easily approach unity (99.8%)[52] by following simple solution-process synthesis, making them very attractive for LED and laser applications [53]. Their photoluminescence peaks range from ultraviolet to near infrared according to their chemical composition. **Figure 1.10** shows perovskite solutions with different chemical formula emitting at different colors. The unique optical versatility based on their composition is the most attractive feature over the conventional semiconductor materials.

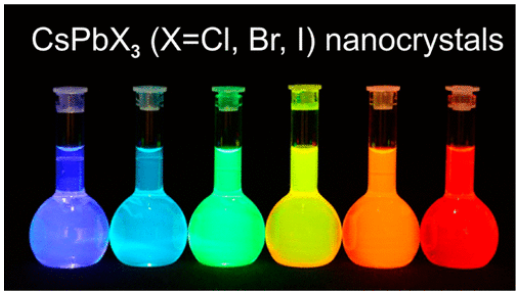


*Figure 1.10: Perovskite nanocrystals emitting different colors from ultraviolet to red by changing their halide component* [35]

# References


1. Smith, D. L. & Mailhiot, C. Piezoelectric effects in strained-layer superlattices. *J Appl Phys* **63**, 2717–2719 (1988).
2. Mohan, A. *et al.* Correction: Retraction: Polarization-entangled photons produced with high-symmetry site-controlled quantum dots. *Nat Photonics* **6**, 793–793 (2012).
3. Stock, E. *et al.* Single-photon emission from InGaAs quantum dots grown on (111) GaAs. *Appl Phys Lett* **96**, 093112 (2010).
4. Arlt, G. & Quadflieg, P. Piezoelectricity in III-V Compounds with a Phenomenological Analysis of the Piezoelectric Effect. in *January 1* 323–330 (De Gruyter, 1968). doi:10.1515/9783112496787-033.
5. Seguin, R. *et al.* Size-Dependent Fine-Structure Splitting in Self-Organized InAs/GaAs Quantum Dots. *Phys Rev Lett* **95**, 257402 (2005).
6. Bayer, M. *et al.* Fine structure of neutral and charged excitons in self-assembled In(Ga)As/(Al)GaAs quantum dots. *Phys Rev B* **65**, 195315 (2002).
7. Miller, D. A. B. *et al.* Band-Edge Electroabsorption in Quantum Well Structures: The Quantum-Confined Stark Effect. *Phys Rev Lett* **53**, 2173 (1984).
8. Dialynas, G. E. *et al.* Anti-binding of biexcitons in (211)B InAs/GaAs piezoelectric quantum dots. *Physica E Low Dimens Syst Nanostruct* **40**, 2113–2115 (2008).
9. Bester, G., Wu, X., Vanderbilt, D. & Zunger, A. Importance of second-order piezoelectric effects in zinc-blende semiconductors. *Phys Rev Lett* **96**, 187602 (2006).
10. Alexei Maradudin, J. Roy Sambles & William L. Barnes. *Modern Plasmonics, Volume 4 - 1st Edition*.
11. Maier, S. A. *Plasmonics: Fundamentals and applications*. *Plasmonics: Fundamentals and Applications* (Springer US, 2007). doi:10.1007/0-387-37825-1/COVER.
12. Gonçalves, P. A. D. & Peres, N. M. R. *An Introduction to Graphene Plasmonics*. *An Introduction to Graphene Plasmonics* (World Scientific Publishing Co. Pte. Ltd., 2016). doi:10.1142/9948/SUPPL_FILE/9948_CHAP01.PDF.
13. Barnes, W. L., Dereux, A. & Ebbesen, T. W. Surface plasmon subwavelength optics. *Nature 2003 424:6950* **424**, 824–830 (2003).
14. Schuller, J. A. *et al.* Plasmonics for extreme light concentration and manipulation. *Nature Materials 2010 9:3* **9**, 193–204 (2010).
15. Hao, E. & Schatz, G. C. Electromagnetic fields around silver nanoparticles and dimers. *J Chem Phys* **120**, 357–366 (2004).

16. Andersen, M. L., Stobbe, Sø., SØrensen, A. Sø. & Lodahl, P. Strongly modified plasmon–matter interaction with mesoscopic quantum emitters. *Nature Physics 2010 7:3* **7**, 215–218 (2010).
17. Ritchie, R. H. Plasma Losses by Fast Electrons in Thin Films. *Physical Review* **106**, 874 (1957).
18. Polman, A. & Atwater, H. A. Plasmonics: optics at the nanoscale. *Materials Today* **8**, 56 (2005).
19. Agranovich, V. M. (Vladimir M. & Mills, D. L. *Surface Polaritons : Electromagnetic Waves at Surfaces and Interfaces*. (Elsevier Science, 1982).
20. Raether, H. Surface plasmons on smooth surfaces. in 4–39 (Springer, Berlin, Heidelberg, 1988). doi:10.1007/BFB0048319.
21. Boardman, A. D. *Electromagnetic surface modes*. (Wiley, 1982).
22. Anger, P., Bharadwaj, P. & Novotny, L. Enhancement and quenching of single-molecule fluorescence. *Phys Rev Lett* **96**, 113002 (2006).
23. Akimov, A. V. *et al.* Generation of single optical plasmons in metallic nanowires coupled to quantum dots. *Nature 2007 450:7168* **450**, 402–406 (2007).
24. Bardhan, R., Grady, N. K., Cole, J. R., Joshi, A. & Halas, N. J. Fluorescence enhancement by au nanostructures: Nanoshells and nanorods. *ACS Nano* **3**, 744–752 (2009).
25. Ming, T. *et al.* Experimental evidence of plasmophores: Plasmon-directed polarized emission from gold nanorod - Fluorophore hybrid nanostructures. *Nano Lett* **11**, 2296–2303 (2011).
26. Cohen-Hoshen, E., Bryant, G. W., Pinkas, I., Sperling, J. & Bar-Joseph, I. Exciton-plasmon interactions in quantum dot-gold nanoparticle structures. *Nano Lett* **12**, 4260–4264 (2012).
27. Orear, Jay., Fermi, E., Rosenfeld, A. H. & Schluter, R. A. Nuclear physics : a course given by Enrico Fermi at the University of Chicago. 248 (1974).
28. Dong, L. *et al.* Fluorescence quenching and photobleaching in Au/Rh6G nanoassemblies: impact of competition between radiative and non-radiative decay. *J Eur Opt Soc Rapid Publ* **6**, 42 (2011).
29. Shubina, T. V. *et al.* Plasmon-induced Purcell effect in InN/In metal-semiconductor nanocomposites. *Phys Rev B Condens Matter Mater Phys* **82**, 073304 (2010).

30. Rousseaux, B., Baranov, D. G., Käll, M., Shegai, T. & Johansson, G. Quantum description and emergence of nonlinearities in strongly coupled single-emitter nanoantenna systems. *Phys Rev B* **98**, 045435 (2018).

31. Hugall, J. T., Singh, A. & Van Hulst, N. F. Plasmonic Cavity Coupling. *ACS Photonics* **5**, 43–53 (2018).

32. Carminati, R. *et al.* Electromagnetic density of states in complex plasmonic systems. *Surf Sci Rep* **70**, 1–41 (2015).

33. Wang, S. *et al.* Perovskite Nanocrystals: Synthesis, Stability, and Optoelectronic Applications. *Small Struct* **2**, 2000124 (2021).

34. Zhao, Q. *et al.* Size-Dependent Lattice Structure and Confinement Properties in CsPbI3 Perovskite Nanocrystals: Negative Surface Energy for Stabilization. *ACS Energy Lett* **5**, 238–247 (2020).

35. Protesescu, L. *et al.* Nanocrystals of Cesium Lead Halide Perovskites (CsPbX3, X = Cl, Br, and I): Novel Optoelectronic Materials Showing Bright Emission with Wide Color Gamut. *Nano Lett* **15**, 3692–3696 (2015).

36. Zhang, F. *et al.* Recent Advances and Opportunities of Lead-Free Perovskite Nanocrystal for Optoelectronic Application. *Energy Material Advances* **2021**, (2021).

37. Li, J. J. *et al.* Microscopic Investigation of Grain Boundaries in Organolead Halide Perovskite Solar Cells. *ACS Appl Mater Interfaces* **7**, 28518–28523 (2015).

38. Liu, H. *et al.* CsPbxMn1-xCl3 Perovskite Quantum Dots with High Mn Substitution Ratio. *ACS Nano* **11**, 2239–2247 (2017).

39. Du, X. *et al.* High-quality CsPbBr3 perovskite nanocrystals for quantum dot light-emitting diodes. *RSC Adv* **7**, 10391–10396 (2017).

40. Chang, Y. *et al.* All-Inorganic Perovskite Nanocrystals with a Stellar Set of Stabilities and Their Use in White Light-Emitting Diodes. *ACS Appl Mater Interfaces* **10**, 37267–37276 (2018).

41. Liang, D. *et al.* Color-Pure Violet-Light-Emitting Diodes Based on Layered Lead Halide Perovskite Nanoplates. *ACS Nano* **10**, 6897–6904 (2016).

42. Lin, K. *et al.* Perovskite light-emitting diodes with external quantum efficiency exceeding 20 per cent. *Nature 2018 562:7726* **562**, 245–248 (2018).

43. Baranowski, M. *et al.* Exciton binding energy and effective mass of $CsPbCl_3$: a magneto-optical study. *Photonics Research, Vol. 8, Issue 10, pp. A50-A55* **8**, A50–A55 (2020).

44. Shamsi, J., Urban, A. S., Imran, M., De Trizio, L. & Manna, L. Metal Halide Perovskite Nanocrystals: Synthesis, Post-Synthesis Modifications, and Their Optical Properties. *Chem Rev* **119**, 3296–3348 (2019).

45. Amat, A. *et al.* Cation-induced band-gap tuning in organohalide perovskites: Interplay of spin-orbit coupling and octahedra tilting. *Nano Lett* **14**, 3608–3616 (2014).

46. Saidaminov, M. I., Mohammed, O. F. & Bakr, O. M. Low-dimensional-networked metal halide perovskites: The next big thing. *ACS Energy Lett* **2**, 889–896 (2017).

47. Prasanna, R. *et al.* Design of low bandgap tin–lead halide perovskite solar cells to achieve thermal, atmospheric and operational stability. *Nature Energy 2019 4:11* **4**, 939–947 (2019).

48. Jin, Z. *et al.* A critical review on bismuth and antimony halide based perovskites and their derivatives for photovoltaic applications: recent advances and challenges. *J Mater Chem A Mater* **8**, 16166–16188 (2020).

49. Zhao, Y. & Zhu, K. Efficient planar perovskite solar cells based on 1.8 eV band gap CH 3NH3PbI2Br nanosheets via thermal decomposition. *J Am Chem Soc* **136**, 12241–12244 (2014).

50. Targhi, F. F., Jalili, Y. S. & Kanjouri, F. MAPbI3 and FAPbI3 perovskites as solar cells: Case study on structural, electrical and optical properties. *Results Phys* **10**, 616–627 (2018).

51. Liu, X. K. *et al.* Metal halide perovskites for light-emitting diodes. *Nature Materials 2020 20:1* **20**, 10–21 (2020).

52. Zhou, X. *et al.* Near-Unity Quantum Yield and Superior Stable Indium-Doped CsPbBrxI3−x Perovskite Quantum Dots for Pure Red Light-Emitting Diodes. *Adv Opt Mater* **10**, 2101517 (2022).

53. Dutta, A., Behera, R. K., Pal, P., Baitalik, S. & Pradhan, N. Near-Unity Photoluminescence Quantum Efficiency for All CsPbX3 (X=Cl, Br, and I) Perovskite Nanocrystals: A Generic Synthesis Approach. *Angewandte Chemie International Edition* **58**, 5552–5556 (2019).

# 2 High Temperature single photon emission from (211)PZ QDs

## 2.1 Abstract

In this chapter we will discuss about high temperature single quantum dot operation and will demonstrate single photon emission in strongly-confined piezoelectric (211)B InAs/GaAs quantum dots at the elevated temperature of 230K, exploiting the enhanced exciton-biexciton splittings in the system. This is the highest operating temperature reported so far, for a single photon emitter based on III-arsenide quantum dots. A determining factor toward this important result, was the incorporation of the quantum dot layer in between GaAs/AlAs short-period super-lattices (SSLs), which improved drastically the carrier confinement and temperature stability of the dot emission, allowing the observation of distinct exciton and biexciton emission peaks up to 260K and single photon emission at a record-high temperature.

## 2.2 Introduction

Semiconductor quantum dots (QDs) are considered ideal sources of single and entangled photons as they can emit *efficiently* and *on demand*, a single photon [1–3] or a single pair of polarization-entangled photons,[4] per excitation cycle. Focusing in particular on the former devices, ultra-bright single-photon emitters with high repetition rates and spectral purity have been demonstrated using epitaxial InAs QDs, exploiting the superior collection efficiencies and light-guiding properties of dot-in-wire [5] and micropillar [6] geometries and other photonic structures such as, circular Bragg gratings[7,8], photonic crystal waveguides[9] and microlenses[10,11]. Importantly, the InAs QDs are able to provide single photons with a high degree of indistinguishability, [6,8,10,12] a prerequisite for many quantum-processing schemes. Moreover, these sources can be readily integrated into real-world devices, addressing one or more technological issues such as, deterministic positioning of QDs in the photonic structure[6–8,10], direct coupling with fiber-optics[13,14] and implementation of electrical injection schemes[15–17], taking advantage of the highly developed III-V semiconductor micro-fabrication technology. For practical reasons, the single photon emitters “on demand” should be able to emit single photons even at high temperatures. With increasing temperature, however, the

InAs-based single photon emitters lose rapidly their brightness and single-photon purity, requiring in general cryogenic temperatures to operate and hence, the inconvenience of bulky and expensive cryo-coolers. The highest operating temperatures reported previously for single photon emission from InAs-based QDs are 120 K under optical excitation [18] and 77 K under electrical injection [19]. The main reasons for this temperature limitation are first, the small exciton-biexciton (X-XX) splittings in the system, typically of a few meV, [20–22] which undermine at elevated temperatures the single-photon purity of the exciton (X) emission by the adjacent thermally-broadened biexciton (XX) lines. Second, the relatively small energy difference, between the energy gap of the wetting layer (WL) and the QD exciton energy, $\Delta E = E_{WL} - E_{QD} \cong 100meV$, which allows for efficient thermionic emission of the QD carriers inτo the WL, leading to strong suppression of the emission intensity at elevated temperatures.

## 2.3 Semiconductor QD systems operating at room temperature

So far, single photon emission at room temperature has been achieved in other *epitaxial* QD systems, such as GaN/AlGaN dots-in-wire [23], GaN/AlN QDs [24], CdSe/ZnSe dots-in-wire [25] and CdSe/ZnSSe/MgS QDs [26]. A common characteristic of these systems is the large X-XX splittings (20-25 meV for the CdSe and 30-40 meV for the GaN QDs), which are comparable to the respective exciton homogeneous linewidths at ambient temperature, enabling the QD excitons to emit single photons with sufficient purity at high temperatures. Another feature of these systems is the generally large band-offsets and $\Delta E$-values, which are able to suppress the carrier thermionic emission out of the QDs, allowing for efficient single photon emission at elevated temperatures. Several other *non-epitaxial* systems have already been proposed in the literature as single photon emitters at room temperature, each carrying along however one or more disadvantages, such as for instance single molecules of terylene [27] suffering from photo-bleaching phenomena, nitrogen-vacancy colour centers in artificial diamond [28,29] exhibiting long radiative lifetimes and broad emission spectra, colour centres in two-dimensional hexagonal boron nitride[30] lacking so far control of the type and density of the optically active defects, and finally colloidal CdSe QDs [31] presenting significant photo-blinking, spectral diffusion effects and long spontaneous-emission lifetimes [32,33].

## 2.4 Advantages of piezoelectric InAs (211)B QDs

For this thesis, we revisit the technologically relevant case of InAs QDs and demonstrate that by appropriate band-gap engineering of the QD surroundings, it is possible to obtain efficient single photon emission up to the elevated temperature of 230 K. It should be noted that this is a *non-cryogenic* temperature, in the sense that it can be provided by a relatively inexpensive thermo-electric cooler[34]. Toward this end, especially designed piezoelectric (PZ) InAs QD samples are grown by molecular beam epitaxy (MBE) using the Stranski-Krastanov (S-K) growth mode on (211)B GaAs substrates [35]. In this orientation, the InAs-based QDs carry a strong PZ field along the growth axis, bringing along a number of interesting properties. First, these dots exhibit enhanced X-XX splitting values, in the range of 4-13 meV [36–40], which is favorable for high temperature single photon emission at the QD exciton level, considering that the X and XX lines can remain spectrally-resolved at elevated temperatures. Second, the PZ QD excitons are characterized by reduced fine-structure splitting values [36,41], which is a prerequisite for the generation of high-fidelity entangled photons [42], Indeed, entangled photon emission has been predicted and observed in (111)B-oriented InAs-based nanostructures [43,44] and dots-in-wire [45–47]. Another interesting aspect of the (211)B PZ QDs is their increased sensitivity to external electric fields due to the quadratic nature of the quantum-confined Stark effect, giving rise to enhanced Stark tunings of their X lines, suggesting the feasibility of widely tunable single-photon sources[37].

## 2.5 The key for high temperature operation

Compared to prior work, here we resort to band-gap engineering of the surroundings of the (211)B QDs, in order to enhance their temperature stability and extend their single photon emission characteristics as near to room temperature as possible. In a previous study on the recombination dynamics of (211)B InAs/GaAs QDs, it was shown that the main activation mechanism for non-radiative recombination at high temperatures is associated with electron-hole pairs escaping from the QDs to the WL [39]. This was testified by the activation energy, determined by an Arrhenius plot of the photoluminescence (PL) intensity and found approximately equal to $\Delta E$. The fact that the activation energy corresponds to the escape of electron-hole pairs as a whole, rather than separate electrons or holes, strongly suggests that the thermionic escape

rates of electrons and holes from the QD to the WL are comparable. The above clearly indicate that in order to increase the operating temperature of (211)B InAs QDs as single photon emitters, we need to increase this activation energy. This can be achieved either by "pushing" the WL energy to higher energies, making use of appropriate AlGaAs barriers around the QD layer, or by shifting the QD energy to lower values, increasing for instance the QD size up to the point of introducing dislocations and adapting to the (211)B orientation growth methodologies such as strain-relaxing layer or metamorphic buffer, which have allowed emission of (100)InAs/GaAs QDs in telecom wavelengths[48,49]. In this study, we adopt the former approach, increasing the activation energy of the carriers in the QDs by encapsulating the QD layers in-between "digital" AlGaAs alloys, issued from binary GaAs/AlAs SSLs, with different combinations of AlAs and GaAs thicknesses. In such a strongly-confined piezoelectric QD system, we demonstrate single-dot emission up to 260K, with the X and XX lines remaining resolved at all temperatures, something never reported before for an InAs-based QD. As a consequence of the enhanced temperature stability in these dots, we report clear anti-bunching behavior at temperatures up to 230K from single PZ QDs embedded in a micro-cavity.

## 2.6 Sample fabrication

In this section details about the sample fabrication will be given. The growth conditions of the QDs, short period superlattice and the cavity will be discussed in detail. Finally, a brief description of the processing techniques that lead to single QD spectroscopy will be given.

### 2.6.1 SSL: digital alloy

The strongly-confined PZ InAs QD samples of this work are schematically presented in **Figure 2.1**. They are grown by MBE on a (2-11) B GaAs semi-insulating substrate and contain a single QD layer embedded in-between "digital" AlGaAs alloys, consisting of two "mirror" GaAs/AlAs SSLs, in order to increase the confinement of carriers inside the dots and the WL. The relative x and y thicknesses of the binary layers in the SSL period define the effective Al-composition of the digital AlGaAs and can be calculated by the following simple equation:

$$< Al >= \frac{y}{x+y}$$

Where $x$, $y$ is the thickness in Angstrom of the GaAs and AlAs SSL components respectively.

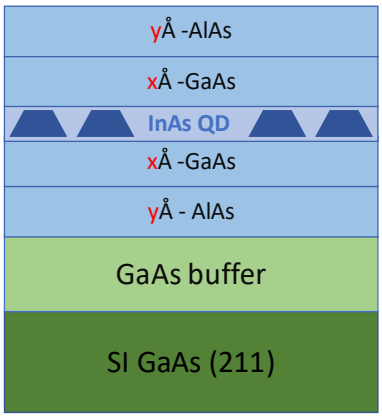


*Figure 2.1 Schematic of the strongly-confined piezoelectric InAs/GaAs QD samples were the QD layer is embedded in between GaAs/AlAs SSLs.*

The reason behind the use of GaAs/AlAs SSLs instead of real alloys is the moderate crystal quality of AlGaAs layers obtained in the (211)B orientation, due to growth-related difficulties related to the modified kinetics of Ga and Al adatoms on the stepped (211)B surface. Furthermore, the choice of digital alloys allows us to nucleate the InAs QDs always on a GaAs surface independently of the SSL's effective Al-composition, ensuring reproducible QD size and density characteristics.

### 2.6.2 QD inside a Cavity

The QD sample studied here with code name #1572 is grown by molecular beam epitaxy on a (211)B GaAs semi-insulating substrate. In order to enhance the single dot PL density by more than a decade the sample has the form of microcavity. The sample consists of a λ-cavity surrounded by bottom and top Distributed Bragg Reflectors (DBR's) as depicted in **Figure 2.2**. The bottom DBR is a 14-period GaAs/AlAs λ/4-stack providing a highly reflective stop-band centered around 950 nm with a reflectivity higher than 99 %, whereas the top DBR consists of a 4-period AlAs/GaAs λ/4-stack. The λ-cavity region consists of a 46 period 1.6 nm/1.2 nm AlAs/GaAs short-period superlattice (SSL), on which is grown the QD layer followed by a 46 period 1.2 nm/1.6 nm GaAs/AlAs "mirror" SSL.

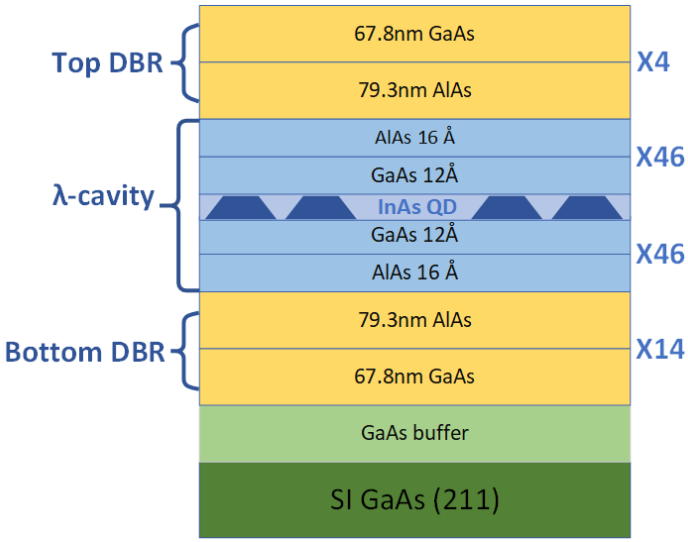


*Figure 2.2 Schematic representation of the sample #1572 grown with molecular beam epitaxy in the form of microcavity*

## 2.6.3 QD growth

The QD layer is at the anti-node of the standing electromagnetic field and is grown in the Stranski-Krastanov mode directly on the bottom SSL with deposition of 2 monolayers (MLs) of InAs at 480°C, using either of two different growth rates of 0.1 ML/s and 0.9 ML/s. Under these conditions, the QDs take the form of truncated pyramids with typical height between 2 and 3 nm, aspect ratio of about 10 and a density ranging between $7 \cdot 10^9$ and $2 \cdot 10^{10}$ $cm^{-2}$, depending on the growth rate.

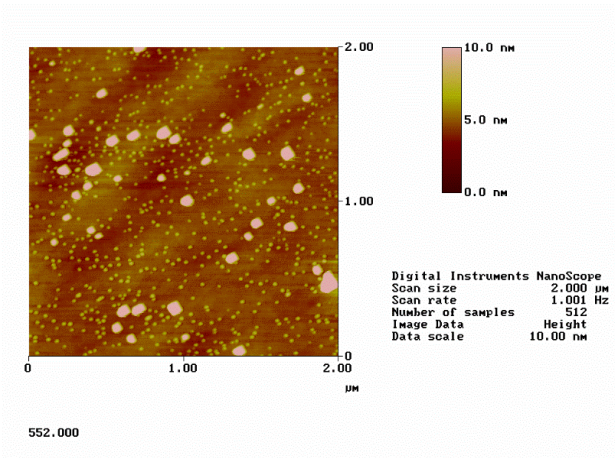


*Figure 2.3 The AFM results on the uncapped sibling of sample 1572, which show successful dot growth on an SSL using $t_g$ = 20 sec and $T_g$ = 480°C and growth rate of 0.1ML/s.*

The above numbers are deduced by atomic force microscopy measurements on reference samples as **Figure 2.3** shows, where identically grown QD layers were left

uncapped. Much lower QD densities of ~$7 \cdot 10^8$ $cm^{-2}$ can be achieved by carefully adjusting the amount of deposited InAs, just above the critical thickness for S-K growth in the (211)B orientation[35]. In most part of the SSLs, the growth of the AlAs and GaAs layers occurs at the optimal growth temperature of 635°C, with the exception of the first 10 SSL periods following the QD layer, where the growth temperature is ramped up from 480°C back to 635°C. In the studied samples, **x** varies between 8.6 and 23 Å, while **y** is kept constant at 16 Å, leading to a $< Al >$ - variation between 41% and 65%.

### 2.6.4 Processing techniques

To perform single dot experiments the grown samples are patterned into mesas with e-beam lithography followed by reacting ion etching. The equipment used for this job is the Field Emission SEM (Jeol 7000F), with an electron beam writer equipment attached to the system (Raith Elphy Quantum). For the dry etching of mesa pillars the reactive ion etching system (Vacutec 1500) was used.

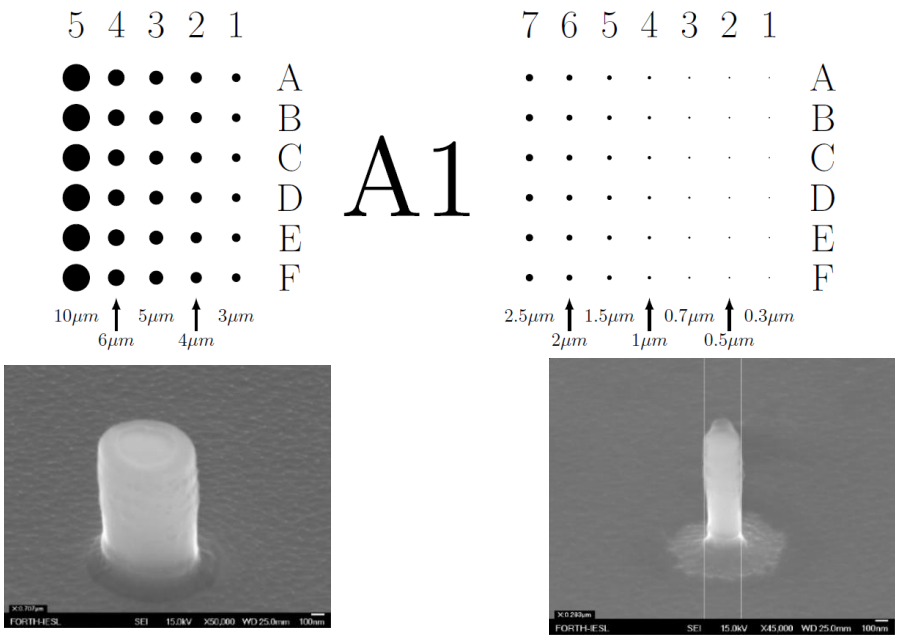


*Figure 2.4 (top) The layout of one period of mesas formed by electron-beam lithography on the surface of the sample, (bottom) SEM images of typical mesas used in the μ-PL experiments.*

The resulting mesas have ~1 μm-height with diameters varying from 0.3 μm to 10 μm. To prevent accidental excitation of a neighbor mesa the inter-spacing between them is 30μm. The layout and typical SEM images of mesas used for μ-PL are shown in **Figure 2.4** above.

## 2.7 Experimental Techniques

### 2.7.1 Optical characterization

The main optical characterization technique is PL and reflectivity measurements before the processing of the sample, followed by micro-photoluminescence (μPL) after the fabrication of mesas. Before discussing the results, it is useful to address the experimental setup used for the optical characterization of the samples. The optical setup in **Figure 2.5**. shows the PL setup where the reflectivity and PL take place. For the PL measurements a Helium-Cadmium (He-Cd) CW laser is used, and the laser beam is directed at an angle on the sample. Then, the signal from the sample is collected with a large diameter lens and is focused on the spectrometer entrance slits. For the reflectivity measurements a halogen lamp is used, and the light is guided through a Multi core Fiber (MCF) to illuminate the sample. Then the reflected light is collected and transferred on the spectrometer slits using a Multi-Mode Fiber (MMF). In both cases, the PL signal is analyzed using a 0.5 m spectrograph with a 150 g/mm grating and is recorded by a liquid nitrogen-cooled charge-coupled device camera (CCD).

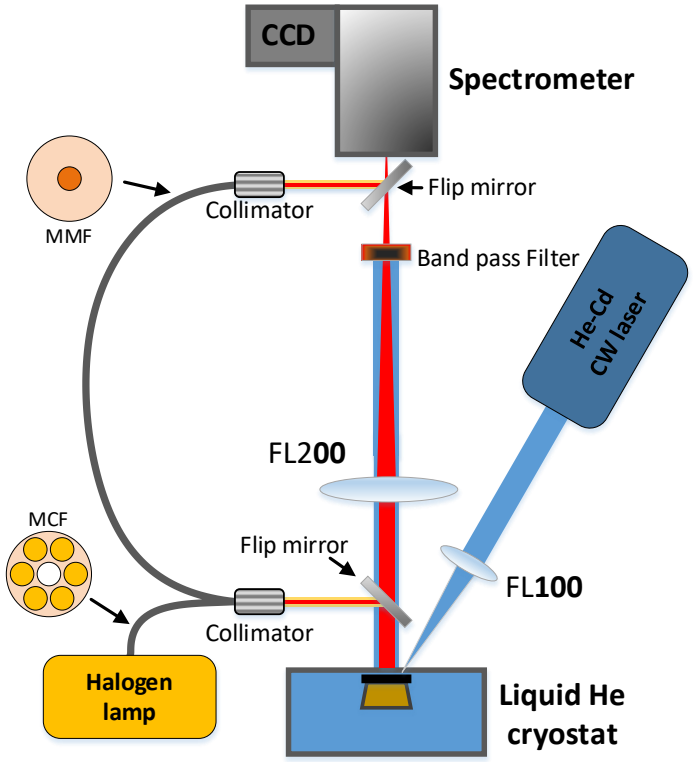


*Figure 2.5 Schematic illustration of the PL and reflectivity setup used for the characterization of the sample before processing.*

The SSL's described in the previous chapter, can be considered as an "AlGaAs" pseudo-alloy with an effective Al-composition of 57 %, adding a ~ 0.7 eV bandgap difference at the Γ-point, with respect to GaAs. Such high barriers can strongly modify the carrier confinement in the system. Specifically, the QD emission band blue-shifts by about 50 meV with respect to the emission of InAs QDs with GaAs barriers, extending now from 860 nm to 960 nm at low temperatures, as confirmed from PL spectra on identically grown strongly confined QDs *without* cavity. In the microcavity sample, this blue shift cannot be discerned, since the QD PL emission is vigorously enhanced at the ~930 nm cavity mode, as shown in **Figure 2.6** bellow.

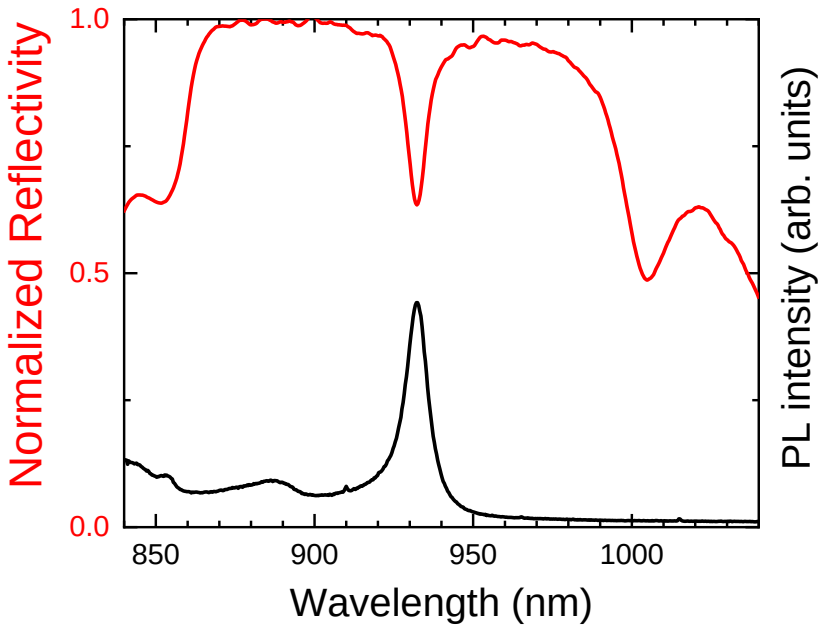


*Figure 2.6 Reflectivity and photoluminescence spectra from the sample #1572 at T=15K, showing a pronounced cavity mode at ~930nm.*

On the other hand, the confining effect of the SSL's to the WL transition is much stronger, based on the small WL thickness[35]. It can be shown, both theoretically and experimentally[50], that the WL emission energy for InAs QDs surrounded by the GaAs/AlAs SSL's used in this work, blue-shifts by as many as 200 meV, compared to the WL position in InAs QDs with GaAs barriers. The varied way that the SSL's affect the QD and WL transition energies is central to interpreting our results, as will be discussed later.

After processing, the sample is characterized with μ-PL technique. This setup which is schematically illustrated in **Figure 2.7** shares the same principles with that of PL setup but with some major differences. Here the laser beam from the source is focused on the sample through a microscope objective, and a regular camera is used to obtain an optical image of the illuminated area for precise excitation of the mesas. The shape and size of the beam are adjusted by a spatial filter which provides a clean spatial profile of a Gaussian beam to the μ-PL setup. The beam is then focused via the prementioned objective lens with 40x magnification and numerical aperture of 0.60, giving a lateral resolution of about 1 μm. The μ-PL signal is then collected by the same objective, analyzed by a 0.75 m spectrograph with a 1200 g/mm grating blazed at 750 nm, and recorded by a high quantum efficiency liquid nitrogen-cooled back-thinned CCD camera.

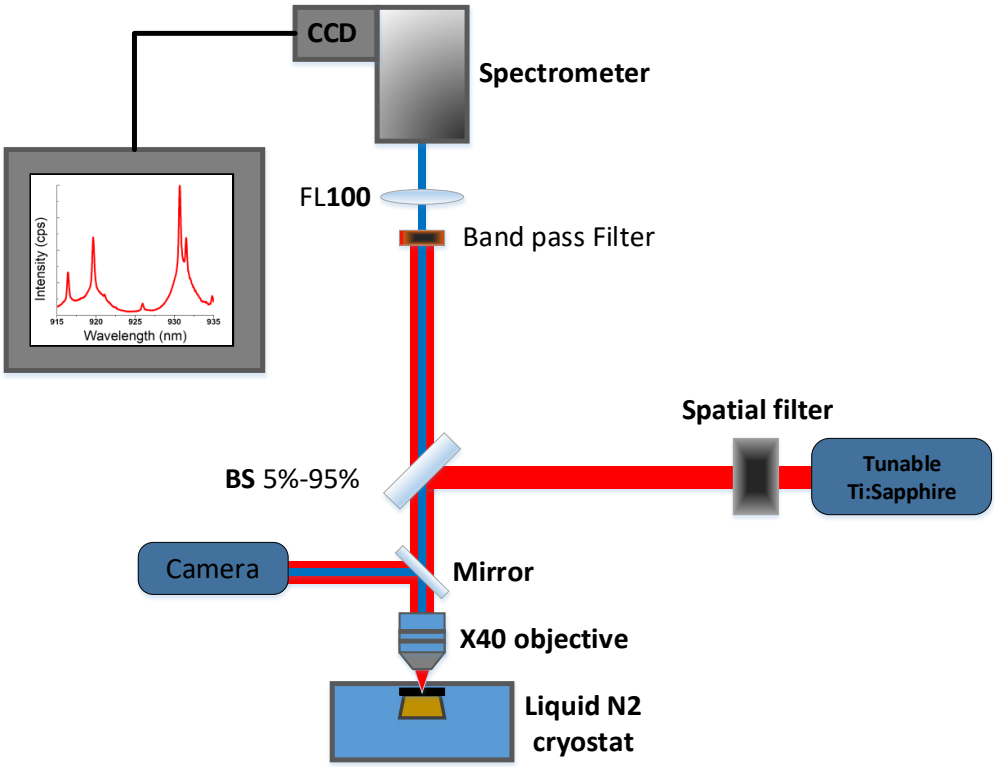


*Figure 2.7 Schematic of micro-PL setup used to perform single dot spectroscopy*

## 2.7.2 Autocorrelation measurements

For the implementation of photon correlation experiments, a tunable Ti:Sapphire laser is used for excitation, either in the femtosecond pulsed mode or in the continuous-wave (CW) mode. In pulsed mode, the repetition rate of the laser is 80 MHz.

To record the photon statistics of the single QDs, the same μPL setup described before is used to collect the photoluminescence of the samples and the signal is analyzed and directed to the side exit of the same spectrograph.

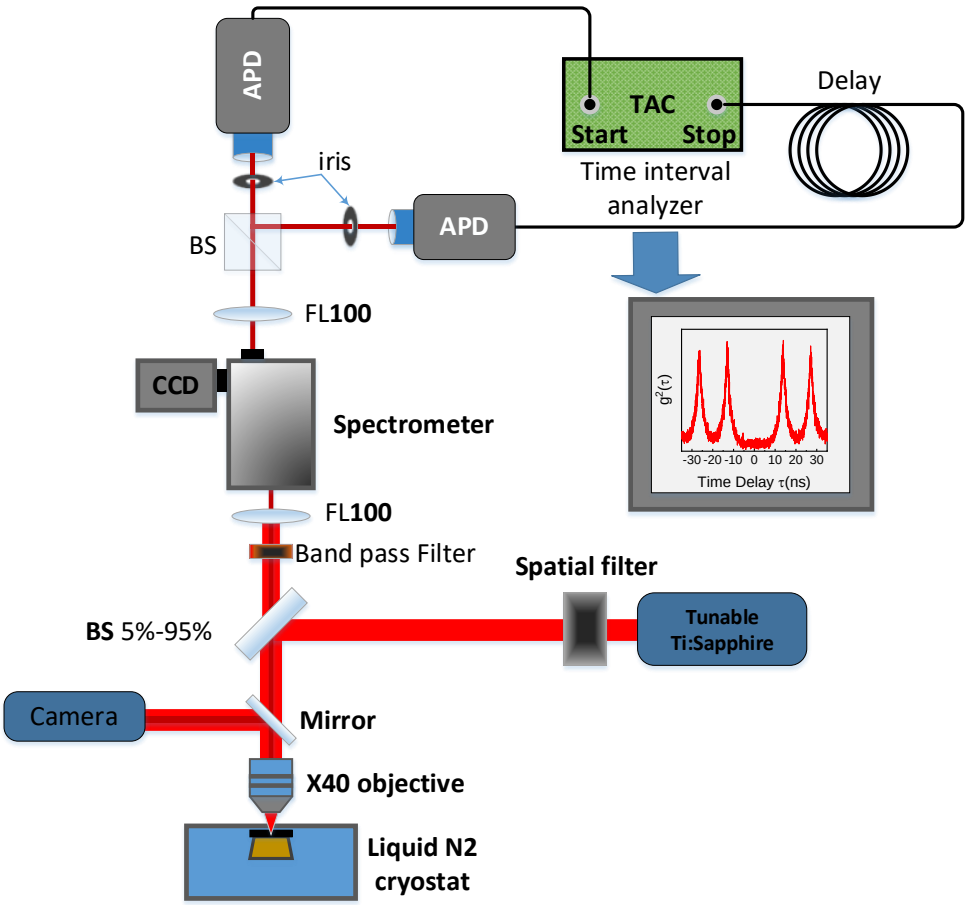


*Figure 2.8 Schematic illustration of the HBT setup used for autocorrelation experiments.*

The light from the single photon source is then spectrally filtered by passing through the slit opening at the back of the spectrograph. The spectral window of observation is adjusted by the slit opening and can be as narrow as 50 μeV. The spectrally-filtered QD signal is then split by a 50/50 non-polarizing beam splitter in the two arms of a Hanbury Brown and Twiss (HBT) [51] setup **Figure 2.8** and is collected by two fast Silicon fiber-coupled Single Photon Avalanche Photodiodes (SPADs) with 340 ps time resolution. Two mechanical irises are placed in the path before the SPADs to avoid cross-talking phenomena [52]. The photon incidences in the two detectors are time-correlated using a single-photon counting acquisition card by Becker & Hickl (SPC-130), with a channel width down to 820 fs.

## 2.8 Band gap tunning

### 2.8.1 Increasing the QD and WL energy difference

The presence of the SSL barriers around the dots enhances $\Delta E$, by affecting the WL ground state much more efficiently than the QD exciton level, due to the smaller WL thickness. This can be observed experimentally in the PL spectra of **Figure 2.9a**, where by increasing $< Al >$ from 0% to 57%, the center of weight of the QD emission bands indicated by red arrows is blue-shifted by merely ~ 60 meV, whereas the corresponding blueshift of the WL transition shown in blue arrows is nearly 200 meV. These blueshifts can be readily accounted for, considering that an SSL with $< Al >=$ 57 % exhibits a ~ 0.7 eV bandgap difference at the Γ-point with respect to GaAs. The indicated position of the WL transition in the reference sample at 1.415eV is based on previous studies on similar (211)B InAs/GaAs QDs [35,39]. For the sample with $< Al >$ =41%, the WL peak can be distinguished as a shoulder next to the sharp GaAs substrate peaks. Notably, the intensity of the WL emission increases drastically with rising $< Al >$. This increase is not due to a variation in the QD density, which does not change significantly in these samples, but is rather attributed to the enhanced carrier localization due to increasing disorder in the SSL-embedded WL, a hypothesis supported by the increased WL linewidths in the higher $< Al >$ composition samples.

Theoretical estimates of the QD and WL transitions as a function of $< Al >$ reproduce reasonably well the experimental results, as depicted in **Figure 2.9b**. The estimates, shown in solid lines, are based on the solution of a one-dimensional (1D) Schrödinger equation in the envelope function approximation, using the nextnano$^3$ nanostructure simulator [53]. Strain and PZ effects in the (211)B orientation are explicitly taken into account and standard III-V material parameters are used [54]. The 1D simplification is justified in our case by the large aspect ratio of the QDs, implying that the quantum confinement along the growth direction is much stronger compared to the lateral direction.

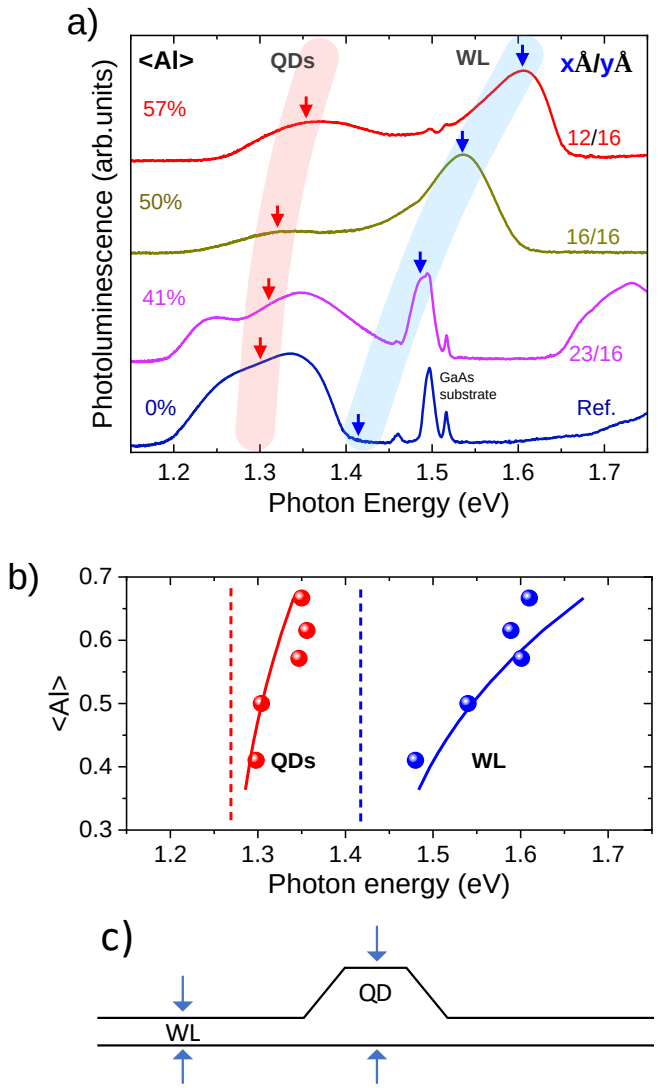


*Figure 2.9 a) Macro-PL spectra at T=20 K of QDs embedded in xÅ GaAs/yÅ AlAs SSLs with different relative thicknesses of GaAs and AlAs layers, in comparison with a reference sample where the QDs are embedded in GaAs. The dot-dashed lines are guides to the eye for the evolution of the QD and WL transitions with increasing Al-concentration. b) Schematic representation of a QD and corresponding WL. c) Calculated QD and WL transition energies (solid lines) as a function of Al-concentration and comparison with experimental data points. The dashed lines represent the corresponding transition energies of the reference sample.*

To take into account the intermixing effects of Gallium and Indium atoms, revealed by high-resolution transmission electron microscopy (HR-TEM) experiments on very similar (211)B InAs/GaAs QDs, [37,55] the WL and QD are considered as $In_xGa_{1-x}As$ quantum wells of different thicknesses. In fact, the alloy composition, and the WL and QD thicknesses are the main adjustable parameters of the simulation. Both WL and QD are sandwiched between two "mirror" GaAs/AlAs SSLs, in which the AlAs thickness is 16Å and the GaAs thickness varies between 8Å and 28Å, translating to an $< Al >$-range between 37% and 67%. The solid lines in **Figure 2.9b** represent the

simulated QD and WL transitions, corresponding to a particular selection of the adjustable parameters, namely, an alloy of $In_{0.5}Ga_{0.5}As$, a 0.8nm-thick WL and a 3nm-thick QD. With this set of parameters, the simulation reproduces rather well the data points of both transitions of $< Al >$, as well as the WL position in the reference sample (blue dashed line). On the other hand, the simulation falls a bit short on the QD position of the reference sample, which is simulated at 1.27 eV (red dashed line), instead of the 1.3 eV determined in **Figure 2.9a**. This discrepancy can be easily accounted for by a small change in the QD thickness of the reference sample. At any rate, the intention here was not to provide a precise fitting of the experimental results, but rather to reproduce their general tendency, which is that with increasing $< Al >$, the WL transition blue-shifts much "faster" than the QD transition, as expected based on the smaller thickness of the WL (**Figure 2.9c**) and in good agreement with the experimental results.

## 2.8.2 Increasing the Activation energy

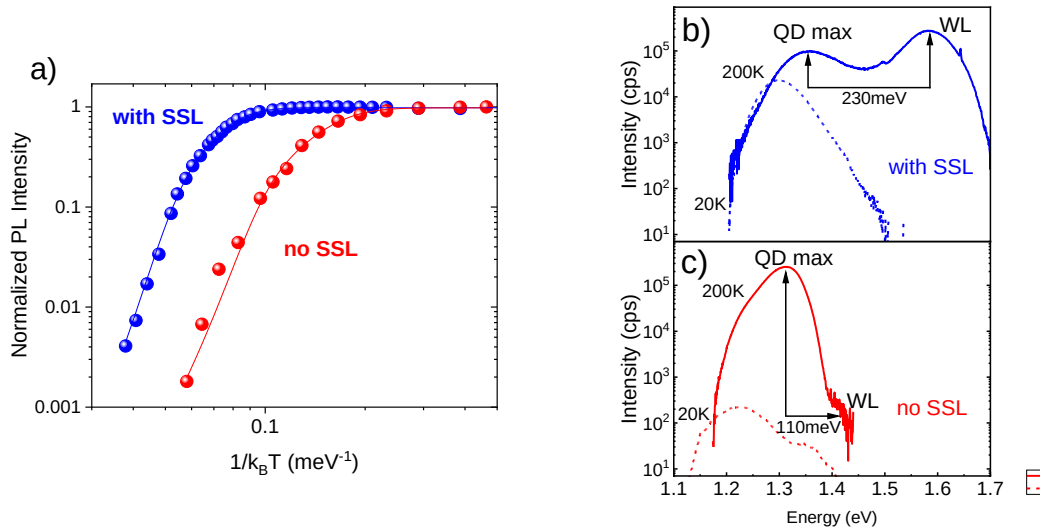


*Figure 2.10 a) Arrhenius plots of normalized PL intensities for two different QD samples, with and without SSL. The solid lines are best fits of the Arrhenius equation described in the text to the corresponding data points. b),c) Macro-PL spectra of the QD samples, with and without SSL, at two different temperatures, highlighting the beneficial role of the SSL in maintaining the PL intensity at high temperatures. The energy difference between the QD and WL peaks is also denoted in each case.*

In order to prove the beneficial role of the SSL at elevated temperatures, PL measurements were performed in two different samples. One with SSL of $< Al >=$ 65% and a reference sample without SSL. In **Figure 2.10a,** the Arrhenius plot of the

two samples is compared. Each data point in the Arrhenius plot, corresponds to the QD PL intensity at different temperature, integrated over a spectral window of $\pm 4$ nm around a wavelength of reference at a given temperature, $\lambda_{ref}(T)$. To consider the variation of the exciton wavelength with temperature, $\lambda_{ref}(20K)$ is set at the peak of the QD emission at T=20K, while for higher temperatures, $\lambda_{ref}(T)$ varies according to Varshni's law [56].

As shown in **Figure 2.11b**, the Varshni equation describing the actual temperature evolution of excitons in (211)B InAs/GaAs QDs is identical with that of bulk GaAs. One reason for this behavior is that the QDs are practically inclusions of Gallium-rich InGaAs alloys[55]. The second possible reason is that in these QDs, a significant part of the electron wavefunctions extend inside the GaAs barriers to a percentage ranging between 30% and 60% depending on the details of the surrounding barriers, with the highest percentage corresponding to plain GaAs barriers without SSLs. By inspection of **Figure 2.10a**, it is clear that the PL intensity of the reference sample drops by one decade already at ~120K, while for the sample with SSL, this occurs at the much higher temperature of ~230K, underscoring the advantage of strong-confinement for higher operating temperatures. The solid lines passing through the data points are best fits to the following equation:

$$I = I_0 \cdot \frac{1}{1 + a \cdot e^{-\frac{E_a}{kT}} + b \cdot e^{-\frac{E_b}{kT}}} \qquad 2\text{-}1$$

The two exponentials correspond to different activation processes, effective in the low and high temperature regimes. At low temperatures, a small decrease in PL intensity observed in both samples, can be accounted for by a small activation energy $E_b \approx (35 \pm 5)$ meV along with a weak probability coefficient $b$, of the order of 100. The origin of this weak activation process is most likely the exciton thermalization to the p-shell of the QDs, whose energy separation from the X line is of the order of 30 meV, as suggested by PL excitation spectroscopy. A much more efficient activation mechanism is necessary to describe the drastic drops in intensity at higher temperatures for both samples. The respective fittings to the Arrhenius equation give a much larger probability coefficient $a$, of the order of $10^{12}$, and an activation energy $E_a$ of ~(125 ± 15) meV for the sample without SSL and of ~(265 ± 30) meV for the sample with SSL. As discussed earlier [39], these activation energies correspond very well to the respective

$\Delta E$-values of ~(110 ± 10) meV and ~(240 ± 20) meV, indicated in the PL spectra of **Figure 2.10b** and **Figure 2.10c**.

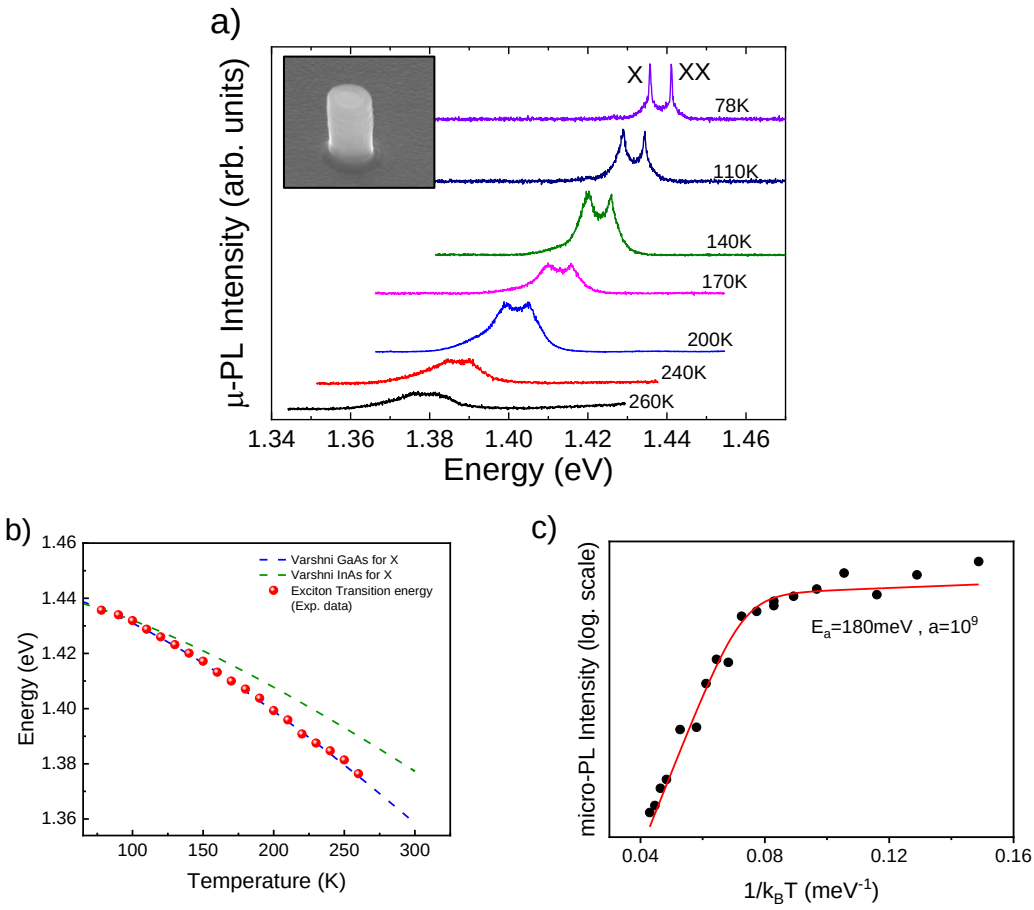


*Figure 2.11 (a) Temperature-dependent μ-PL spectra of a single (211)B InAs/GaAs QD which is strongly-confined in between GaAs/AlAs SSLs with <Al>=57%. The single dot spectra are interspaced vertically for clarity and consist of an exciton (X) and a biexciton (XX) line that remain easily resolved up to 260K in spite of the line broadening. (b) Energy variation of the single (211)B InAs/GaAs QD exciton emission of Figure 3 of the manuscript as a function of temperature, following closely the Varshni equation for GaAsS1. (c) Arrhenius plot for the emission of the same strongly-confined single QD, showing an enhanced activation energy due to the presence of SSLs*

The PL enhancement at high temperatures induced by the SSLs, allows us to observe single dot emission almost at room temperature (270K), even in samples without any microcavity-induced amplification. In **Figure 2.11a**, we show temperature-dependent μ-PL spectra from a single (211)B InAs/GaAs QD, sandwiched in-between 12 Å/16 Å GaAs/AlAs SSLs, with <Al>=57%. The sample is processed by e-beam lithography into circular mesas with diameters as low as 350 nm, as the one shown in the inset of **Figure 2.11a**. At T=78 K, the μ-PL spectrum consists of two sharp lines, assigned to X and XX emission from the same dot, based on the linear and quadratic power-dependence of their intensities, respectively. In this particular dot, the XX line

is blue-shifted by 5.4 meV with respect to X, denoting an anti-bound bi-exciton state, something typical in PZ QDs [23,24,36–40]. By analyzing the temperature-dependent μ-PL spectra of **Figure 2.11**, a number of useful conclusions can be reached. First of all, the QD excitons red-shift with temperature following the Varshni relation of bulk GaAs rather than InAs, most likely due to intermixing effects and wavefunction spill-out into the barriers. Second, the fact that the μ-PL signal of single QDs persists well with temperature is a consequence of enhanced $\Delta E$-values. Specifically, the low-temperature X-position of the dot in **Figure 2.11** is ~1.44 eV, while the WL transition energy of this sample is at ~1.61 eV (top PL spectrum in **Figure 2.9a**), suggesting a $\Delta E \approx (170 \pm 15)$ meV for this dot. This $\Delta E$-value corresponds well to the activation energy of $E_a \approx (180 \pm 20)$ meV, determined from the Arrhenius plot of **Figure 2.11c**. Third, the thermal broadening of excitons in (211)B InAs/GaAs QDs at high temperatures is very similar to that observed in (100) counterparts [57,58], suggesting that the high internal fields in the PZ QDs do not generate any additional broadening compared to non-PZ QDs. This is illustrated in **Figure 2.12** of the supplementary information, where the linewidth curves of the (211)B and (100) QD systems merge at $T \geq 250$K, to full-width half-maximum (FWHM) values of 6-7 meV. In the context of this work, the most interesting feature of **Figure 2.11** is clearly that the X and XX emission lines remain resolved up to 260K. This is a prerequisite for single-photon emission with high single-photon purity at such elevated temperatures and comes as a consequence of the relatively high XX-X splittings in our system and the enhanced temperature stability of the SSL-embedded QDs.

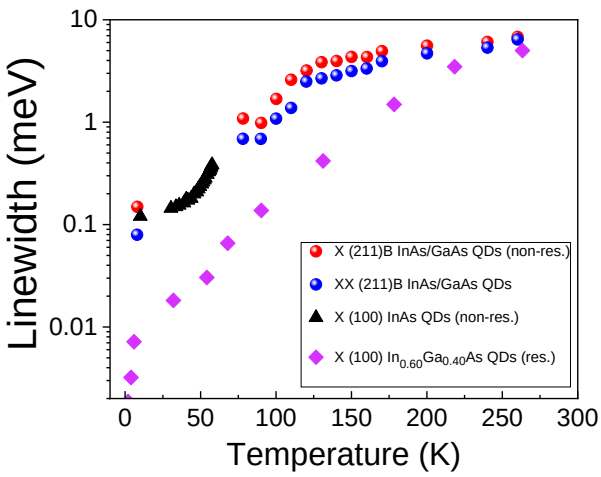


*Figure 2.12 Temperature-dependent FWHM linewidths of the X and XX lines (circles) of the single (211)B InAs/GaAs QD of Figure 3 of the manuscript, in comparison with reported results on (100) QDs under resonant[S2] (rhombs) and non-resonant[S3] (triangles) excitation conditions*

### 2.8.3 Single photon emission up to 230K

A single QD can emit anti-bunched photons because it is essentially a two-level system. When a QD emits at the exciton line a single photon at τ=0, it is impossible to emit a second one because the system is already in the ground state. The next photon can be emitted only when the system is re-excited and the detection-waiting time between two consecutive photons depends on the repetition rate of the excitation source. The statistics of the emitted photons for a QD are sub-Poissonian, which means that the QD operates below the threshold of the Poisson's distribution which is described as follows:

$$P_a(n) = \frac{N^n}{n!} \cdot e^{-N} \qquad 2\text{-}2$$

Where $P_a(n)$ is the probability to find n photons in a coherent state with mean photon number $N = a^2$. Any state that has a narrower photon distribution than Poisson's, like the QD exciton is called sub-Poissonian. To prove the quantum nature of the system the second order correlation function $g^{(2)}(\tau)$ is measured as a function of the delay time τ and can be written as follows:

$$g^2(\tau) = \frac{\langle I(t) I(t+\tau) \rangle}{\langle I(t)^2 \rangle} \qquad 2\text{-}3$$

Where $\langle \cdot \rangle$ denotes the time average and $g^2(\tau)$ is the probability to measure a second photon at a time τ≠0, when a first photon has already been detected at τ=0. For a pure single photon emitter, the $g^2(\tau = 0)$=0. When the number of emitters is increased the $g^2(t)$ is no longer zero, and for this reason the criterion to characterize a single photon emitter is $g^2(t) \leq 0.5$.

The temperature-dependent anti-bunching experiments are performed on the microcavity sample #1572 to take advantage of the about one order of magnitude enhancement in the μ-PL intensity. In **Figure 2.13a**, we present temperature-dependent μ-PL spectra from the dot, which showed single photon emission at 230K. The excitation conditions were identical to those used in the anti-bunching experiments. The μ-PL spectrum at 78K contains four main peaks, marked according to their detailed assignment which will be discussed in the next chapter.

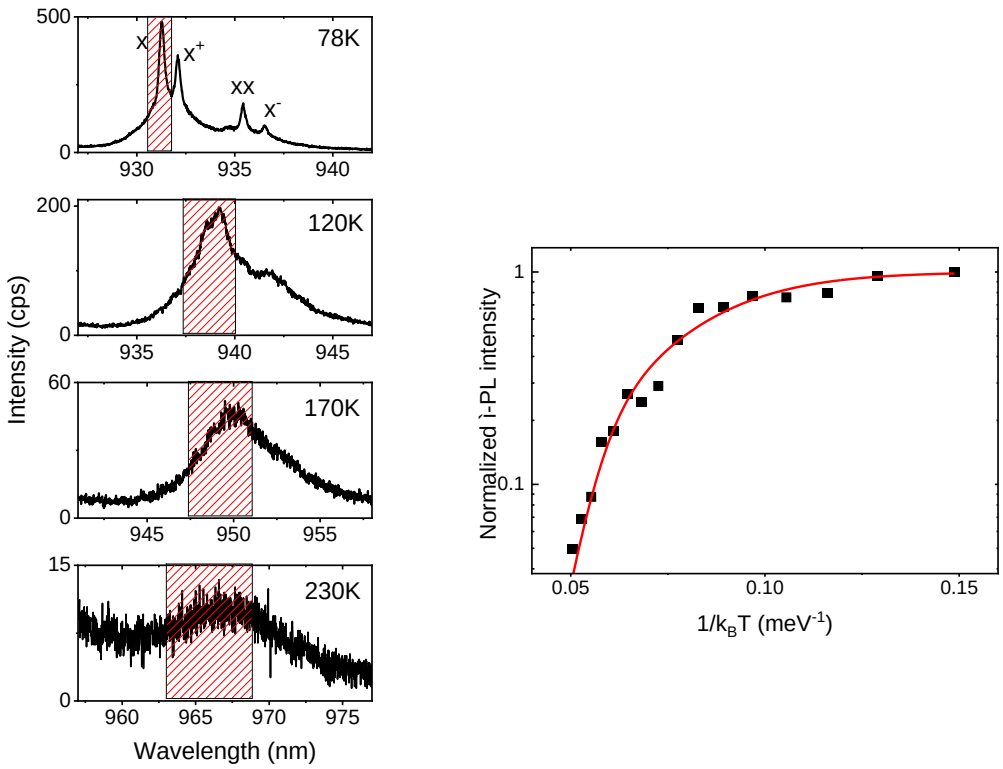


*Figure 2.13 (a)Temperature-dependent μ-PL spectra under pulsed excitation from the single (211)B InAs/GaAs QD in a microcavity, used in the antibunching experiments. The shaded areas indicate the spectral window used in the antibunching experiments at each temperature (b) Arrhenius plot of the spectrally-integrated μ-PL emission for the (211)B InAs/GaAs QD of Figure 4 of the manuscript, used in the antibunching experiments. The fitting curve corresponds to an activation energy of $E_a$ = 240 meV*

With increasing temperature, the charged exciton lines ($X^+$ and $X^-$) rapidly lose intensity. The power of excitation is constant for all temperatures and well below the saturation level, to minimize bi-excitonic emission and ensure high single-photon purity at the exciton level. The shaded areas indicate in each case the spectral window used in the anti-bunching experiment of the same temperature. It should be noted that even if some $X^+$ photons coexist in the spectral window of the X emission up to some temperature, the overall single-photon characteristics should not be affected, considering that the X and $X^+$ lines are found strongly anti-bunched, based on cross-correlation spectroscopy that will be discussed also in next chapter.[30] In the microcavity sample, we expect enhanced temperature stability of the dots, since the QD layer is embedded in between GaAs/AlAs SSLs with <Al>=57%. This is confirmed by the enhanced activation energy of $E_a$ = (240 ± 20) meV, determined by the corresponding Arrhenius plot, shown in **Figure 2.13b**.

In **Figure 2.14**, we present the second order correlation function of the X-line under pulsed excitation. To obtain the $g^2(\tau = 0)$, the τ=0 peak in each of histogram is

normalized with respect to the four adjacent peaks. The fitting function used for each peak was the following:

$$y = Ae^{-\left|\frac{\tau-\tau_i}{\tau_d}\right|} \qquad 2\text{-}4$$

This exponential function is fitted for every peak of the antibunching histogram, with $\tau_i$ corresponding to the peak position in the delay line and $\tau_d$ the decay time of the measured excitonic state.

The value of $g^{(2)}(0) \leq 0.5$ at zero delay time ($\tau = 0$) testifies the emission of non-classical light in the form of single photon emitter. The average excitation power was kept below the exciton saturation level at about ~0.3μW/cm2 which was the same for all the temperatures. Above that excitation value, the background underlying the QD emission increases so we chose not to completely fill the QD with carriers in order have sufficient count rates and low signal to noise ratios.

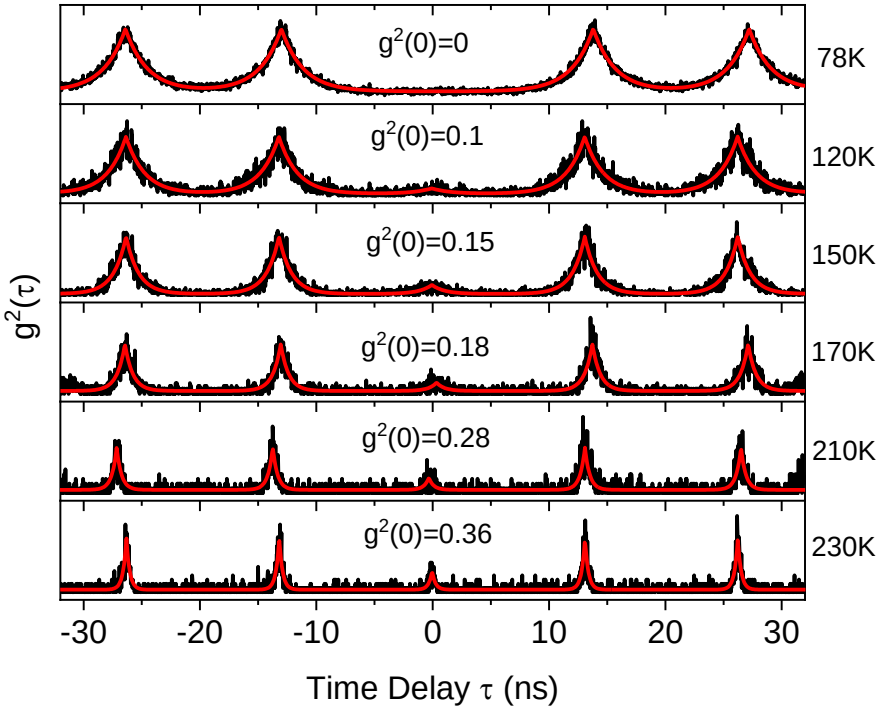


*Figure 2.14 Coincidence counts histograms obtained from 77K to 230K using an HBT auto-correlation setup under pulsed excitation, representing the normalized second order intensity correlation function g2(τ) from the photons of the excitonic transition*

The average photon counting rate on each APD during the accumulation of the coincidence histograms at 77K, 120K, 150K, 170K, 210K and 230K was 40000, 25000,

16000, 6000, 2000 and 1000 cps, respectively, while the respective integration times were 30, 40, 60, 120, 340 and 340 minutes. The dark count rate on each APD was ~120 cps. The $g^{(2)}(\tau)$ function represents the probability of detecting a coincidence photon at time $\tau$, following the detection of a "start" photon at time zero. As expected for a single-photon emitter, the normalized $g^{(2)}(\tau)$ curves exhibit a series of intense coincidence peaks at repeat laser pulses with $\tau \neq 0$ and a "weak" or null coincidence peak around $\tau=0$. The $g^{(2)}(0)$ values marked next to each curve, are obtained by fitting the data with double-exponentials without applying any background correction, and correspond to the area under the $\tau=0$ peak divided by that of the adjacent peaks. For all temperatures, the $g^{(2)}(0)$ values remain well below 0.5 satisfying the criterion for single-photon emission. At 78K, in particular, $g^{(2)}(0)$ cannot be determined by fitting, due to the lack of significant coincidence counts around $\tau=0$. Instead, we give an upper bound estimate of $g^{(2)}(0) \leq 0.02$. To the best of our knowledge, such small $g^{(2)}(0)$ value at liquid nitrogen temperature has never been reported before in any QD system. For comparison, we cite several values of $g^{(2)}(0)$ at 78 K in other systems: in optically-pumped InGaAs/GaAs QDs $g^{(2)}(0)$ is between 0.177 and 0.26, [18] in electrically-pumped InAs/GaAs QDs 0.35[19], in GaAs QDs grown by droplet epitaxy 0.27[59] and finally in GaN/AlN QDs between 0.26 and 0.35[23]. Observing a $g^{(2)}(0) \leq 0.02$ at 78 K in our case, demonstrates the high single-photon purity of the (211)B PZ QD system, as a consequence of the large X-XX splittings and the relatively high signal to background ratio in this temperature. In our system, the background photons arise mainly from emission in the WL, and to a lesser degree in the SSL barriers of the structure. At higher temperatures, however, the $g^{(2)}(0)$ increases progressively, reaching the value of 0.36 at 230K. This is due to the relative increase of the background level with respect to the QD signal, as can be confirmed in the high-T spectra of **Figure 2.13a**. Another characteristic of the $g^{(2)}(\tau)$ curves is that the coincidence peaks become narrower with increasing temperature. This can be explained by the fact that the temporal profile of the coincidence peaks follows the X decay time at a given temperature. It is worth noting that the X decay times determined by temporal fitting of the anti-bunching curves are very consistent with those directly measured by us in TRPL experiments on the very same dot, as presented in **Figure 2.15** bellow.

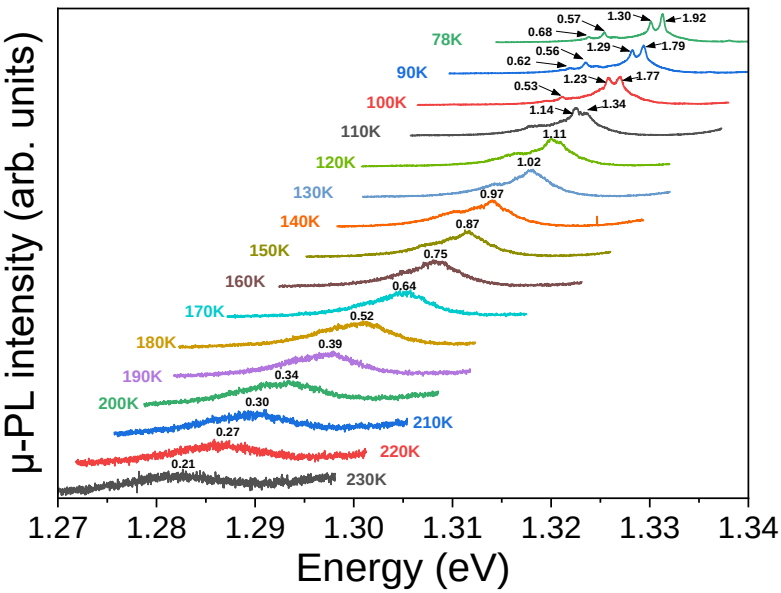


*Figure 2.15 Complete set of temperature-dependent μ-PL spectra for the microcavity-embedded InAs/GaAs QD, discussed in Figure 4 and 5 of the manuscript. Next to each spectrum, are indicated in nanoseconds the time-decays of the respective emission lines deduced from TRPL experiments*

To illustrate this point, we show in **Figure 2.16** the information the TRPL and anti-bunching curves of the same dot at 78 K, whose fittings lead to practically same X lifetime.

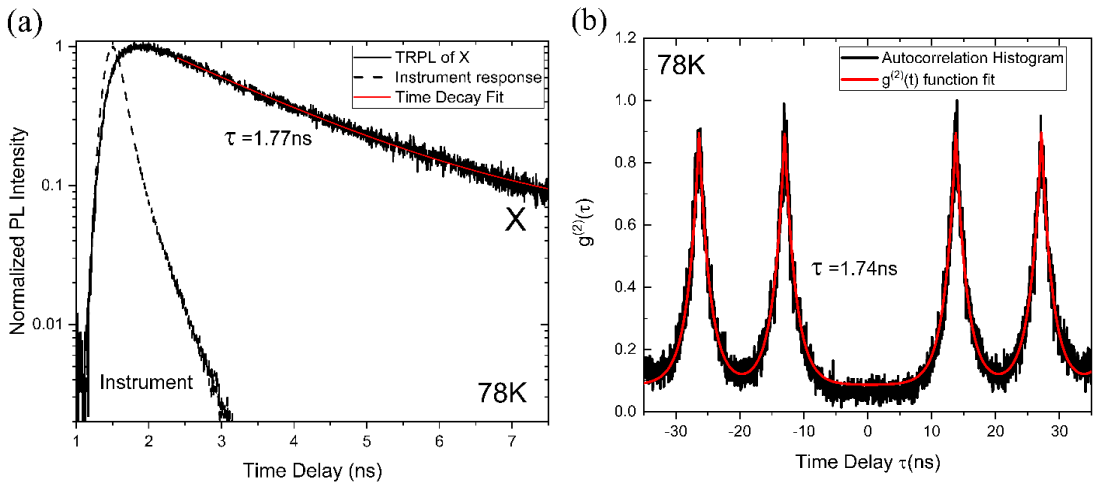


*Figure 2.16: (a) TRPL decay curve at 78 K from the X line of the microcavity-embedded InAs/GaAs QD, discussed in Figure 4 and 5 of the manuscript. The solid line running through the data is a mono-exponential fitting curve giving a lifetime of τ=1.77 ns. The instrument response to a femtosecond laser pulse is also shown in dashed line. (b) Anti-bunching curve obtained from the X line of the same QD at 78K, and related fitting with double-exponentials, leading to a lifetime of τ=1.74 ns, in very good agreement with TRPL.*

## 2.9 Conclusions

In this chapter we have demonstrated, using a strongly-confined (211)B piezoelectric InAs quantum dot, single photon emission up to 230K with excellent single-photon purity at liquid nitrogen temperature. The used short period GaAs/AlAs superlattices improved drastically the temperature stability of the QD emission by preventing the carriers from escape into the wetting layer. The other key ingredient of this study is the piezoelectric orientation, which enabled the large X-XX splittings in the system and thus the observation up to 260K of spectrally resolved X and XX peaks originating from a single quantum dot. It is important to note that the above quantum dot system is capable, with minor modifications, of single-photon emission at higher temperatures than 230 K. The main parameters controlling the operating temperature are the average Al-composition in the barriers, the X-XX splitting in the dot and the position of the cavity mode. If for example, the cavity mode in the sample of Figure 2.13a and Figure 2.14 was shifted to longer wavelengths by merely 50 nm, room temperature operation would already be achievable. As a final remark, it should be commented the main advantage in the context of this work of piezoelectric quantum dot samples over the conventional ones, which is that they can provide big numbers of "useful" quantum dots with sufficiently large |XX-X| splittings. In fact, in the two samples discussed in **Figure 2.11**, **Figure 2.13** and **Figure 2.14**, more than 50 % of the studied quantum dots showed |XX-X| larger than 5 meV.

# References


1. Michler, P. *et al.* A quantum dot single-photon turnstile device. *Science (1979)* **290**, 2282–2285 (2000).
2. Santori, C., Pelton, M., Solomon, G., Dale, Y. & Yamamoto, Y. Triggered Single Photons from a Quantum Dot. *Phys Rev Lett* **86**, 1502 (2001).
3. Zwiller, V. *et al.* Single quantum dots emit single photons at a time: Antibunching experiments. *Appl Phys Lett* **78**, 2476–2478 (2001).
4. Oliver Benson, Charles Santori, Matthew Pelton & Yoshihisa Yamamoto. Regulated and Entangled Photons from a Single Quantum Dot. *Phys Rev Lett* **84**, 2513 (2000).
5. Claudon, J. *et al.* A highly efficient single-photon source based on a quantum dot in a photonic nanowire. *Nature Photonics 2010 4:3* **4**, 174–177 (2010).
6. Somaschi, N. *et al.* Near-optimal single-photon sources in the solid state. *Nature Photonics 2016 10:5* **10**, 340–345 (2016).
7. Sapienza, L., Davanço, M., Badolato, A. & Srinivasan, K. Nanoscale optical positioning of single quantum dots for bright and pure single-photon emission. *Nature Communications 2015 6:1* **6**, 1–8 (2015).
8. Liu, J. *et al.* A solid-state source of strongly entangled photon pairs with high brightness and indistinguishability. *Nature Nanotechnology 2019 14:6* **14**, 586–593 (2019).
9. Laucht, A. *et al.* Awaveguide-coupled on-chip single-photon source. *Phys Rev X* **2**, 1–7 (2012).
10. Gschrey, M. *et al.* Highly indistinguishable photons from deterministic quantum-dot microlenses utilizing three-dimensional in situ electron-beam lithography. *Nature Communications 2015 6:1* **6**, 1–8 (2015).
11. Chen, Y., Zopf, M., Keil, R., Ding, F. & Schmidt, O. G. Highly-efficient extraction of entangled photons from quantum dots using a broadband optical antenna. *Nature Communications 2018 9:1* **9**, 1–7 (2018).
12. Santori, C., Fattal, D., Vučković, J., Solomon, G. S. & Yamamoto, Y. Indistinguishable photons from a single-photon device. *Nature 2002 419:6907* **419**, 594–597 (2002).
13. Daveau, R. S. *et al.* Efficient fiber-coupled single-photon source based on quantum dots in a photonic-crystal waveguide. *Optica, Vol. 4, Issue 2, pp. 178-184* **4**, 178–184 (2017).
14. Schlehahn, A. *et al.* A stand-alone fiber-coupled single-photon source. *Scientific Reports 2018 8:1* **8**, 1–7 (2018).

15. Yuan, Z. *et al.* Electrically driven single-photon source. *Science (1979)* **295**, 102–105 (2002).
16. Salter, C. L. *et al.* An entangled-light-emitting diode. *Nature 2010 465:7298* **465**, 594–597 (2010).
17. Schlehahn, A. *et al.* An electrically driven cavity-enhanced source of indistinguishable photons with 61% overall efficiency. *APL Photonics* **1**, 11301 (2016).
18. Mirin, R. P. Photon antibunching at high temperature from a single InGaAs/GaAs quantum dot. *Appl Phys Lett* **84**, 1260–1262 (2004).
19. Dou, X. M. *et al.* Single-photon-emitting diode at liquid nitrogen temperature. *Appl Phys Lett* **93**, 101107 (2008).
20. Finley, J. J. *et al.* Observation of multicharged excitons and biexcitons in a single InGaAs quantum dot. *Phys Rev B* **63**, 161305 (2001).
21. Thompson, R. M. *et al.* Single-photon emission from exciton complexes in individual quantum dots. *Phys Rev B* **64**, 201302 (2001).
22. Rodt, S. *et al.* Repulsive exciton-exciton interaction in quantum dots. *Phys Rev B* **68**, 035331 (2003).
23. Holmes, M. J., Choi, K., Kako, S., Arita, M. & Arakawa, Y. Room-temperature triggered single photon emission from a III-nitride site-controlled nanowire quantum dot. *Nano Lett* **14**, 982–986 (2014).
24. Tamariz, S. *et al.* Toward Bright and Pure Single Photon Emitters at 300 K Based on GaN Quantum Dots on Silicon. *ACS Photonics* **7**, 1515–1522 (2020).
25. Bounouar, S. *et al.* Ultrafast room temperature single-photon source from nanowire-quantum dots. *Nano Lett* **12**, 2977–2981 (2012).
26. Fedorych, O. *et al.* Room temperature single photon emission from an epitaxially grown quantum dot. *Appl Phys Lett* **100**, 61114 (2012).
27. Lounis, B. & Moerner, W. E. Single photons on demand from a single molecule at room temperature. *Nature 2000 407:6803* **407**, 491–493 (2000).
28. Gruber, A. *et al.* Scanning confocal optical microscopy and magnetic resonance on single defect centers. *Science (1979)* **276**, 2012–2014 (1997).
29. Beveratos, A. *et al.* Room temperature stable single-photon source. *The European Physical Journal D - Atomic, Molecular, Optical and Plasma Physics 2002 18:2* **18**, 191–196 (2002).

30. Tran, T. T., Bray, K., Ford, M. J., Toth, M. & Aharonovich, I. Quantum emission from hexagonal boron nitride monolayers. *Nature Nanotechnology 2015 11:1* **11**, 37–41 (2015).

31. Michler, P. *et al.* Quantum correlation among photons from a single quantum dot at room temperature. *Nature 2000 406:6799* **406**, 968–970 (2000).

32. De Mello Donegá, C., Bode, M. & Meijerink, A. Size- and temperature-dependence of exciton lifetimes in CdSe quantum dots. *Phys Rev B Condens Matter Mater Phys* **74**, 085320 (2006).

33. Labeau, O., Tamarat, P. & Lounis, B. Temperature Dependence of the Luminescence Lifetime of Single [Formula presented] Quantum Dots. *Phys Rev Lett* **90**, 4 (2003).

34. Bosco, L. *et al.* Thermoelectrically cooled THz quantum cascade laser operating up to 210 K. *Appl Phys Lett* **115**, (2019).

35. Dialynas, G. E. *et al.* Piezoelectric InAs (211)B quantum dots grown by molecular beam epitaxy: Structural and optical properties. *J Appl Phys* **108**, 103525 (2010).

36. Germanis, S. *et al.* Piezoelectric InAs/GaAs quantum dots with reduced fine-structure splitting for the generation of entangled photons. *Phys Rev B Condens Matter Mater Phys* **86**, 035323 (2012).

37. Germanis, S. *et al.* Enhanced Stark Tuning of Single InAs (211)B Quantum Dots due to Nonlinear Piezoelectric Effect in Zincblende Nanostructures. *Phys Rev Appl* **6**, 014004 (2016).

38. Dialynas, G. E. *et al.* Anti-binding of biexcitons in (2 1 1)B InAs/GaAs piezoelectric quantum dots. *Physica E Low Dimens Syst Nanostruct* **40**, 2113–2115 (2008).

39. Germanis, S. *et al.* Recombination dynamics in piezoelectric (2 1 1)B InAs quantum dots. *Microelectron Eng* **112**, 179–182 (2013).

40. Chatzarakis, N. G. *et al.* Redshifted biexciton and trion lines in strongly confined (211)B InAs/GaAs piezoelectric quantum dots. *J Appl Phys* **131**, 123101 (2022).

41. Treu, J. *et al.* Substrate orientation dependent fine structure splitting of symmetric In(Ga)As/GaAs quantum dots. *Appl Phys Lett* **101**, 22102 (2012).

42. Larqué, M., Robert-Philip, I. & Beveratos, A. Bell inequalities and density matrix for polarization-entangled photons out of a two-photon cascade in a single quantum dot. *Phys Rev A* **77**, 042118 (2008).

43. Schliwa, A., Winkelnkemper, M., Lochmann, A., Stock, E. & Bimberg, D. In(Ga)As/GaAs quantum dots grown on a (111) surface as ideal sources of entangled photon pairs. *Phys Rev B Condens Matter Mater Phys* **80**, 161307 (2009).

44. Juska, G. *et al.* Conditions for entangled photon emission from (111)B site-controlled pyramidal quantum dots. *J Appl Phys* **117**, 134302 (2015).
45. Singh, R. & Bester, G. Nanowire quantum dots as an ideal source of entangled photon pairs. *Phys Rev Lett* **103**, 063601 (2009).
46. Versteegh, M. A. M. *et al.* Observation of strongly entangled photon pairs from a nanowire quantum dot. *Nature Communications 2014 5:1* **5**, 1–6 (2014).
47. Huber, T. *et al.* Polarization entangled photons from quantum dots embedded in nanowires. *Nano Lett* **14**, 7107–7114 (2014).
48. Paul, M. *et al.* Metal-organic vapor-phase epitaxy-grown ultra-low density InGaAs/GaAs quantum dots exhibiting cascaded single-photon emission at 1.3? μ m. *Appl Phys Lett* **106**, 122105 (2015).
49. Paul, M. *et al.* Single-photon emission at 1.55 μ m from MOVPE-grown InAs quantum dots on InGaAs/GaAs metamorphic buffers. *Appl Phys Lett* **111**, 17 (2017).
50. N. G. Chatzarakis, S. Germanis, I. Thyris & N. T. Pelekanos. Unpublished data.
51. Brown, R. H. & Twiss, R. Q. Correlation between Photons in two Coherent Beams of Light. *Nature 1956 177:4497* **177**, 27–29 (1956).
52. Bernard, J., Fleury, L., Talon, H. & Orrit, M. Photon bunching in the fluorescence from single molecules: A probe for intersystem crossing. *J Chem Phys* **98**, 850–859 (1993).
53. Birner, S. *et al.* Nextnano: General purpose 3-D simulations. *IEEE Trans Electron Devices* **54**, 2137–2142 (2007).
54. Vurgaftman, I., Meyer, J. R. & Ram-Mohan, L. R. Band parameters for III–V compound semiconductors and their alloys. *J Appl Phys* **89**, 5815–5875 (2001).
55. Florini, N. *et al.* Structure, strain, and composition profiling of InAs/GaAs(211)B quantum dot superlattices. *J Appl Phys* **119**, 34304 (2016).
56. Varshni, Y. P. Temperature dependence of the energy gap in semiconductors. *Physica* **34**, 149–154 (1967).
57. Bayer, M. & Forchel, A. Temperature dependence of the exciton homogeneous linewidth in In0.60Ga0.40As/GaAs self-assembled quantum dots. *Phys Rev B* **65**, 041308 (2002).
58. Benyoucef, M., Rastelli, A., Schmidt, O. G., Ulrich, S. M. & Michler, P. Temperature dependent optical properties of single, hierarchically self-assembled GaAs/AlGaAs quantum dots. *Nanoscale Res Lett* **1**, 172–176 (2006).
59. Cavigli, L. *et al.* High temperature single photon emitter monolithically integrated on silicon. *Appl Phys Lett* **100**, 231112 (2012).

# 3 Redshifted Biexciton and trion lines in strongly confined (211)B InAs/GaAs piezoelectric quantum dots

## 3.1 Abstract

The emission lines of strongly-confined (211)B InAs/GaAs quantum dots (QDs), embedded in short-period GaAs/AlAs superlattices, are thoroughly characterized by a range of single-dot spectroscopy techniques, including cross-correlation photon-counting measurements. Contrary to what is expected for a piezoelectric QD system, the single-dot biexciton line is found red-shifted with respect to the exciton one by as many as 6 meV. This comes in striking contrast to previous reports on the same QD system, without additional confinement, where the biexciton lines always showed up at higher energies than the exciton, by 4 to 13 meV. In addition, two charged exciton lines are identified for the first time in a piezoelectric InAs-based QD. A positively-charged ($X^+$) and a negatively-charged ($X^-$) trion line are observed 1.5 meV and 7.5 meV below the neutral exciton line, respectively. These results pave the way to an enhanced understanding of the excitonic transitions in (211)B QDs and highlight the possible role of strong confinement and accompanying correlation effects as a means to tailor the transition energies of multi-particle states in semiconductor QDs.

## 3.2 Introduction

Since the first observation of sharp emission lines in the micro-photoluminescence (μ-PL) spectra of one or few QDs[1,2], there have been numerous reports in the literature underscoring the complexity of single-dot emission spectra. Among the plethora of possible multi-particle lines that can be observed in a QD, the most characteristic ones are the neutral exciton (X), the biexciton (XX), and the positively-charged ($X^+$) or negatively-charged ($X^-$) trions, respectively. The general trend regarding biexcitons in InAs/GaAs QDs grown along the (100) orientation is that for relatively "deep" QDs emitting below 1.3 eV, the XX lines appear at lower energy than X, by 2-3 meV, forming a "binding" XX state[3–5]. On the other hand, for "shallow"

QDs emitting above 1.3 eV, the XX lines become "anti-binding", appearing on the high energy side of X by an energy difference between 0.4 to 4 meV[6–9].

## 3.3 Coulomb interaction

### 3.3.1 Energy correction of X-XX

A qualitative explanation for this behavior is that in "shallow" QDs, correlation and exchange interaction effects are negligible, as the higher-excited electronic states of the QD, are pushed out of the dot by confinement, forming extended states into the wetting layer (WL). In such circumstance, the XX energy position with respect to the X line is essentially determined by direct Coulomb interaction between the additional quasiparticles forming the biexciton[9]. Introducing the Coulomb interaction energy terms $J_{ij}$ between the $i_{th}$ and $j_{th}$ electron or hole inside the dot That describes the energy exchange of a particle $i$ with wavefunction $\Psi$ under the influence of the potential $V$ of the particle $j$. By using the Poisson approach [10] the exchange integral can be written:

$$J_{ij} = q_i \int d\boldsymbol{r} |\boldsymbol{\Psi}_i|^2 V_j \,, \qquad 3\text{-}1$$

$$q_j \left|\boldsymbol{\Psi}_j\right|^2 = \epsilon_0 \nabla \cdot (\epsilon_s \nabla V_j)$$

The magnitude of $J$ depends on the particle type being repulsive for $J_{ee}$ or $J_{hh}$ and attractive for $J_{eh}$. Also, the interaction depends on the spatial extend of the electron and hole wavefunctions inside the dot and the relative position of their orbitals. **Figure 3.1a** shows the magnitude of each term according to the relative position of the probability clouds. The net Coulomb correction to the XX energy with respect to X can be written as $J_{hh} + J_{ee} - 2|J_{eh}|$. In most truncated-pyramidal dots, we expect that $J_{hh} > |J_{eh}| > J_{ee}$, based on the much heavier hole mass. Moreover, in truncated InAs QDs, $J_{hh} + J_{ee} \gtrsim 2|J_{eh}|$, which leads to a slightly positive Coulomb correction and the appearance of the XX line on the high-energy side of X, by a few meV[9,10]. Contrarily, for "deep" QDs, correlation and exchange interaction effects can no longer be neglected, tending to compensate the repulsive Coulomb interaction and leading eventually to "binding" XX states.

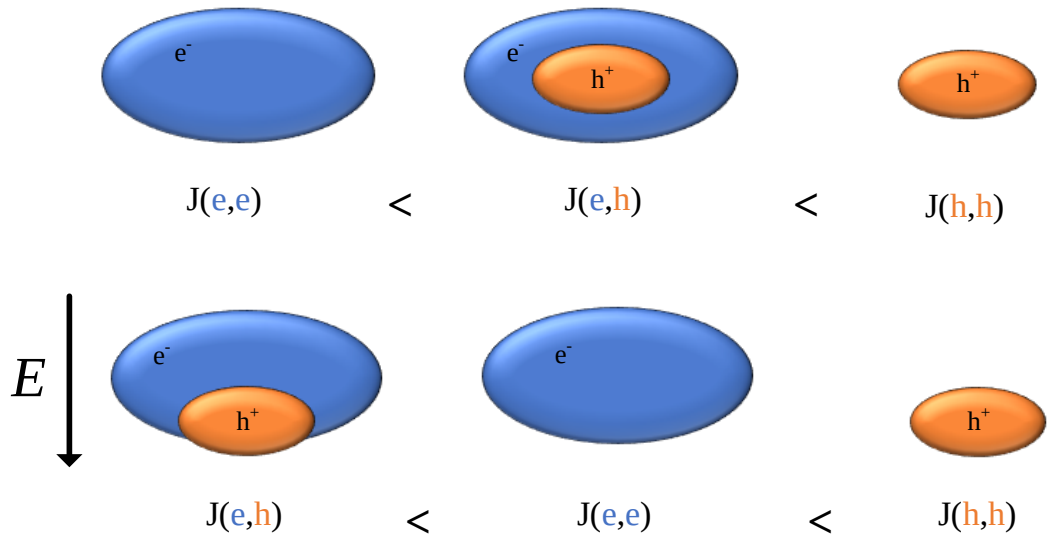


*Figure 3.1: Magnitude of the coulomb interaction according to the electron and hole wavefunction size and mutual position a) without electric field and b) with electric field.*

### 3.3.2 Energy correction of trions

Similar reasoning applies to the charged exciton states of (100) InAs/GaAs QDs. Experimentally, the $X^+$ lines are systematically blue-shifted with respect to X, with the energy difference becoming smaller as the QD size increases[11]. On the other hand, the $X^-$ lines are always red-shifted with respect to X and this energy difference increases with increasing QD size. This behavior is straightforward to understand in "shallow" QDs, where only direct Coulomb terms are important. In particular, the Coulomb correction for the $X^+$ line is $J_{hh} - |J_{eh}|$, which as previously noted is always positive in a truncated pyramid. Similarly, the Coulomb correction for the $X^-$ line is $J_{ee} - |J_{eh}|$, which is always negative, explaining the systematic observation of $X^-$ on the low energy side of X. With increasing QD size, correlation, and exchange effects step in and red-shift both the $X^+$ and $X^-$ lines with respect to X, in agreement with the experimental observations[11].

### 3.3.3 Advantages of polar orientations

Of particular interest to this work are InAs/GaAs QDs grown along a polar orientation, such as (111) or (211) [12,13]. In such crystallographic orientations, the QDs are piezoelectric (PZ), in the sense that they contain a strong PZ field along the growth direction. PZ QDs are appealing for single or entangled photon source applications due

to a number of reasons. First, the large X-XX energy splittings, which are possible in PZ QDs, as discussed below, minimize the spectral overlap of the X and XX lines with increasing temperature, enabling single photon emission operation at elevated temperatures [14]. Second, the PZ field along the QD growth axis is able to induce negligible fine structure splitting values of the X state [15–18], which are necessary for the generation of high-fidelity entangled photons [19]. Indeed, entangled photon emission has been observed in as-grown site-controlled pyramidal (111)B InGaAs/GaAs QDs [20,21], as well as InAsP QDs inserted in (111)-oriented InP nanowires [22,23]. Another interesting aspect of PZ QDs is their high sensitivity to external electric fields due to the quadratic nature of the Quantum-Confined Stark effect, giving rise to enhanced Stark tunings of their exciton lines and the feasibility of widely-tunable single photon sources [24].

### 3.3.4 Additional confinement in PZ QDs

Regarding biexciton lines in PZ QDs, large anti-binding energies can be expected as a consequence of the PZ field. Considering in particular truncated PZ QDs such as, for instance, epitaxially-grown GaN/AlN QDs [25,26] and (211)B InAs/GaAs QDs [13,27], the Coulomb terms order as $J_{hh} > J_{ee} > |J_{eh}|$, with the $|J_{eh}|$ term significantly decreasing due to the separation of the electron and hole wavefunctions by the PZ field as **Figure 3.1b** shows. This implies that, whenever correlation and exchange effects can be neglected in PZ QDs, the Coulomb correction to the XX energy will be amply positive and the XX line will appear blue-shifted and well separated from X. This has been verified experimentally in GaN/AlN c-axis-grown QDs with a reported anti-binding XX energy of ~35 meV [14], as well as in (211)B InAs/GaAs QDs with anti-binding energies ranging between 4 and 13 meV [17,24,28,29]. Up to this work, no trion lines have been unambiguously identified in PZ QDs. A common characteristic of all previous reports on the (211)B InAs/GaAs QD system is that the InAs QDs were embedded in relatively thick GaAs segments, a situation where the QD states feel solely the confinement of the surrounding GaAs barriers. In this chapter, a comprehensive single-dot spectroscopy study of a (211)B InAs QD which is *strongly-confined* by short-period GaAs/AlAs superlattices is presented. Contrary to expectations for a PZ QD, the XX line is now found red-shifted with respect to X, by as many as 6 meV. In addition, two trion lines are identified emitting from the same PZ dot: a positively-charged and a negatively-charged trion, with binding energies of 1.5 meV and 7.5 meV,

respectively. Our results strongly suggest the role of additional confinement and concomitant correlation effects, as a means to vary and control the energies of multi-particle levels in semiconductor QDs.

## 3.4 Sample fabrication and characterization

The sample studied here is the same sample (#1572) that showed single photon emission at 230K in previous chapter. Technical information about the design of the microcavity, the growth of the QDs and mesa creation for single dot spectroscopy can be found in chapter 2 of this thesis.

## 3.5 Experimental Techniques

For the optical characterization, the same PL and μPL setup described in the previous chapter was used. To read in details about these techniques, please refer to chapter 2 of this thesis.

### 3.5.1 Time Resolved Measurements

For the implementation of time-resolved PL (TRPL) and cross-correlation experiments, a tunable Ti:Sapphire laser is used for excitation, either in the femtosecond pulsed mode or in the continuous-wave (CW) mode. The specs of this laser can be found in chapter 2 at the autocorrelation section. In pulsed mode, the signal from an integrated photodiode is used to trigger the fast on-board single-photon counting module (SPCM) for the TRPL experiments (**Figure 3.2a**).

For the implementation of cross correlation experiments the setup of **Figure??** in the previous chapter, was modified so that two different emission lines from the same QD can be spectrally-filtered separately. For this reason, two different spectrometers were used as **Figure 3.2b** shows. The collected μ-PL signal is spitted by a 50:50 non-polarizing beam splitter before the spectrometers leading to the two Hanbury, Brown and Twiss (HBT) [30] arms.

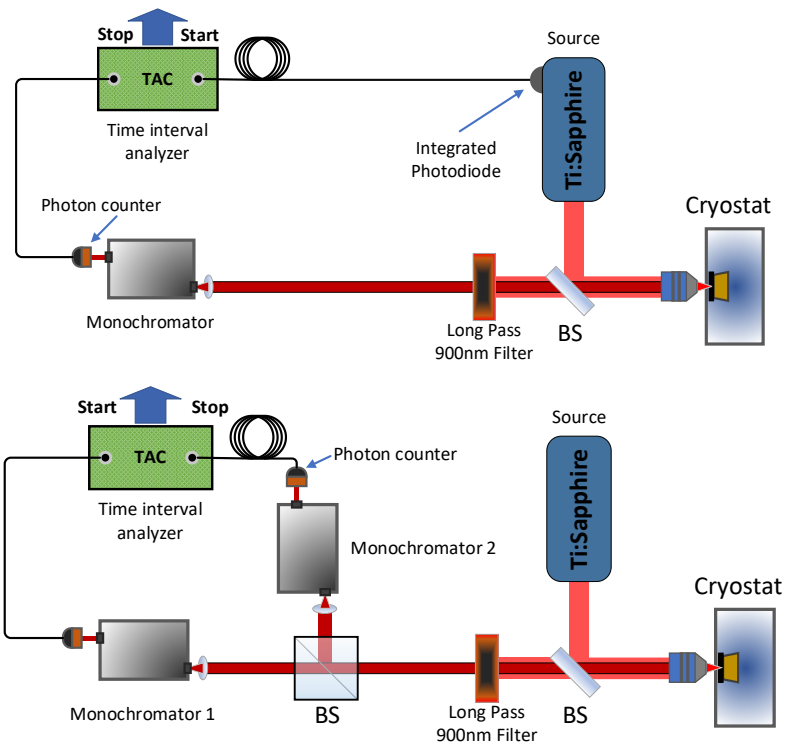


*Figure 3.2: a) Schematic illustration of the TPRL setup used for lifetime measurements b) schematic illustration of the HBT setup used for cross correlation experiments.*

After splitting, half of the signal is directed through a primary 0.75 m spectrograph, equipped with a 1200 gr/mm grating, blazed at 750 nm, where μ-PL spectra can be recorded by a high quantum efficiency back-thinned liquid Nitrogen-cooled charge-coupled device (CCD). Alternatively, the side exit of the same spectrograph is used for spectral filtering, with the slit opening defining the spectral window of observation, which can be as small as 50 μeV. The other half of the signal is filtered with a secondary 0.2 m spectrograph equipped with a 1200 gr/mm grating blazed at 750 nm. The signal at the two spectrograph exits is recorded using the same fast Silicon Single Photon Avalanche Photodiodes (SPADs) as previously described in chapter 2 triggering the same Single Photon Counting module (SPC-130).

## 3.6 Direct evidence of multiexcitonic lines from a single QD

In the previous chapter a good QD candidate with high excitonic emission intensity was found on sample #1572. We were able to obtain single photon emission at elevated temperature utilizing the Purcell effect inside the cavity, in combination with large X-XX energy difference. In the following section, the origin of the

multiexcitonic lines, which were not properly justified previously in chapter 2 will be thoroughly investigated and identified.

### 3.6.1 Determination of multiexcitonic lines

Power-dependent μ-PL spectra from a single QD contained in a mesa structure, under pulsed excitation at 77 K, are presented in **Figure 3.3a.** The spectra contain four main peaks, marked according to their final assignment. All four peaks derive from the same QD, and their final identification was based on polarization-resolved and cross-correlation measurements, presented in this chapter, exhibiting clear cascade or anti-bunching relation between them, which would be impossible to observe if the peaks came from different QDs.

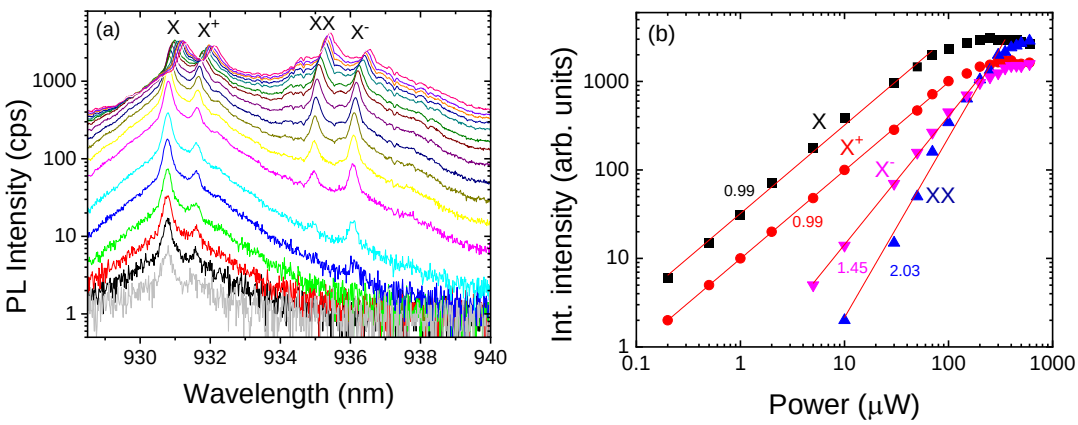


*Figure 3.3: (a) μ-PL spectra at T=77 K from a single strongly-confined (211)B InAs/GaAs QD with increasing excitation power from 200 nW to 6 μW. Several multi-particle exciton lines are denoted according to their assignment discussed in the text. (b) Integrated μ-PL intensity of corresponding emission lines versus excitation power. The numbers denote the exponent of the respective fitting curve.*

At high powers, the intensities of the various peaks saturate, as expected for single dot emission. All peaks red-shift by ~0.5 nm at high powers, due to a photo-induced heating of the sample by 1 or 2 degrees. The integrated-intensity versus power curves for all peaks are plotted in **Figure 3.3b**. The solid curves running through the data points at low powers are best fits to the equation $I \propto P^b$, where $I$ is the intensity, $P$ the power of excitation, and $b$ the exponent which is characteristic of the emission process. The numbers next to each curve indicate the corresponding best-fitting exponent. The "X" and "$X^+$" peaks scale linearly with power and saturate at about the same power level, suggesting they are QD excitations containing a single electron-hole

pair. On the other hand, the linear and quadratic power dependence of the "X" and "XX" lines, respectively, is in perfect agreement with their assignment as neutral exciton and bi-exciton emission peaks. In keeping with this assignment is also the fact that the two peaks saturate at the same intensity level, as expected in QDs with negligible non-radiative processes [31]. Finally, the "$X^-$" line exhibits also an intermediate power law, with $b = 1.45$. Based on this and the fact that the "$X^+$" and "$X^-$" peaks seem to saturate at about the same intensity, one could be tempted to assign "$X^-$" as a positively charged "$XX^+$". However, this possibility is excluded on the basis of cross-correlation measurements as we show later in this section.

### 3.6.2 Polarization resolved measurements

To further investigate the origin of each peak, polarization resolved μPL is used. The spectra in **Figure 3.4a** are recorded using a fixed linear polarizer in front of the spectrograph and a broadband λ/2 wave-plate to rotate the polarization. The sample is oriented such that "zero" degrees correspond to a linear polarization parallel to the [011] crystallographic direction.

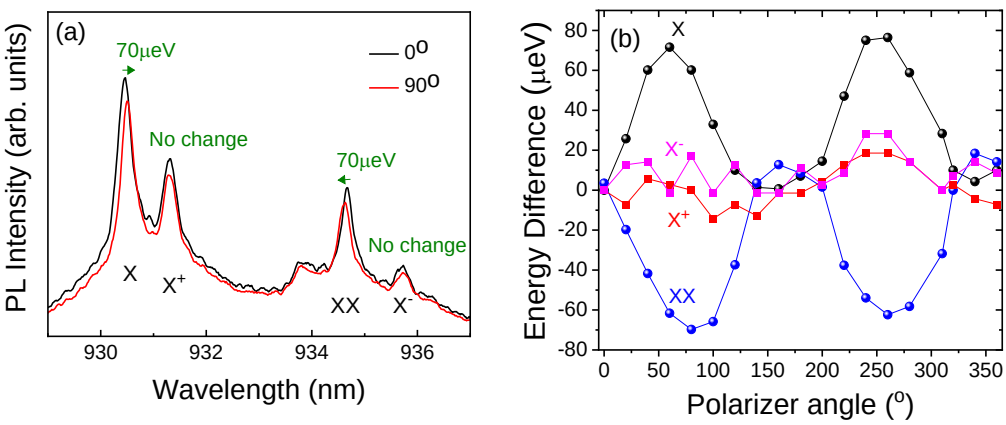


*Figure 3.4: (a) Vertical (0°) and horizontal (90°) polarization-dependent μ-PL spectra at T=77 K from the strongly-confined (211)B InAs/GaAs QD under study. The angle of 0° corresponds to the [011] crystallographic direction. (b) Energy shift of the various multi-particle lines as a function of linear polarization angle.*

Clearly, the X and XX emission peaks shift in opposite directions with polarization, according to the expected behavior of exciton and biexciton peaks, as cross-polarized doublets of same splitting but reversed polarization [9]. Here in this particular QD, the corresponding fine-structure splitting is 70 μeV, suggesting significant lateral anisotropy of the exciton wave functions in the dot. On the other

hand, the $X^+$ and $X^-$ peaks present no measurable polarization dependence, as shown in **Figure 3.4b**, in agreement with their assignment as trions, where the pairing of electron and hole spins cancels out the exchange interaction.

### 3.6.3 Time resolved photoluminescence measurements

In this section, the recombination dynamics of the various multi-particle lines under study will be investigated. TRPL decay measurements for all four spectral lines were performed using pulsed laser excitation at 730nm, which corresponds to an excitation above the WL emission energy. The obtained decay curves are presented in **Figure 3.5** in semi-logarithmic scale.

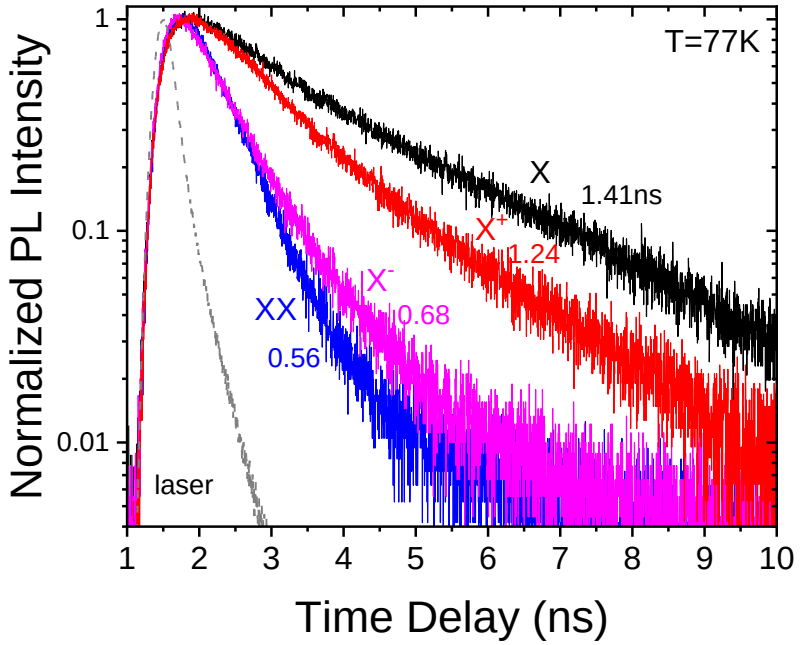


*Figure 3.5: Time-decay curves of the various multi-particle emission lines at 77 K from the same single (211)B InAs/GaAs QD. The instrument response to the excitation laser pulse is also shown in dashed line*

The numbers next to each curve correspond to the respective lifetimes in ***ns***, deduced by fitting the decay curves with single exponentials. The X-lifetime of 1.41 ns is very similar to the lifetimes reported in (100) InAs QDs [7,8], despite the PZ field in our case. This can be explained by the relatively small size of our dots, thwarting the ability of the PZ field to separate the electron and hole wave-functions and increase the lifetime. On the other hand, the XX-lifetime is ~2.5 times shorter than the excitonic one. Similar shortening factors have been observed in truncated (100) InAs/GaAs QDs

and were attributed to the absence of dark components in the XX-state along with the two possible recombination paths for the electron-hole pairs in the bi-exciton. The theoretical limit for lens-shaped InAs QDs was found $\tau_{XX} = \tau_X /4$ [32]. Regarding the trion lines, their lifetimes fall in-between those of X and XX, in good agreement with experimental [7] and theoretical [32] results on (100) InAs/GaAs QDs. The shorter lifetimes of the trions compared to neutral excitons is due to the absence of any dark state in the charged exciton.

### 3.6.4 Cross correlation measurements

In order to further validate the assignment of the discussed peaks, we resorted to cross-correlation measurements at 77 K, using a CW laser source at 730 nm and directing in the two arms of the HBT setup the spectral windows shown in **Figure 3.6a** for each peak. The obtained histograms in **Figure 3.6 b-e**, represent the second-order intensity correlation function $g^2(\tau)$ between the transition pairs indicated in each graph. When the XX line is used as a "start" and the X line as a "stop", a pronounced cross-bunching feature appears in **Figure 3.6(b)** around $\tau = 0$, in perfect agreement with a standard bi-exciton to exciton cascade process[8]. In this particular histogram, each SPAD received over $10^5$ counts per second and the integration time was about minutes. On the other hand, correlating the X and $X^+$ peaks, leads to a clear anti-bunching signature in **Figure 3.6(c)**, strongly suggesting that the QD intermittently captures and releases an excess carrier (hole), emitting at time intervals either as a charged exciton ($X^+$) or as a neutral exciton[7,33]. The reason we assign the $X^+$ line to a positively-charged exciton rather than a negatively-charged one, is that the Coulomb correction for the $X^+$ line is always larger than that of the $X^-$ line, based on the fact that $J_{hh} > J_{ee}$ , implying that the charged exciton line with the higher energy is always positively-charged. Comparing the PL intensities of the X and $X^+$ lines in **Figure 3.3a**, one may infer that the QD remains charged for about 25-30 % of the time. Interestingly, the cross-correlation $g^2(\tau)$ function between the XX (start) and the $X^+$ (stop) reveals again a cascade process (*cf.* **Figure 3.6d**), indicating that the bi-exciton may also cascade to the charged exciton, most likely via the efficient charging of the neutral exciton, mentioned above. Finally, in **Figure 3.6e** we observe a fine anti-bunching trace between the $X^+$ and $X^-$ peaks, in accordance with expectations for two differently-charged excitons of the same dot. It should be noted that this $X^+/X^-$ anti-bunching also excludes the

possibility of assigning the $X^-$ peak to a positively-charged bi-exciton, as in that case a clear cascade process leading to $X^+$ would have been expected.

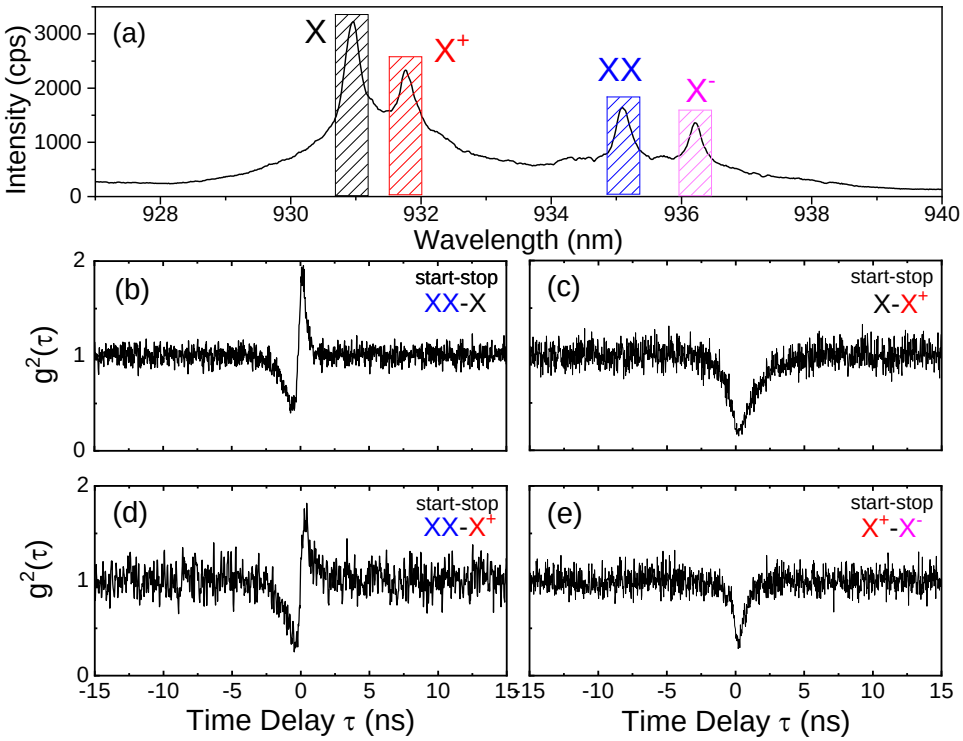


*Figure 3.6: (a) μ-PL spectrum at T=77K indicating the various QD emission lines analyzed by cross-correlation spectroscopy. (b)-(e) Coincidence counts histograms obtained at 77K using an HBT cross-correlation setup under continuous-wave excitation, representing the second order intensity correlation function g2(τ) between the indicated transition pairs.*

Based on the ensemble of experiments presented above, we have conclusively identified a set of multi-particle exciton lines in a strongly-confined (211)B InAs/GaAs QD, all of which were found red-shifted with respect to the neutral exciton one. Specifically, the "binding" energies for the $X^+$, XX and $X^-$ lines are 1.5 meV, 6 meV and 7.5 meV, respectively.

It should be mentioned that similar results have been reproduced on several single QDs of the same sample. Some of them are presented in the **Figure 3.7a** and **Figure 3.7b**. In both cases, the XX line appears at lower energy than X, in accordance with the main finding. For the relatively shallow QDs emitting around 870 nm in (a), the X-XX splitting is 1.7 meV and 2.7 meV from left to right. On the other hand, for the larger QD emitting around 960nm in (b), the X-XX energy is as large as 8.8 meV.

It should be noted here that the different power densities used in the two graphs is due to the varying excitation wavelength, which is 780 nm in (a) and 532 nm in (b).

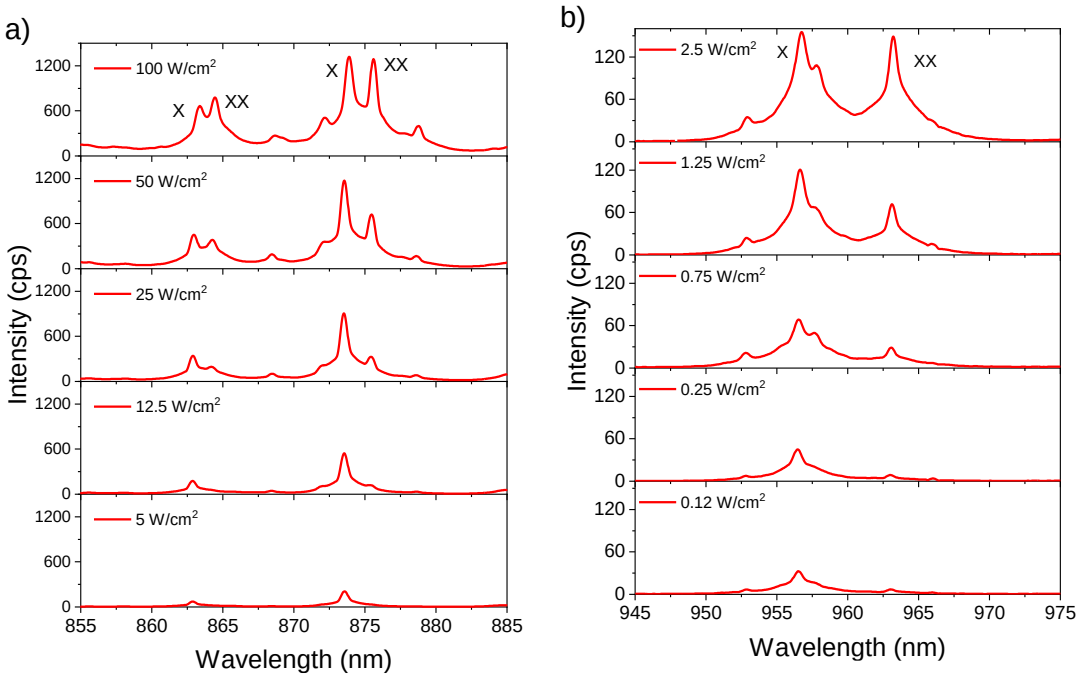


*Figure 3.7: Power-dependent μ-PL spectra at 77 K, obtained from two different mesas, showcasing several X-XX pairs from QDs of varying size.*

### 3.6.5 Critical parameter in the modification sequence

Clearly, the observed energy sequence, $E_X > E_{X^+} > E_{XX} > E_{X^-}$ in the 4-line QD we studied thoroughly in this chapter, cannot be accounted for by considering merely Coulomb interaction effects. In a PZ QD, where $J_{hh} > J_{ee} > |J_{eh}|$, the Coulomb correction terms would produce instead the sequence, $E_{XX} > E_{X^+} > E_{X^-} > E_X$ [10,15]. We argue that correlation effects are somehow important in our strongly-confined QDs and are responsible for the modified sequence of the multi-particle lines. Based on previous works on (100) InAs/GaAs QDs [9–11], correlation effects are known to red-shift the bi-exciton and trion lines with respect to the neutral exciton line and could in principle account for the modified sequence.

The critical parameter determining when correlation effects enter into play and become important, is the energy difference ($\Delta E$) between the WL gap and the QD exciton. In the (100) InAs/GaAs QDs, correlation effects can be neglected in "shallow" QDs, where $\Delta E$ is smaller than 100 meV. Similar $\Delta E$ values are typically encountered in standard (211)B InAs/GaAs QDs *without* additional confinement, justifying the systematic observation of anti-bound bi-excitons in these dots. However, in the

strongly-confined QD case of this work, $\Delta E$ is of the order of 250 meV, due to the much larger blue-shift of the WL transition, induced by the influence of the GaAs/AlAs SSL's. These large $\Delta E$ values are more than sufficient to allow for additional excited electron and hole levels inside the dots, accounting for the onset of significant correlation effects.

## 3.7 Conclusions

In this chapter the emission lines of strongly-confined (211)B InAs/GaAs QDs, in-between short-period GaAs/AlAs superlattices, have been carefully identified using various characterization techniques. The bi-exciton line (XX) is found red-shifted with respect to the neutral exciton (X) by **6 meV**, contrary to expectations for a piezoelectric QD system and previous reports on the same QDs ***without*** additional confinement. A positively-charged and a negatively-charged trion line have been also detected, 1.5 meV and 7.5 meV below the neutral exciton energy, respectively. The above relatively unexpected sequence of multi-particle lines can be attributed to enhanced correlation effects, enabled by the additional electron and hole levels inside the strongly-confined QDs. These results suggest an appealing mechanism to control the transition energies of a single QD by appropriate band-gap engineering of the surrounding barriers. It is important to note that this mechanism not only relates to the particular case of (211)B InAs QDs, but can be applied to any semiconductor QD system, including for instance the standard (100) InAs/GaAs QDs.

# References


1. Marzin, J. Y., Gérard, J. M., Izraël, A., Barrier, D. & Bastard, G. Photoluminescence of Single InAs Quantum Dots Obtained by Self-Organized Growth on GaAs. *Phys Rev Lett* **73**, 716 (1994).
2. Brunner, K., Abstreiter, G., Böhm, G., Tränkle, G. & Weimann, G. Sharp-Line Photoluminescence and Two-Photon Absorption of Zero-Dimensional Biexcitons in a GaAs/AlGaAs Structure. *Phys Rev Lett* **73**, 1138 (1994).
3. Bayer, M., Stern, O., Hawrylak, P., Fafard, S. & Forchel, A. Hidden symmetries in the energy levels of excitonic 'artificial atoms'. *Nature 2000 405:6789* **405**, 923–926 (2000).
4. Finley, J. J. *et al.* Observation of multicharged excitons and biexcitons in a single InGaAs quantum dot. *Phys Rev B* **63**, 161305 (2001).
5. Baier, M., Findeis, F., Zrenner, A., Bichler, M. & Abstreiter, G. Optical spectroscopy of charged excitons in single quantum dot photodiodes. *Phys Rev B* **64**, 195326 (2001).
6. Landin, L. *et al.* Optical investigations of individual InAs quantum dots: Level splittings of exciton complexes. *Phys Rev B* **60**, 16640 (1999).
7. Thompson, R. M. *et al.* Single-photon emission from exciton complexes in individual quantum dots. *Phys Rev B* **64**, 201302 (2001).
8. Moreau, E. *et al.* Quantum Cascade of Photons in Semiconductor Quantum Dots. *Phys Rev Lett* **87**, 183601 (2001).
9. Rodt, S. *et al.* Repulsive exciton-exciton interaction in quantum dots. *Phys Rev B* **68**, 035331 (2003).
10. Schliwa, A., Winkelnkemper, M. & Bimberg, D. Few-particle energies versus geometry and composition of In x Ga 1-x As/GaAs self-organized quantum dots. *Phys Rev B Condens Matter Mater Phys* **79**, 075443 (2009).
11. Rodt, S., Schliwa, A., Pötschke, K., Guffarth, F. & Bimberg, D. Correlation of structural and few-particle properties of self-organized InAs GaAs quantum dots. *Phys Rev B Condens Matter Mater Phys* **71**, 155325 (2005).
12. Stock, E. *et al.* Single-photon emission from InGaAs quantum dots grown on (111) GaAs. *Appl Phys Lett* **96**, 93112 (2010).
13. Dialynas, G. E. *et al.* Piezoelectric InAs (211)B quantum dots grown by molecular beam epitaxy: Structural and optical properties. *J Appl Phys* **108**, 103525 (2010).

14. Kako, S. *et al.* A gallium nitride single-photon source operating at 200 K. *Nature Materials 2006 5:11* **5**, 887–892 (2006).
15. Schliwa, A., Winkelnkemper, M., Lochmann, A., Stock, E. & Bimberg, D. In(Ga)As/GaAs quantum dots grown on a (111) surface as ideal sources of entangled photon pairs. *Phys Rev B Condens Matter Mater Phys* **80**, 161307 (2009).
16. Singh, R. & Bester, G. Nanowire quantum dots as an ideal source of entangled photon pairs. *Phys Rev Lett* **103**, 063601 (2009).
17. Germanis, S. *et al.* Piezoelectric InAs/GaAs quantum dots with reduced fine-structure splitting for the generation of entangled photons. *Phys Rev B Condens Matter Mater Phys* **86**, 035323 (2012).
18. Treu, J. *et al.* Substrate orientation dependent fine structure splitting of symmetric In(Ga)As/GaAs quantum dots. *Appl Phys Lett* **101**, 22102 (2012).
19. Larqué, M., Robert-Philip, I. & Beveratos, A. Bell inequalities and density matrix for polarization-entangled photons out of a two-photon cascade in a single quantum dot. *Phys Rev A* **77**, 042118 (2008).
20. Mohan, A. *et al.* Polarization-entangled photons produced with high-symmetry site-controlled quantum dots. *Nature Photonics 2010 4:5* **4**, 302–306 (2010).
21. Juska, G. *et al.* Conditions for entangled photon emission from (111)B site-controlled pyramidal quantum dots. *J Appl Phys* **117**, 134302 (2015).
22. Versteegh, M. A. M. *et al.* Observation of strongly entangled photon pairs from a nanowire quantum dot. *Nature Communications 2014 5:1* **5**, 1–6 (2014).
23. Huber, T. *et al.* Polarization entangled photons from quantum dots embedded in nanowires. *Nano Lett* **14**, 7107–7114 (2014).
24. Germanis, S. *et al.* Enhanced Stark Tuning of Single InAs (211)B Quantum Dots due to Nonlinear Piezoelectric Effect in Zincblende Nanostructures. *Phys Rev Appl* **6**, 014004 (2016).
25. Widmann, F. *et al.* Blue-light emission from GaN self-assembled quantum dots due to giant piezoelectric effect. *Phys Rev B* **58**, R15989 (1998).
26. Rouvière, J. L., Simon, J., Pelekanos, N., Daudin, B. & Feuillet, G. Preferential nucleation of GaN quantum dots at the edge of AlN threading dislocations. *Appl Phys Lett* **75**, 2632–2634 (1999).
27. Florini, N. *et al.* Structure, strain, and composition profiling of InAs/GaAs(211)B quantum dot superlattices. *J Appl Phys* **119**, 34304 (2016).

28. Dialynas, G. E. *et al.* Anti-binding of biexcitons in (2 1 1)B InAs/GaAs piezoelectric quantum dots. *Physica E Low Dimens Syst Nanostruct* **40**, 2113–2115 (2008).

29. Germanis, S. *et al.* Recombination dynamics in piezoelectric (2 1 1)B InAs quantum dots. *Microelectron Eng* **112**, 179–182 (2013).

30. Brown, R. H. & Twiss, R. Q. Correlation between Photons in two Coherent Beams of Light. *Nature 1956 177:4497* **177**, 27–29 (1956).

31. Robert, I., Moreau, E., Gayral, B., Gérard, J. M. & Abram, I. Tailoring photon emission statistics of a single quantum box for quantum communications. *Physica E Low Dimens Syst Nanostruct* **13**, 606–609 (2002).

32. Narvaez, G. A., Bester, G. & Zunger, A. Pressure effects on neutral and charged excitons in self-assembled (In,Ga)As GaAs quantum dots. *Phys Rev B Condens Matter Mater Phys* **72**, 041307 (2005).

33. Finley, J. J. *et al.* Charged and neutral exciton complexes in individual self-assembled In ( Ga ) As quantum dots. *Phys Rev B* **63**, 073307 (2001).

# 4 Plasmonic effect on GaAs NWs

## 4.1 Abstract

In this chapter we present the μ-PL and TRPL results on GaAs/AlGaAs and GaAs/InAlAs NWs. The NWs were transferred on top of gold-patterned templates, to investigate the plasmonic resonance effect of the metal to the semiconductor NW. To controllably vary the relative distance between the gold surface and the NW emitter, $HFO_2$ layers of varying thickness were deposited on the gold by atomic layer deposition (ALD) method. The PL measurements showed a ~45-fold enhancement in the PL signal and a two times faster lifetime for NWs having no spacer between the metal and the NW. The radiative enhancement fades away with increasing spacer thickness.

## 4.2 Introduction

When light interacts with electron plasma waves located on a metal surface, Surface Plasmons (SPs) can be created, which are capable of generating an enhanced local electromagnetic field that can significantly influence the optical properties of semiconducting emitters located near the metal [1–4]. During the last years, great effort has been made trying to improve the PL efficiency of semiconductors using the surface plasmon enhanced electromagnetic field[5–9]. Generally, there are two conditions that must be met in order to achieve interaction between the emitter and the surface plasmon resonance[10–12]. First, the energy of the SP should match the emission energy of the photons from the semiconductor. In this case, the electromagnetic field which is generated from the oscillation of the charge density of the electrons, becomes resonant with the emitter's photons, providing an effective channel for energy transfer between the metal and the semiconductor. Second, the distance between the emitter and the metal surface should be sufficient to suppress any energy loss of the nonradiative energy transfer from the semiconductor to the metal.

During the last two decades, the metal-semiconductor or metal-dielectric-semiconductor hybrid structures have proved to be good candidates for enhancing the PL of semiconductors on the basis of surface plasmon resonance (SPR). At present, a great number of works on structures such as thin films[13], dye molecules[14], quantum dots[5,10,11,15–18], core-shell NC heterostructures[11,12,19,20] and semiconductor NWs [21–24]

reported the realization of PL enhancement based on SPR. In the case of NWs the realization has been made by covering the NWs with Au nanoparticles[22,23,25], thin film deposition on the NW [26] and even creating a metal cavity around the NW [24]. The unique one-dimensional structure and versatile chemical properties of NWs make them excellent candidates as advanced photonic and electronic components[27–34]. Toward this end, improving the PL emission and tailoring their optoelectronic properties is of great significance for integrated nanophotonic devices and also for electronic circuits.

In this work, GaAs/AlGaAs and GaAs/InAlAs core-shell NWs are transferred on prepatterned substrates with 100nm-thick gold metal pads by using a simple mechanical transfer method. Hafnium dioxide ($HFO_2$) was used to adjust accurately the distance between the NW and the metal pad. PL measurements showed up to a~45-fold enhancement in the band-edge emission of the GaAs core and the results from lifetime measurements revealed almost ~2x faster carrier recombination when the $HFO_2$ thickness was null. Such hybrid metal-semiconductor system not only provides a novel and simple system to investigate the exciton-plasmon coupling but also paves the way for novel quantum emitters with enhanced characteristics.

## 4.3 Experimental techniques

### 4.3.1 NW growth

Two different samples were used in this thesis with code names 222 and D0487, both grown by molecular beam epitaxy. The sample 222 was grown in our facilities at Microelectronics Research Group and the sample D0487 was grown by our colleagues in HZDR. The NWs of **sample 222** are core–shell GaAs/AlGaAs NWs grown on n-type Si (111) substrates via the Ga-assisted Vapor-Liquid-Solid (VLS) mechanism, in a VG80 MBE system, using an As effusion cell. Before the GaAs growth, the untreated substrate was annealed in situ at ≈730 °C to form pores in the native $SiO_2$ of the substrate, acting as nucleation centers. After annealing, the growth temperature was ramped down to 620 °C, and the GaAs core NWs were grown for 10 min, using ≈0.5 ML/s Ga flux and an As/Ga flux ratio of ~ 2. These conditions resulted to an average NW diameter and length of 75 nm and 2.5 μm respectively, with NW density of ~$10^8$ $cm^{-2}$. The Ga droplets on the NW tips were then consumed by exposing the sample to As flux for 3 min For the $Al_{0.3}Ga_{0.7}As$ shell, the As-to-Ga flux ratio was adjusted to about 4 and the growth temperature was kept unchanged, while the growth time was 10

min leading to a shell thickness of 10nm in order to protect the shell surface from oxidation, a GaAs over-shell a few nm thick was grown around the NWs. SEM images of the grown NWs are shown in **Figure 4.1**. A particularity of the "222" NWs is that the AlGaAs growth does not only lead to a conformal shell around the GaAs core, but in addition, due to probable re-appearance of a Ga-droplet on the top of the NWs activating the VLS process again, we end up with a long enough "tip" on top of the GaAs/AlGaAs fully grown NWs. This AlGaAs tip which is ~2-3μm long has its own spectral signature, as will be discussed in the optical characterization section, but our main focus remains the GaAs core emission of the NWs.

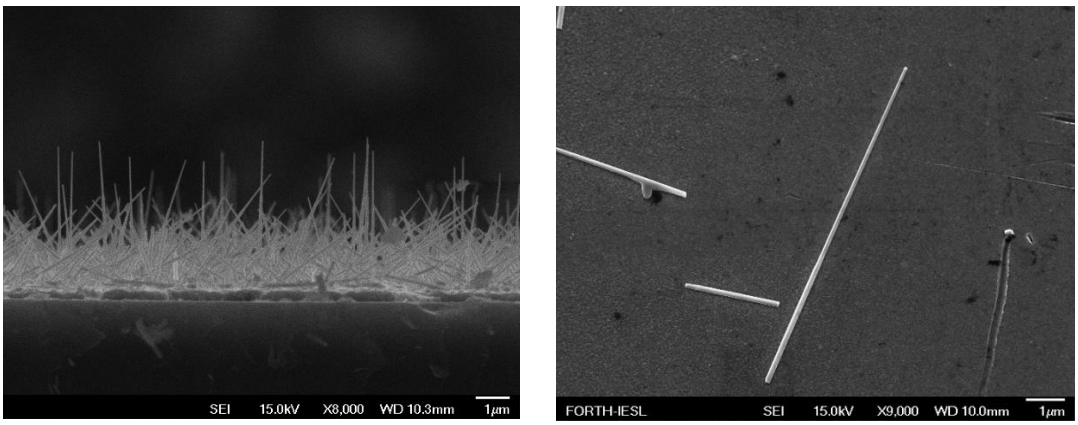


*Figure 4.1: a) SEM image of free-standing NWs on an n-type Si (111) substrate b) SEM image of a single NW transferred on a Si substrate.*

The sample **D0487** is a GaAs core NW sample, with GaAs QD axially-grown in the VLS mode in-between AlGaAs barriers. The growth was performed with Droplet-confined alternate pulsed epitaxy[35] (DCAPE) of GaAs/$Al_xGa_{1-x}As$ axial nanowire heterostructures directly on Si(111) substrates. For the GaAs core, 800 nm long and 60nm thick GaAs NWs were grown in DCAPE using $T_{gr}$=550 ◦C, and ratio Ga/As=2.6 with a growth rate of 1.95 ML/s, leading to a NW density of ~$10^8$/cm$^2$. The length of the grown nanowires was short, to minimize the lateral growth of the nanowire sidewalls and achieve thin-enough nanowires to radially confine the electrons. For the shell growth, after the second axial $Al_xGa_{1-x}As$ barrier is finished, the growth is interrupted by cooling the substrate down to 370˚C with As-presence inside the chamber. This leads to the axial growth of the core nanowires until the Ga droplets at the tips are consumed. After the stabilization of the substrate temperature, in about 20 minutes, a 40nm $In_{40\%}Al_{60\%}As$ shell was grown for 11.5 min by opening the In and Al shutters, in parallel to the As shutter. To avoid oxidation of the shell an $In_xGa_{1-x}As$

capping layer was grown for 1.5 minutes. The In, Al, Ga and As fluxes were $F_{In}$=0.30 ML/s, $F_{Al}$=0.47 ML/s, $F_{Ga}$=0.45 ML/s and $F_{As}$=2.45 ML/s for the shell growth. In **Figure 4.2a** an SEM image of the as-grown nanowires is shown in top view, whereas in **Figure 4.2b** an SEM image of transferred NWs indicates lengths of ~1μm.

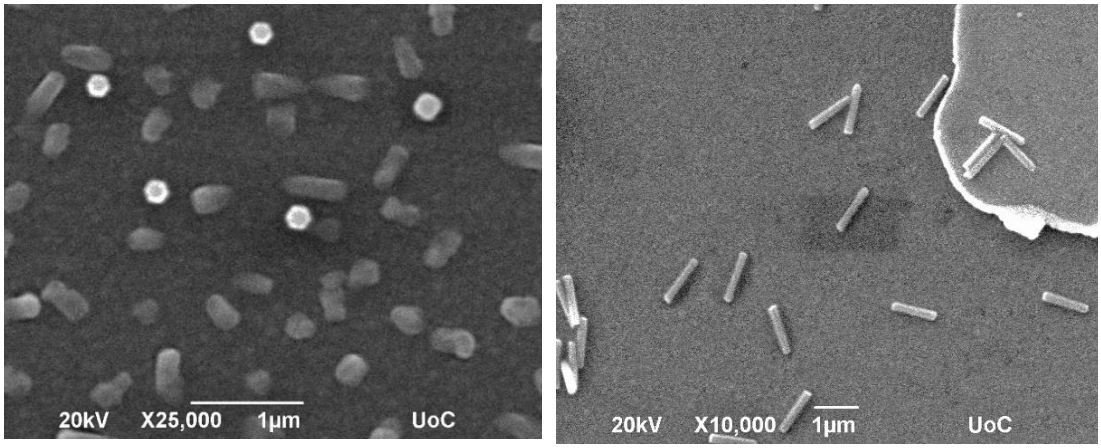


*Figure 4.2: a) SEM image of GaAs/InAlAs NWs standing vertically showing their hexagonal shape. b) SEM image of single GaAs/InAlAs NWs transferred on Si/$SiO_2$ substrate surface or Au metal pad (white color).*

### 4.3.2 Optical characterization of the as-grown nanowires

To optically characterize the samples the PL setup described in chapter 2 was used. As excitation source, a 325nm He-Cd CW laser was used to excite the NWs above their band gap. A long strip of sample was cut from the wafer to characterize the as-grown NWs in the radial direction from the center of the wafer to the edge.PL mapping was performed in both samples along the long strips which were loaded in the He-cooled cryostat. In **Figure 4.3**, different PL spectra from the center of the wafer (number 1) through the edge (number 12) are shown for both samples. From SEM measurements we know that all the areas of the sample have similar NW density except the areas at the edge where the NWs are less dense. **Figure 4.3a** shows the PL mapping of sample 222. There are two main emissions at ~780nm and ~830nm originating from the AlGaAs tip and shell and GaAs core respectively. We observe that all areas exhibit the same spectral features and an intensity that is slowly declining toward the edge of the wafer, suggesting an overall good uniformity of the NWs over the wafer. **Figure 4.3b** shows the PL mapping of the as-grown sample D0487. There is an emission from the InAlAs shell at ~700nm and a dominant emission at ~1000nm from the GaAs core. The homogeneity here is not so pronounced as we radially scan the sample. Please

notice the one order of magnitude lower PL intensity in the D0487 sample which can be partly attributed to the one order of magnitude lower NW density compared to the 222 sample.

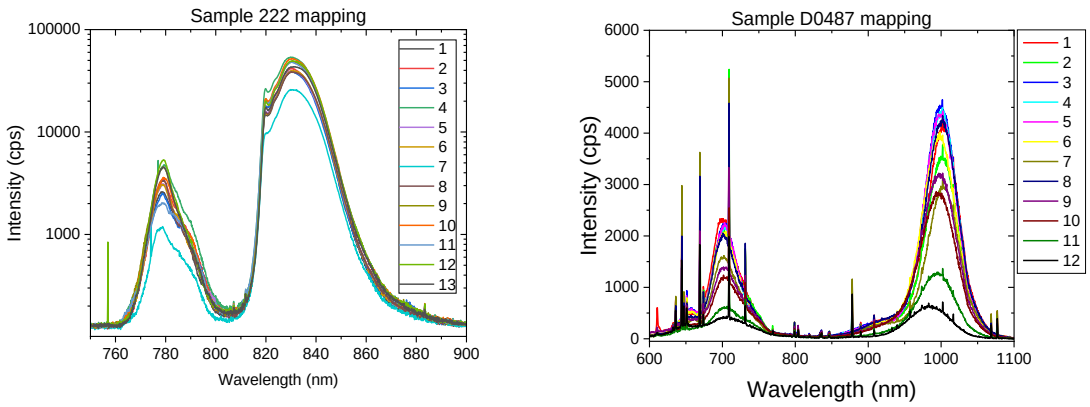


*Figure 4.3: Photoluminescence spectra from different areas of the cut piece used for mapping of sample a) 222 and b) D0487*

Based on the above results, we decided to transfer NWs from the areas 4 through 10 of both samples because these areas, are very similar in terms of PL intensity and spectral features. Details about the transfer method are given next.

### 4.3.3 NW transfer

To perform single NW spectroscopy the as-grown samples had to be transferred onto $SiO_2$/Si substrates, prepatterned with gold. The $SiO_2$ thickness is 290nm for enhanced optical contrast. To transfer the nanowires, a piece of wafer from the as-grown NWs is brought in contact with the target prepatterned substrate, as is schematically illustrated in **Figure 4.4 (bottom)**. By simply 'tapping' the back of the wafer piece, mechanical pressure is applied to the NWs which break and are thus successfully transferred on the surface of the prepatterned substrate. The pattern of the substrate contains letters and numbers which are very useful to identify and relocate a single NW of interest for μ-PL measurements or SEM imaging.

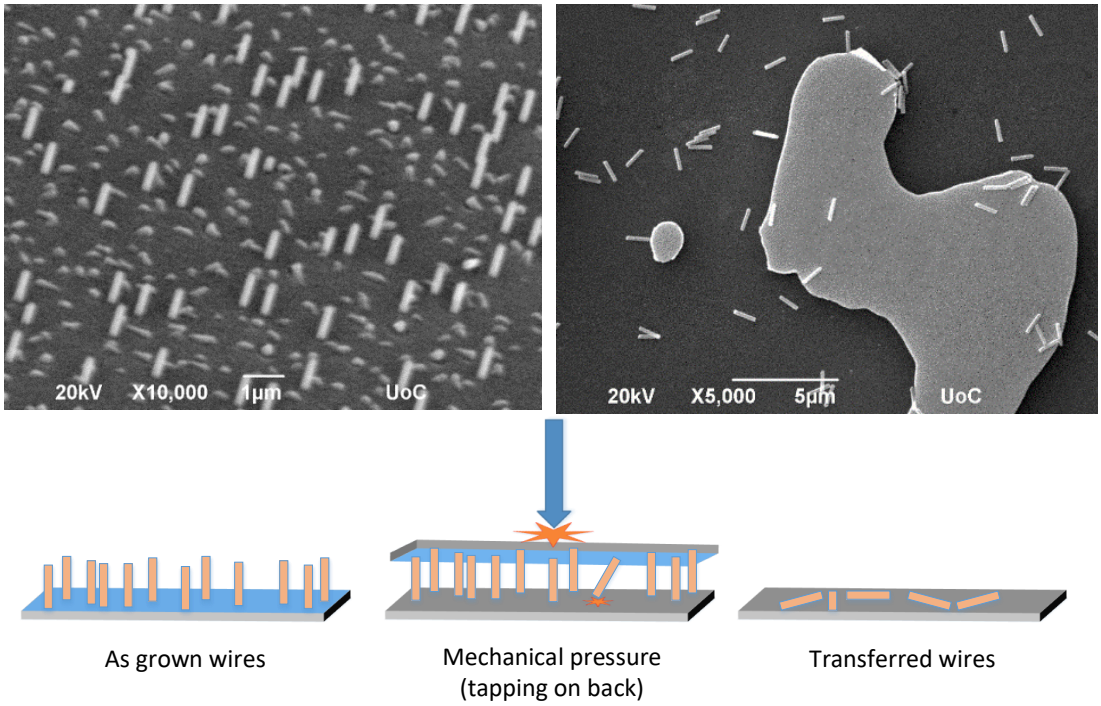


*Figure 4.4: (top) a) SEM image of as-grown GaAs/InAlAs nanowires b) SEM image of the same nanowires transferred on the surface of a prepatterned substrate. (bottom) Schematic illustration of the transfer process*

**Figure 4.4a** is an SEM image of as-grown NWs of sample D0487, standing vertically. In **Figure 4.4b** we show the SEM image of the NWs after the transfer process, laying down at random spots of the prepatterned substrate (the black in this picture is Si/$SiO_2$ and the grey is gold).

### 4.3.4 Optical characterization of the transferred nanowires

To optically characterize the transferred single NWs the μ-PL setup described in chapter 2 is used. As excitation source, a tunable Ti-Saphire laser is used tuned at 730nm in pulsed mode. A basic CCD camera is used to obtain real-time optical feedback of the excitation spot on each NW and to store images of the topological location for repeated experiments. The single NWs, as already mentioned in previous section, are randomly distributed after the transfer process, having random orientations as well. According to basic electromagnetic theory, when the excitation wavelength is comparable with the emitter dimensions (NW length), the electric field polarized perpendicular to the NW axis becomes attenuated inside the NW, by a factor of $2/(\varepsilon + 1)$, compared to the outside electric field[36], where $\varepsilon$ is the dielectric constant of the NW relative to its surrounding medium. On the other hand, for polarization parallel to the NW axis, no such attenuation occurs. Therefore, to induce maximum absorption of

the excitation laser, a λ/2 wave plate is used in the excitation path of the μ-PL setup adjusting the linear polarization of the laser parallel to the NW axis and obtain maximum absorption.

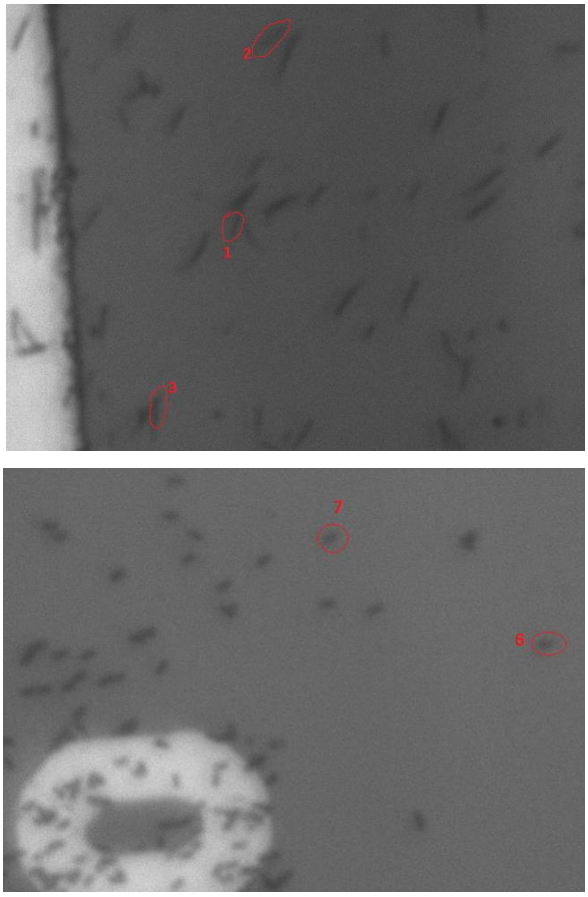


*Figure 4.5: Optical image from the μPL setup camera showing transferred single NWs from sample 222(upper panel) and sample D0487(lower panel). The white colored sections is Au. The red circles indicate single NWs which are named with numbers.*

In **Figure 4.5**, optical images from the camera of the μPL setup show many different nanowires randomly distributed on the surface of the prepatterned substrates. The upper figure shows random nanowires from sample 222 near or on the gold surface. The red circles correspond to single studied NWs and the given numbers is the name of each one. Thus, we can relocate a specific NW and perform multiple experiments. The shorter NWs of sample D0487 are shown in the bottom picture where the same numbering logic applies. These NWs cannot be distinguished as clearly because of the smaller length which is comparable with the microscope's objective resolution. For this reason, the selection procedure of a single NW is not only visual but is also spectral. The selected NWs must be isolated from others, something than can confirmed visually.

Then to verify that there is no neighbor NW next to the NW of interest, the PL spectrum is examined to not change while we "scan" the NW itself and the area around it.

Early experiments of single NW spectroscopy on both samples showed that the proximity of the metal with the emitter had serious impact on the PL intensity and the lifetimes of the carriers. More specifically the NWs that were randomly transferred on the gold surface of the prepatterned substrate showed not only increased intensity, but also smaller lifetimes compared to the NWs placed on silicon. **Figure 4.6b** shows the integrated emission intensity versus lifetime for the GaAs core of NWs from sample 222. The horizontal red and black dashed lines correspond to average PL intensities for the NWs on gold and on $SiO_2$/Si respectively. On the other hand, the vertical lines show the average lifetime values in each case. The average PL intensity is increased by a factor of ~12 in the case of NWs on gold compared to the NWs on $SiO_2$/Si. Also, the average lifetime of NWs on $SiO_2$/Si is ~5ns (black vertical dashed line) and for the gold (red vertical dashed line) is ~2.8ns which is almost half the lifetime of the NWs on $SiO_2$/Si.

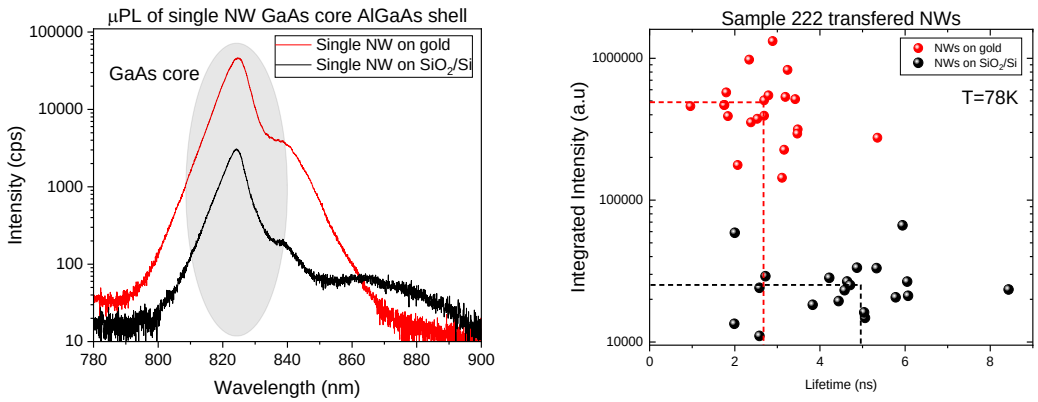


*Figure 4.6: a) µPL spectrum from a single nanowire of sample 222. The highlighted peak corresponds to the emission of interest from the GaAs core, b) Integrated intensity versus lifetime for the GaAs core emission only, from NWs which lie on gold (red) and silicon (black).*

The same behavior is observed in sample D0487 when comparing NWs on gold and on $SiO_2$/Si. In **Figure 4.7a** there is a µPL spectrum of a single NW from sample D0487 which shows emission from the axial GaAs dot inside the NW and the GaAs core at around 1050nm, which is the emission of our interest. In **Figure 4.7b** the emission from many NW cores have been measured and plotted versus their lifetime. The NWs on gold show a ~37-fold enhancement and their lifetimes are reduced almost by a factor of 2.

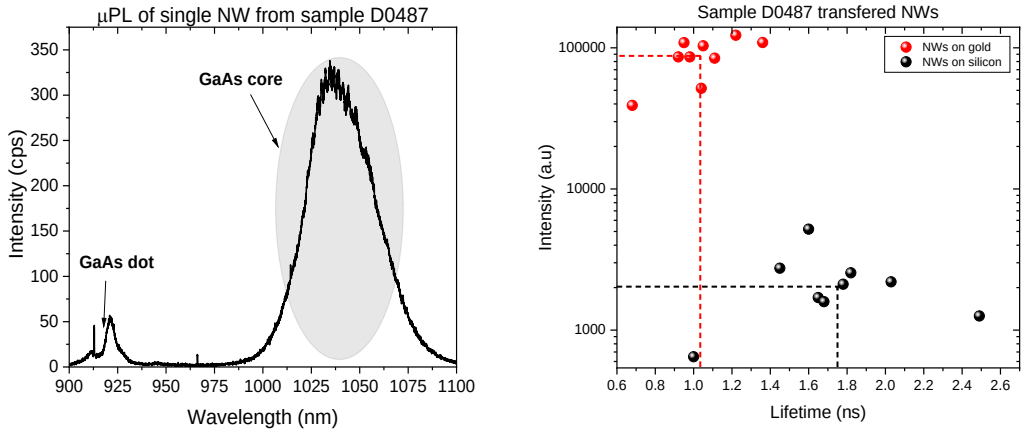


*Figure 4.7: a) µPL spectrum from a single nanowires of sample D0487. The highlighted peak corresponds to the emission of interest from the GaAs core, b) Integrated intensity versus lifetime for the GaAs core emission only from NWs that are on gold(red) and silicon(black).*

Please notice that the average µPL intensity of sample D0487 in **Figure 4.7b** is one order of magnitude lower than in sample 222 of **Figure 4.6b,** despite the fact that the excitation was 10 times larger (1mW for D0487 and 100µW for 222). This may be attributed mainly to the fact that the NWs of sample D0487 are physically much smaller and their emission range at ~1000nm is at the spectral limit of our CCD camera where the efficiency is ~6-7 times smaller compared to the 800nm range.

### 4.3.5 Manipulating the distance of the emitter from the metal

In order to investigate experimentally the plasmonic effect between the NWs and the surface of the metal as a function of their relative distance, 4 different core shell NW samples were prepared by our colleagues in Dresden with molecular beam epitaxy. The idea was to grow GaAs core NWs with different AlGaAs shell thicknesses that would act as a spacer between the GaAs core and the metal surface. The prepared samples were 3µm long NWs with ~30nm GaAs core and 10, 20, 40 and 80nm-thick $Al_{0.27}Ga_{0.33}As$ shells. We performed µPL measurements on single NWs from all these samples but the results were inconclusive. Their PL was very different as the AlGaAs shell in GaAs/AlGaAs NWs plays a very important role in passivating the GaAs core surface. Thus, with increasing the shell thickness, both the PL intensity and the lifetime increase strongly, and thus is difficult to decipher which effect is due to better passivation and which to plasmonic effect. For this reason, we decided to keep the NW shell thickness constant and find another way to increase the emitter-metal distance.

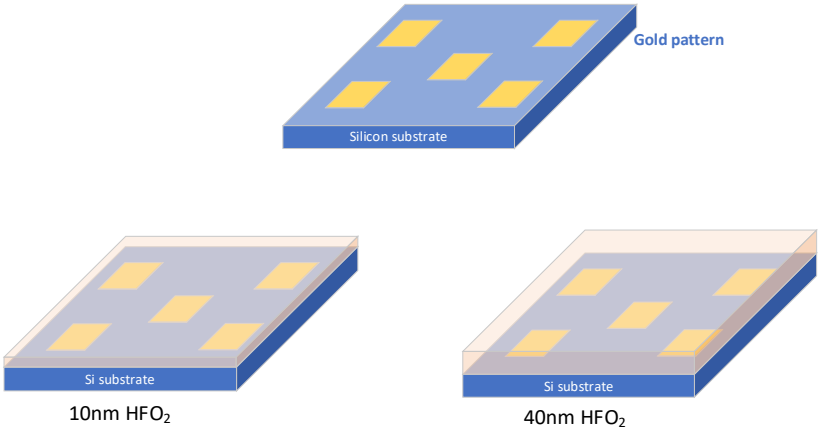


*Figure 4.8: Schematic illustration of the 3 different samples covered with $HFO_2$ of different thickness using the Atomic Layer Deposition (ALD) method.*

We used Atomic Layer Deposition (ALD) Method to deposit $HfO_2$ on top of the prepatterned substrates before the NW transfer. Two different thicknesses of 10nm and 40nm $HFO_2$ were deposited on top of the substrates acting as a spacer, increasing the distance of the NWs from the metal surface. Finally, two separate but similar set of experiments for the transferred NWs of samples D0478 and 222 were performed on the ALD deposited substrates in order to investigate the recombination dynamics of the carriers inside the NWs under the influence of the nearby metal surface. **Figure 4.9** is a schematic representation of the two types of single NWs, transferred on the ALD-deposited substrates in cross-section view.

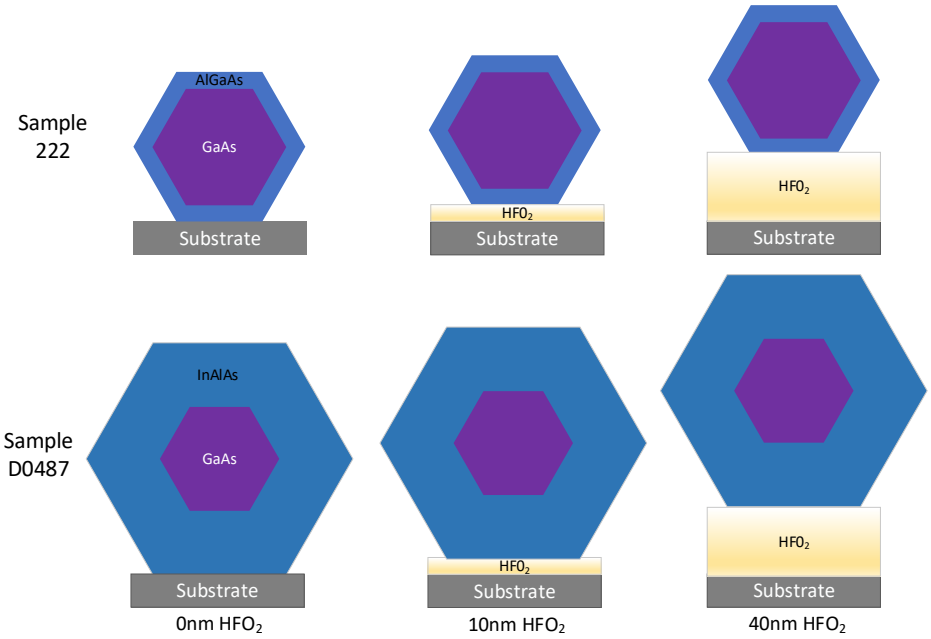


*Figure 4.9: Schematic representation of a single NW from sample 222 (upper panel) and sample D0487 (lower panel), transferred on substrates with different ALD depositions of $HfO_2$. The graph scale reflects the real layer dimensions.*

**Figure 4.10** shows a statistical measurement of different NW intensities versus their lifetime for the sample 222. The colored circles correspond to the NWs on gold and the star-shaped colored points to the NWs on silicon. The green, red and blue colors correspond to the sample with 40nm, 10nm and 0nm $HFO_2$ spacer. All the data points of NWs on silicon exhibit the same average integrated intensity of ~35000±4000 and a lifetime of ~4.8±0.4ns, independent of the spacer thickness. On the other hand, for the NWs on gold, with 40nm spacer, the average intensity is ~185000±22000 and the average lifetime is ~(4.9±0.5)ns. For the spacer thickness of 10nm and 0nm the average intensity is ~310000±29300 and ~480000±60000 with lifetimes ~(4.0±0.3)ns and ~(2.70±0.2)ns, respectively.

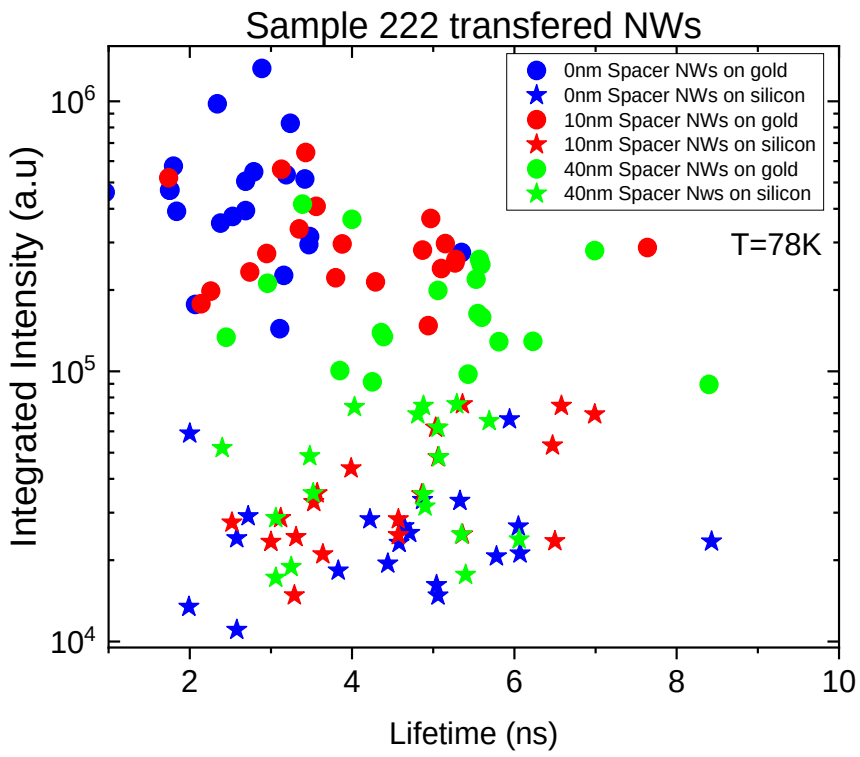


*Figure 4.10: Statistical measurements of Intensity versus Lifetime for many different nanowires of sample 222.*

In order to verify the results of sample 222, the NWs of sample D0487 were similarly transferred and characterized in terms of μPL intensity and lifetime values. **Figure 4.11** shows the statistical measurements on many single NWs of intensity versus lifetime. The results are similar to those obtained on sample 222. For all the NWs on silicon the average integrated intensity is ~2500±350 with lifetimes of ~(1.6±0.1)ns. With a 40nm and 10nm spacer, the NWs on gold show average intensity of

~43000±7700 and ~72115±14190 with lifetime values of ~(1.28±0.07)ns and ~(1.04±0.06)ns, respectively. Finally, with 0nm spacer the average intensity is ~88800±8241 with lifetime ~(0.92±0.1)ns.

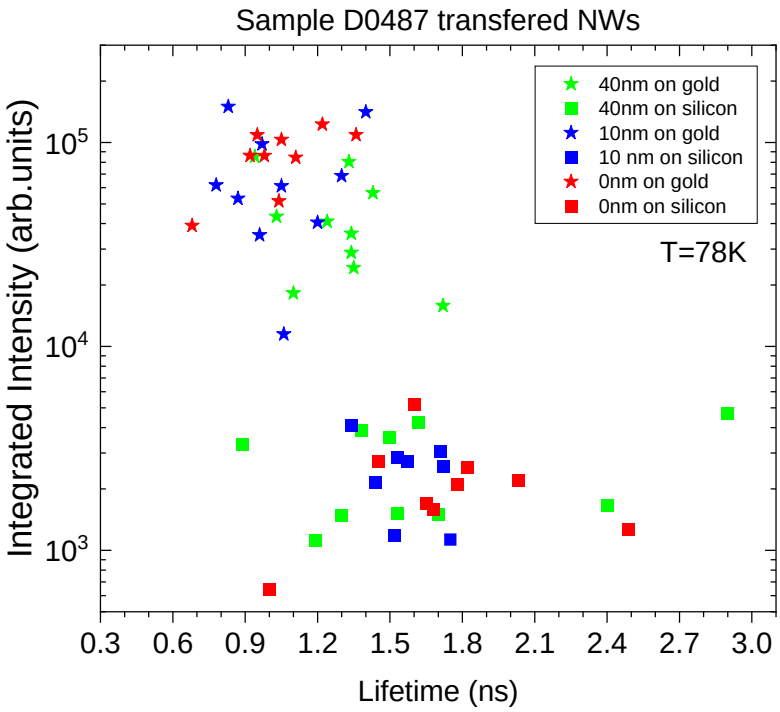


*Figure 4.11: Statistical measurements of Intensity versus Lifetime for many different nanowires of sample D0487*

The following tables summarize the main results from the two different NW samples:

| Sample 222 transferred NWs | | | | |
|---|---|---|---|---|
| | NWs on Gold | | NWs on Silicon | |
| | Integ. Intensity (arb. units) | Av. Lifetime (ns) | Integ. Intensity (arb. units) | Av. Lifetime (ns) |
| 0nm $HFO_2$ | 480000 ± 60000 | 2.7 ± 0.2 | 27441 ± 3033 | 4.9 ± 0.51 |
| 10nm $HFO_2$ | 310000 ± 29300 | 4.0 ± 0.3 | 38534 ± 4220 | 4.7 ± 0.3 |
| 40nm $HFO_2$ | 185000 ± 22000 | 4.9 ± 0.5 | 44263 ± 4750 | 4.8 ± 0.36 |

| Sample D0487 transferred NWs | | | | |
|---|---|---|---|---|
| | NWs on Gold | | NWs on Silicon | |
| | Integ. Intensity (arb. units) | Av. Lifetime (ns) | Integ. Intensity (arb. units) | Av. Lifetime (ns) |
| 0nm $HFO_2$ | 88800 ± 8241 | 0.94 ± 0.1 | 2220 ± 430 | 1.72 ± 0.13 |
| 10nm $HFO_2$ | 72115 ± 14190 | 1.04 ± 0.06 | 2468 ± 345 | 1.57 ± 0.05 |
| 40nm $HFO_2$ | 42972 ± 7700 | 1.28 ± 0.07 | 2700 ± 431 | 1.64 ± 0.19 |

From the data of the above tables, it is clear that the plasmons on the metal surface progressively enhance the optical properties of the NWs as the thickness of the spacer is reduced. For 0nm spacer, the PL intensity is enhanced by a factor of ~12 for the sample 222 and of ~37 for sample D0487. Their lifetimes in both cases are reduced to about half, compared to when they are on silicon.

At this point, it should be noted that the enhancement factor is different in the two NW samples. This could be attributed to the large length difference of the NWs (~1μm for sample D0487 and ~3.5μm for sample 222). If the incident beam of our experimental setup focuses down to a ~2μm spot-diameter, then we can assume that the longer nanowires cannot be excited properly leading to an enhanced electromagnetic field at the interface of the NW-gold only in the middle of the NW as **Figure 4.12** shows. On the other hand, the small in length NWs are smaller than the spot size of the incident beam, creating an enhanced electromagnetic field at the interface which has the same amplitude along the axis of the NW.

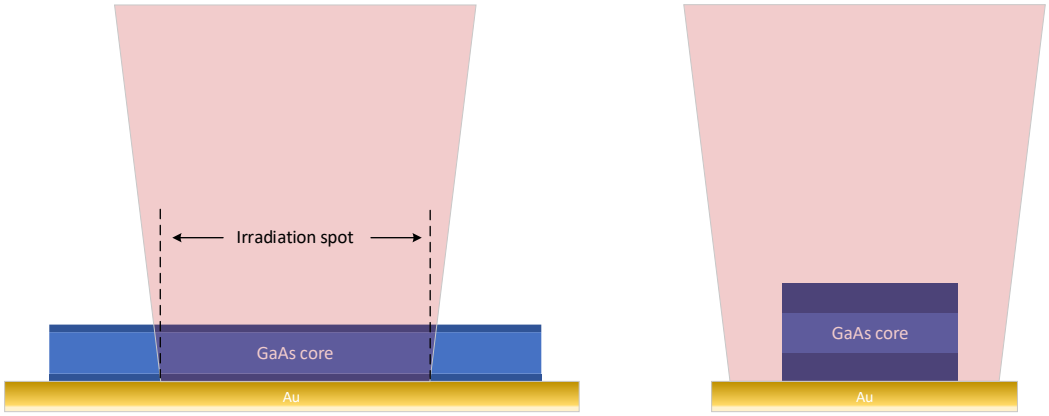


*Figure 4.12: Schematic representation of the excitation for sample 222(left) and sample D0487(right). The NWs of sample D0487 have small length and can be fully excited because the spot size of the objective lens is larger than the length of the NW in contrast with the NWs of sample 222 which are much larger.*

## 4.4 Radiative and non-radiative paths

In order to evaluate the influence of non-radiative effects in the emission characteristics of our NWs, temperature dependent PL and TRPL measurements were performed on single NWs on gold and on silicon. **Figure 4.13a** shows the integrated PL intensity from the GaAs core of a single NW from sample 222, located on gold (red dots) and from another NW of the same sample located on silicon (**black** dots). At low temperatures the PL intensity is almost one order of magnitude larger for the NW on gold, most likely due to the plasmonic resonance effect of the metal surface[37]. At higher temperatures, however, the PL enhancement drops to about a factor of ~4 at 250K. This

factor of 4 could be attributed to the plain mirror effect of the gold surface, possibly suggesting that the plasmonic effect for some reason disappears at higher temperatures. **In Figure 4.13b,** the lifetimes of the two different nanowires at various temperatures are presented. At low temperatures, the lifetime on silicon is more than 2 times larger compared to gold, while the two lifetimes merge at temperatures above 210K. To connect these different measurements and prove that there is indeed some type of interaction between the surface plasmons and the emitter, further analysis is needed.

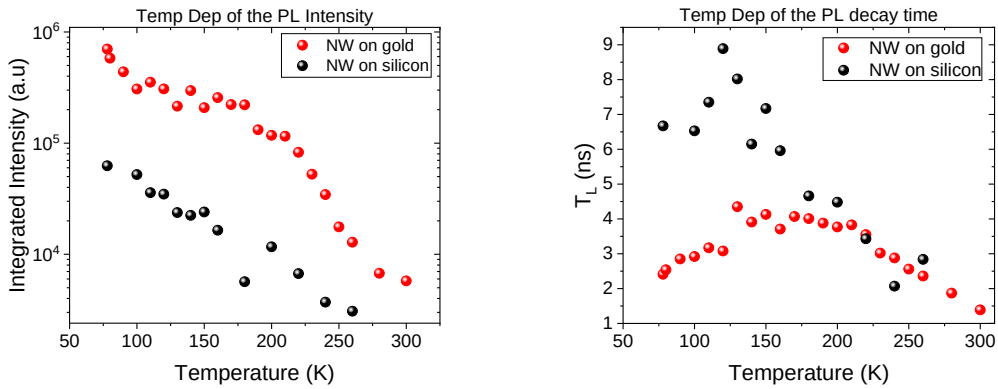


*Figure 4.13 a) Scatter plot of integrated Intensities at different temperatures for a single NW on gold (red) and another single NW on silicon (black) b) Scatter plot of lifetime measurements for different temperatures*

The recorded exciton decay times of **Figure 4.13b** will be analyzed into the radiative and non-radiative components according to M.Gurioli *et al.* [38]. The measured time decays $T_L$ at different temperatures $T$ are related to radiative and non-radiative recombination times $T_R$ and $T_{NR}$ respectively according to the following equation:

$$\frac{1}{T_L(T)} = \frac{1}{T_R(T)} + \frac{1}{T_{NR}(T)} \qquad 4\text{-}1$$

The Integrated intensity $I_L(T)$ at different temperatures can be expressed by:

$$I_L(T) = I_0 \frac{T_L(T)}{T_R(T)} = I_0\, \eta(T) \qquad 4\text{-}2$$

Where $\eta(T)$ is the radiative efficiency and $I_0$ is the normalization factor that depends on the excitation rate and the collection efficiency of the experimental setup.

Combining equations 4-1 and 4-2, the extracted radiative and non-radiative recombination times as a function of $T$ are the following:

$$T_R(T) = I_0 \frac{T_L(T)}{I_L(T)} = \frac{T_L(T)}{\eta(T)} \qquad 4\text{-}3$$

$$T_{NR}(T) = T_L(T)\,\frac{I_0}{I_0 - I_L(T)} = T_L(T)\frac{1}{1-\eta(T)} \qquad 4\text{-}4$$

In **Figure 4.14a,b** and **Figure 4.14c,d** are depicted the extracted values for radiative $T_R$ and non-radiative $T_{NR}$ lifetimes as a function of $T$ under different assumptions for the radiative efficiency $n_0$ at T=78K, ranging from 0.1 to 1. In **Figure 4.14a,b** we see that the $T_R(T)$ curves differ between them by the scale factor of $n_0$, forming in the semilogarithmic graph a set of vertically shifted curves. The general tendency of $T_R(T)$ for both NWs is a significant increase with temperature, from somewhere in the 10ns-range at 78K, all the way up to the 50ns-range at about 200K. On the other hand, the $T_{NR}(T)$ curves in **Figure 4.14c,d** are very dispersed around 78K as they are very sensitive to the precise $n_0$ value (e.g. diverging for $n_0 = 1$). At higher temperatures however, the $T_{NR}(T)$ curves for both types of NWs converge at about 200K, to values of about 5ns. This implies that while at 78K the radiative lifetimes are comparable or even shorter than the non-radiative ones, the situation changes drastically at higher temperature, where for instance at ~200K the non-radiative lifetimes are much shorter than the radiative ones and the NW emission is practically dominated by non-radiative processes.

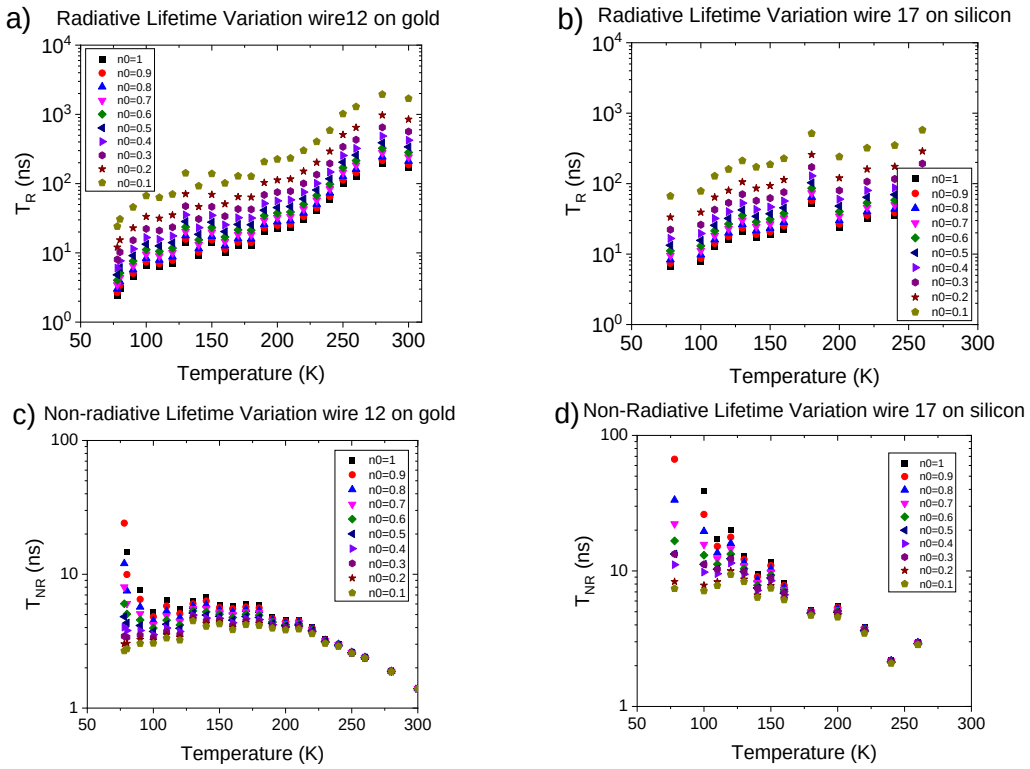


*Figure 4.14* ***Radiative*** *Lifetime Variation for a single nanowire a) on gold and b) on silicon.* ***Non-radiative*** *lifetime for the single NW c) on gold and d) and silicon*

Revisiting now **Figure 4.13** having the above information, we can make the following comments: First, that the NW emission at low T's has a very strong radiative component and that's why the plasmonic effect is most visible at low-T's. Another clear sign that at low T's the NW emission is predominately radiative is that the $T_L$ curve for the NW on gold in **Figure 4.13b** increases with temperature, something never observed in non-radiative processes. Second, that the factor of 4 enhancement at about 200K for the NWs on gold has nothing to do with plasmonic effect but is rather due to the mirror effect of the gold-surface. On the other hand, the factor of ~10 at 78K contains, aside from the mirror effect, a significant enhancement of about ~2 – 2,5 which is most likely due to the plasmonic effect.

## 4.5 Conclusions

In this chapter the plasmon-emitter interaction between a core-shell nanowire and a gold surface is studied as a function of relative distance. We show that by transferring free-standing nanowires on relatively flat gold surface the overall photoluminescence efficiency and recombination dynamics of the nanowires is drastically changed. This leads to an increase in intensity emission in the range of ~12-37 and decrease in the average lifetime of the carriers to almost half for the NWs that were placed on the surface of the gold compared to the NW on silicon, proving that plasmons can be utilized to manipulate the emitter properties with possible applications to single photon emitters.

# References


1. Purcell, E. M., Torrey, H. C. & Pound, R. V. Resonance absorption by nuclear magnetic moments in a solid [7]. *Physical Review* **69**, 37–38 (1946).
2. Pile, D. F. P. *et al.* Theoretical and experimental investigation of strongly localized plasmons on triangular metal wedges for subwavelength waveguiding. *Appl Phys Lett* **87**, 61106 (2005).
3. Barnes, W. L., Dereux, A. & Ebbesen, T. W. Surface plasmon subwavelength optics. *Nature 2003 424:6950* **424**, 824–830 (2003).
4. Oulton, R. F. *et al.* Plasmon lasers at deep subwavelength scale. *Nature 2009 461:7264* **461**, 629–632 (2009).
5. Shimizu, K. T., Woo, W. K., Fisher, B. R., Eisler, H. J. & Bawendi, M. G. Surface-Enhanced Emission from Single Semiconductor Nanocrystals. *Phys Rev Lett* **89**, 117401 (2002).
6. Kwon, M. K. *et al.* Surface-Plasmon-Enhanced Light-Emitting Diodes. *Advanced Materials* **20**, 1253–1257 (2008).
7. Okamoto, K. *et al.* Surface-plasmon-enhanced light emitters based on InGaN quantum wells. *Nature Materials 2004 3:9* **3**, 601–605 (2004).
8. Cho, C. H. *et al.* Tailoring hot-exciton emission and lifetimes in semiconducting nanowires via whispering-gallery nanocavity plasmons. *Nature Materials 2011 10:9* **10**, 669–675 (2011).
9. Zhang, X. *et al.* Surface exciton-plasmon polariton enhanced light emission via integration of single semiconductor nanowires with metal nanostructures. *Nano Res* **2**, 47–53 (2009).
10. Jung, D. R. *et al.* Surface-plasmon-enhanced photoluminescence of CdS nanoparticles with Au/SiO2 nanocomposites. *Mater Res Bull* **47**, 453–457 (2012).
11. Jung, D. R. *et al.* Photoluminescence enhancement in CdS nanoparticles by surface-plasmon resonance. *Appl Phys Lett* **99**, 41906 (2011).
12. Lin, H. Y., Chen, Y. F., Wu, J. G., Wang, D. I. & Chen, C. C. Carrier transfer induced photoluminescence change in metal-semiconductor core-shell nanostructures. *Appl Phys Lett* **88**, 161911 (2006).
13. Xiao, X. H. *et al.* Surface plasmon-enhanced light emission using silver nanoparticles embedded in ZnO. *Appl Phys Lett* **97**, 71909 (2010).

14. Pan, S., Wang, Z. & Rothberg, L. J. Enhancement of adsorbed dye monolayer fluorescence by a silver nanoparticle overlayer. *Journal of Physical Chemistry B* **110**, 17383–17387 (2006).

15. Im, J., Singh, J., Soares, J. W., Steeves, D. M. & Whitten, J. E. Synthesis and optical properties of dithiol-linked ZnO/gold nanoparticle composites. *Journal of Physical Chemistry C* **115**, 10518–10523 (2011).

16. Kulakovich, O. *et al.* Enhanced Luminescence of CdSe Quantum Dots on Gold Colloids. *Nano Lett* **2**, 1449–1452 (2002).

17. Li, X. *et al.* Enhancing fluorescence of quantum dots by silica-coated gold nanorods under one- and two-photon excitation. *Optics Express, Vol. 18, Issue 11, pp. 11335-11346* **18**, 11335–11346 (2010).

18. Chen, T., Xing, G. Z., Zhang, Z., Chen, H. Y. & Wu, T. Tailoring the photoluminescence of ZnO nanowires using Au nanoparticles. *Nanotechnology* **19**, 435711 (2008).

19. Li, M. *et al.* Synthesis of Au–CdS Core–Shell Hetero-Nanorods with Efficient Exciton–Plasmon Interactions. *Adv Funct Mater* **21**, 1788–1794 (2011).

20. Li, G. P. *et al.* Nanoscale semiconductor–insulator–metal core/shell heterostructures: facile synthesis and light emission. *Nanoscale* **3**, 3170–3177 (2011).

21. Cheng, C. W. *et al.* Surface plasmon enhanced band edge luminescence of ZnO nanorods by capping Au nanoparticles. *Appl Phys Lett* **96**, 71107 (2010).

22. Lee, J., Govorov, A. O., Dulka, J. & Kotov, N. A. Bioconjugates of CdTe nanowires and Au nanoparticles: Plasmon-exciton interactions, luminescence enhancement, and collective effects. *Nano Lett* **4**, 2323–2330 (2004).

23. Guo, P. *et al.* Surface plasmon resonance enhanced band-edge emission of CdS–SiO2 core–shell nanowires with gold nanoparticles attached. *J Mater Chem C Mater* **1**, 566–571 (2012).

24. Mokkapati, S. *et al.* An order of magnitude increase in the quantum efficiency of (Al)GaAs nanowires using hybrid photonic-plasmonic modes. *Nano Lett* **15**, 307–312 (2015).

25. Chen, T., Xing, G. Z., Zhang, Z., Chen, H. Y. & Wu, T. Tailoring the photoluminescence of ZnO nanowires using Au nanoparticles. *Nanotechnology* **19**, 435711 (2008).

26. Kaveh, M. *et al.* Controlling the exciton emission of gold coated GaAs–AlGaAs core–shell nanowires with an organic spacer layer. *Nanotechnology* **27**, 485204 (2016).

27. Duan, X., Huang, Y., Agarwal, R. & Lieber, C. M. Single-nanowire electrically driven lasers. *Nature 2003 421:6920* **421**, 241–245 (2003).

28. Duan, X., Huang, Y., Cui, Y., Wang, J. & Lieber, C. M. Indium phosphide nanowires as building blocks for nanoscale electronic and optoelectronic devices. *Nature 2001 409:6816* **409**, 66–69 (2001).

29. Friedman, R. S., McAlpine, M. C., Ricketts, D. S., Ham, D. & Lieber, C. M. High-speed integrated nanowire circuits. *Nature 2005 434:7037* **434**, 1085–1085 (2005).

30. Yan, H. *et al.* Programmable nanowire circuits for nanoprocessors. *Nature 2011 470:7333* **470**, 240–244 (2011).

31. Qian, F. *et al.* Multi-quantum-well nanowire heterostructures for wavelength-controlled lasers. *Nature Materials 2008 7:9* **7**, 701–706 (2008).

32. Huang, M. H. *et al.* Room-temperature ultraviolet nanowire nanolasers. *Science (1979)* **292**, 1897–1899 (2001).

33. Huang, Y. *et al.* Logic gates and computation from assembled nanowire building blocks. *Science (1979)* **294**, 1313–1317 (2001).

34. Zhong, Z., Wang, D., Cui, Y., Bockrath, M. W. & Lieber, C. H. Nanowire Crossbar Arrays as Address Decoders for Integrated Nanosystems. *Science (1979)* **302**, 1377–1379 (2003).

35. Balaghi, L. *et al.* Widely tunable GaAs bandgap via strain engineering in core/shell nanowires with large lattice mismatch. *Nat Commun* **10**, 2793 (2019).

36. Shan, C. X., Liu, Z. & Hark, S. K. Photoluminescence polarization in individual CdSe nanowires. *Phys Rev B* **74**, 153402 (2006).

37. Jana, J., Ganguly, M. & Pal, T. Enlightening surface plasmon resonance effect of metal nanoparticles for practical spectroscopic application. *RSC Adv* **6**, 86174–86211 (2016).

38. Gurioli, M. *et al.* Temperature dependence of the radiative and nonradiative recombination time in GaAs/AlxGa1−xAs quantum-well structures. *Phys Rev B* **44**, 3115 (1991).

39. Otto, A., Mrozek, I., Grabhorn, H. & Akemann, W. Surface-enhanced Raman scattering. *Journal of Physics: Condensed Matter* **4**, 1143 (1992).

40. Moskovits, M. Surface-enhanced spectroscopy. *Rev Mod Phys* **57**, 783 (1985).

41. Gersten, J. & Nitzan, A. Electromagnetic theory of enhanced Raman scattering by molecules adsorbed on rough surfaces. *J Chem Phys* **73**, 3023–3037 (1980).

42. Glass, A. M., Liao, P. F., Bergman, J. G. & Olson, D. H. Interaction of metal particles with adsorbed dye molecules: absorption and luminescence. *Optics Letters, Vol. 5, Issue 9, pp. 368-370* **5**, 368–370 (1980).

43. Shimizu, K. T., Woo, W. K., Fisher, B. R., Eisler, H. J. & Bawendi, M. G. Surface-Enhanced Emission from Single Semiconductor Nanocrystals. *Phys Rev Lett* **89**, 117401 (2002).

# 5 Perspectives

The rapid deployment of Quantum Technologies in the near future depends crucially on the availability of efficient, controllable and cost-effective nanophotonic sources of single and entangled photons. In this chapter a new generation of solution-processed $CsPbBr_3$ halide perovskite nanocrystals are studied as nanophotonic devices of the future. Open questions such as the origin of the photo-blinking mechanism and the absence of multiexcitonic lines such as biexcitons (XX) about $CsPbBr_3$ nanocrystals make necessary the further-study of their optoelectronic properties. For this reason, we studied via the quantum-confined Stark effect (QCSE) of the optical transitions of $CsPbBr_3$ NCs. Despite the large values of hundreds of KVs/cm applied on single NCs we observed no significant change on the excitonic transition energy or lifetime, possibly due to severe screening effects of the excitons inside the nanocrystal. In addition, we have experimented with alternative collection strategy schemes in order to increase the light collection efficiency of our optical setup. By reducing the refractive index difference between the material, where the emitter is embedded, and its environment it is possible to obtain a collection enhancement larger than two, which is crucial for high temperature applications.

## 5.1 Perovskite NCs as single photon emitters

Lead halide perovskite NCs, such as for instance CsPbBr3 NCs, have shown great potential as single photon sources “on-demand”, exhibiting remarkable photon antibunching behavior at room temperature, with $g^2(0)$ values as low as a few percent[1]. Interestingly, however, the single-photon purity of the NC emission deteriorates at low temperatures and the corresponding $g^2(0)$ values fall between 0.3[2] and 0.7 in our own measurements at 78K. This is contrary to what is typically observed in other semiconductor QD systems, where the $g^2(0)$ values increase with increasing temperature. Another particularity of these NCs is that, with the exception of a report on $CsPbI_3$ nanocrystals[3], no distinct biexciton lines are observed in single dot spectroscopy experiments. This possibly suggests that in most perovskite NCs, the bi-exciton and exciton lines are very close in energy, explaining the poor single photon purity at low temperatures. With increasing temperature, the hypothesis goes that some thermally-activated Auger process[4] takes place, where biexciton energy is non-

radiatively transferred to an extra charge instead of being converted to a photon, weakening the bi-excitonic emission and lowering drastically the $g^2(0)$ values at 300K. In order to clarify these hypotheses and deepen our understanding of the exciton transitions in these NCs [3,5–8], we have studied in this thesis for the first time, the emission properties of single $CsPbBr_3$ nanocrystals under the effect of an external electric field.

## 5.2 Can perovskite NCs replace traditional QDs?

When quantum confined Stark effect occurs in semiconductor nanostructures, the electron and hole wavefunction overlap is modified so they overlap, leading to some major changes in the excitonic recombination energy, oscillator strength and carrier lifetime [9–11]. The effect of QCSE has been previously studied in epitaxially grown QDs to remove their fine structure splitting and produce entangled photons [12–14]. In chemically synthesized NCs, the QCSE is present in asymmetric structures where weak quantum confinement exists, such as nanorods and nano-pellets [15–24]. Recently novel perovskite NCs, such as the ones used in this thesis, have reached the weak confinement regime by having sizes comparable with the exciton Bohr diameter [25]. The effect of QCSE on perovskite NCs has been largely unexplored [26] and only two works on $CsPbI_3$ [27] and $CsPbBr_3$ [28] NCs, have examined the effect of electric field on this weakly quantum-confined nanostructures. The understanding of QCSE will not only provide better evaluation of their optoelectronic properties for various applications but also allow to extend their applicability to the regime of quantum technologies.

## 5.3 Experimental techniques

### 5.3.1 Perovskite NCs diluted in toluene

The perovskite nanocrystals fabrication will be not discussed in detail because this is beyond the scope of this thesis. Fabrication of the perovskite NC solutions are made by our colleagues in ETH Zurich following a specific-solution phase synthesis of monodisperse $CsPbX_3$ NCs[29], which takes advantage of the ionic nature of the chemical bonding in these compounds. Furthermore, the NCs were treated post-synthetically with didodecyldmethylammonium bromide (DDAB) molecules to increase their stability and quantum yield [30]. All the nanocrystals with chemical composition of

$CsPbBr_3$ are diluted in toluene inside a glass vial with average concentration of ~10mg/ml.

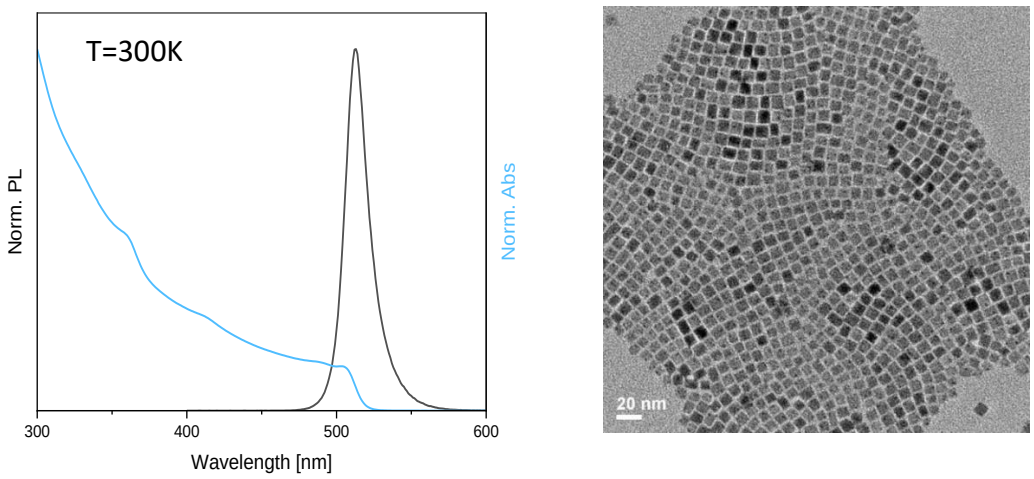


*Figure 5.1: a) Absorption and photoluminescence spectra of DDAB treated NCs diluted in toluene, b) TEM image of single NCs placed close to each other with average size of ~10nm.*

For the optical characterization of the diluted NCs the vials are illuminated directly from an angle and the light is collected and analyzed with a spectrometer. In **Figure 5.1a** the excitonic absorption profile and the narrowband photoluminescence of ~19nm is shown, centered at 512nm. The NCs have cubic shape with an average size of ~10nm as shown in TEM image in **Figure 5.1b)**. All these NCs feature a high quantum yield as high as ~90% inside a toluene solution[8].

### 5.3.2 Preparing single NCs for μPL spectroscopy

Perovskite NCs are heavily concentrated inside the vial and thus cannot be studied without dilution. To perform single NC spectroscopy the initial solution has to be specifically diluted [8] and spin-coated on the substrate of our choice. The dilution process involves two stages in order to be precisely controlled towards the final desired concentration: 1) First 5μL of the initial solution (10mg/ml) is diluted with 1000μL of toluene leading to x200 dilution and final concentration of 0.05mg/ml. 2) Next 5μL of the x200 diluted solution is added to 1000μL of pure toluene leading to x40000 dilution compared to the initial solution with a final concentration of 0.00025mg/mL.

To spread the crystals on top of a substrate, spin coating technique is used. The optimal speed to prepare samples was found to be at 3000rpm after various tests resulting to various NC densities on the surface. The other critical parameter was the usage of polymer matrix to prevent degradation. The polymer used here was

polystyrene and to prepare the samples, the first step of dilution remains the same. The second step involves dilution with a mixture of a 5wt% polymer solution in toluene (200µL) and pure toluene (800µL) leading to the same 0.00025mg/mL concentration. Many samples were prepared in order to decide whether polystyrene is needed or not. We found that polystyrene not only protects the NCs from degradation but also helps for the best NC surface dispersion.

### 5.3.3 Imaging of the single NCs

To perform single NC spectroscopy, the samples are loaded in the µPL setup described in chapter 2. Since the single NCs are very small, they cannot be observed with our x40 microscope objective and hence cannot be probed directly. The solution to this is either to scan the surface of the sample and monitor in single NC spectroscopy when a spectrum appears on the screen, or use a different illumination source that not only illuminates the surface but also excites the single NCs enough so we can detect their luminescence from a simple camera with adjustable exposure. The first approach requires too much human time to characterize one sample, which makes it impractical. The second approach requires less time and also gives a precise image of the NCs topological locations, making it possible to relocate a single NC of interest. Also imaging a large area of NCs gives information about their dispersion.

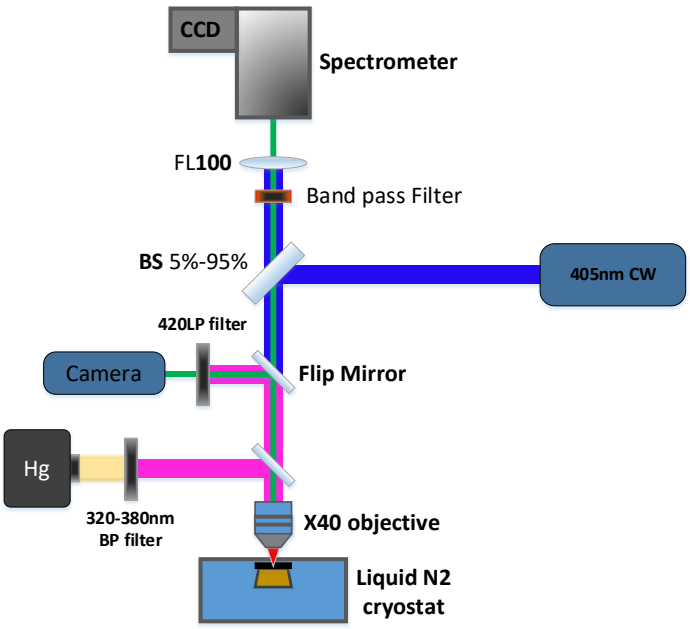


*Figure 5.2: Schematic illustration of the µPL setup using an high power Hg lamp to image the single NCs via their photoluminescence.*

To image the single NCs the μPL setup was modified as **Figure 5.2** shows. The microscope's regular white halogen lamp was replaced with an Osram 100W Hg. This high-power lamp can produce relatively high UV emission, enough to excite the perovskite NCs. The spectrum of the lamp is filtered with a band pass BP330-385nm filter. In the collection path there is a long pass filter at 420nm that allows only the emission of the perovskites to reach the camera through a beam splitter. Because of this, we can also include our excitation source into the imaging path which enables us to precisely see where our laser spot is located at the surface of the sample while we image the real PL signal of the NCs.

### 5.3.4 Protecting the NCs from degradation

Despite their great potential, single NCs have insufficient optical stability in ambient conditions mainly because of the moisture-assisted photodegradation [8]. In this section the polystyrene effect on perovskite NC emission is discussed. The perovskite NCs come diluted in toluene with a density of ~10mg/ml. As discussed before, dilution is necessary in order to perform single NC spectroscopy. Two different samples were prepared, with and without polystyrene, for single NC spectroscopy. In **Figure 5.3** the μPL of the samples is shown and each of them was measured two consecutive days.

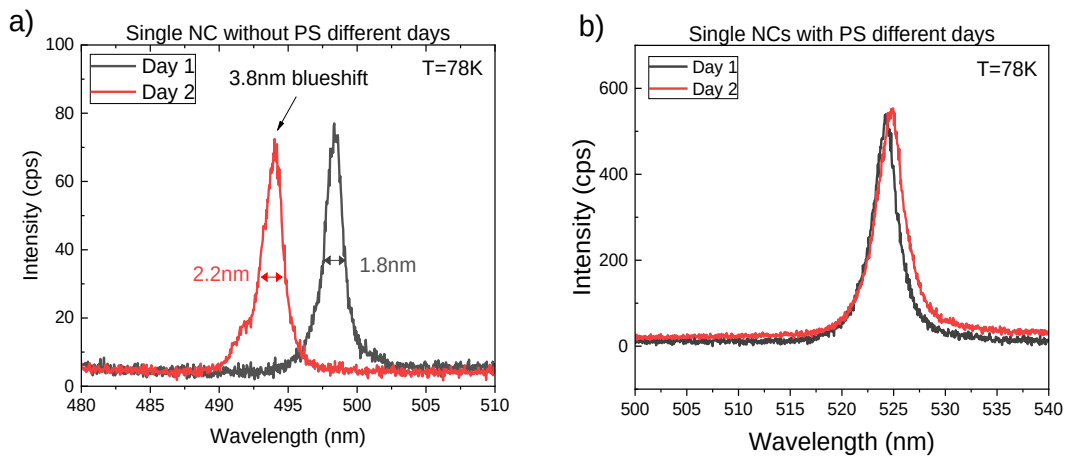


*Figure 5.3: μPL spectra of a single $CsPbCr_3$ NC two consecutive days a) without use of polystyrene b) with use of polystyrene*

In **Figure 5.3a** there is the μPL spectrum of a single NC without the protection of PS. The red line shows the spectrum of the same NC after one day inside the cryostat in the presence of vacuum. It has been reported previously a possible degradation of

the $CsPbBr_3$ NCs during the acquisition of the data, which is also accompanied by a permanent blue shift[31,32]. This mechanism involves the presence of humidity and light simultaneously during the measurements which is not our case for where the NCs are left in vacuum overnight. Interestingly, when there is no polymer matrix to protecting the NCs we observe a significant blueshift of the main emission accompanied with some spectral broadening. This cannot be attributed directly to humidity because there is vacuum inside the cryostat. Even though, our cryostat cannot maintain the same level of vacuum overnight, we think unlikely that any humidity appears inside the chamber. A possible degradation alternative is the silver paint we used to glue the substrate on the cold finger. Such pastes are diluted in polar solvents such as acetone, which can strongly modify and even degrade the perovskite NCs[33], as the dilutant can be evaporated overnight causing degradation to the NCs. On the other hand, the single NC in **Figure 5.3b** maintains the spectral position of its emission line after one day. The small shift can be attributed to the spectral diffusion during the measurement.

### 5.3.5 Controlling the density of perovskite NCs

The usage of Polystyrene to protect the single NCs from degradation non only protects the NCs from degradation but also helps their dispersion on the surface of the sample. The toluene itself is hydrophobic and during the spin-coating, the solution does not uniformly spread all over the surface of the Si substrate. To enhance spreading, we treated the surface of the sample with oxygen plasma to activate the surface bonds, making the toluene to spread evenly and evaporate leaving behind single NCs. As shown in **Figure 5.4a** the NCs most of the time form clusters of many single NCs (big white spots) preventing us from performing single NC spectroscopy. On the other hand, by using PS the NCs also form clusters but in the area between these clusters, many of these can be found isolated and more importantly equally distributed over the surface of the sample. This result makes single NC spectroscopy much easier to perform.

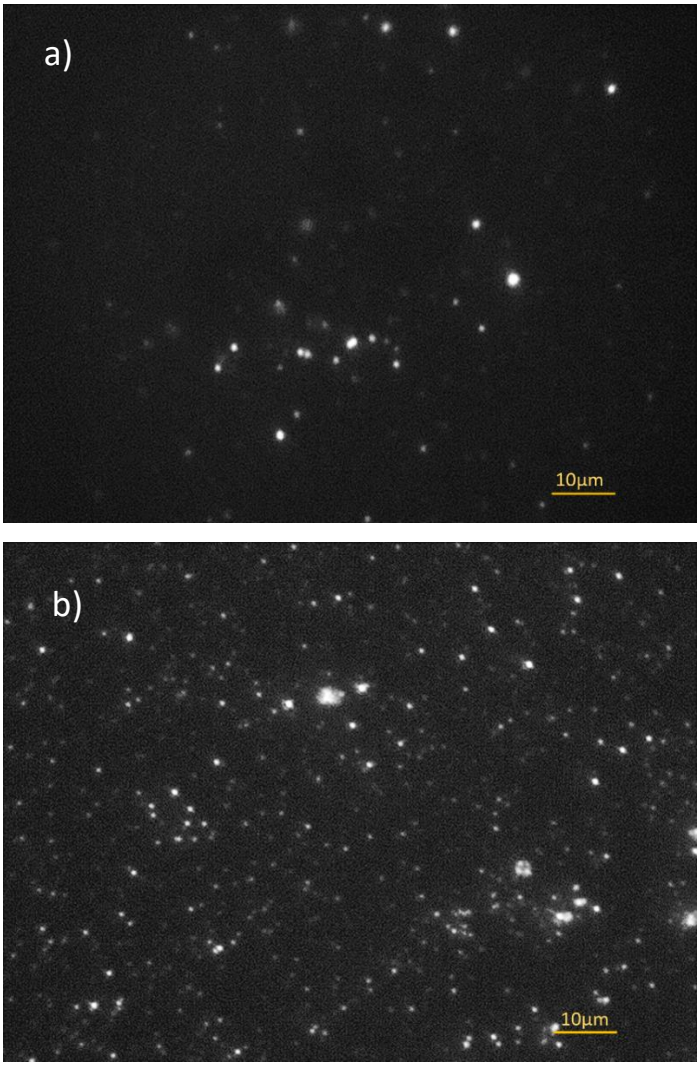


*Figure 5.4: Optical image of a sample spin coated a) without, and b) with polystyrene, showing the Photoluminescence of the perovskites in grey scale.*

The average NC density of the NCs using the dilution recipe described in the previous section and polystyrene for protection is ~2nc/10µm$^2$ as shown in **Figure 5.4b**.

### 5.3.6 Optical characterization

A large number of different NCs with and without polystyrene were studied at 78K with µPL. In **Figure 5.6**, the FWHM linewidth versus emission wavelength of each NC is plotted in a scatter form. At that point, there was no way to distinguish emissions from single NCs, other than based on their emission wavelength and FWHM linewidth.

In **Figure 5.5,** a calculated prediction of the FWHM for a single NC is plotted versus temperature using the Ramade *et al.*[34] formula for homogeneous linewidth of excitons:

$$\gamma(T) = \gamma_0 + A_{ac}T + B_{LO} + n_{LO}(T) \qquad 5\text{-}1$$

Where $\gamma_0$ is a residual homogeneous linewidth including spectral diffusion, $A_{ac}$ and $B_{LO}$ are homogeneous broadening terms for acoustic and LO phonons, and $n_{LO}(T) = 1/(\exp\left(\frac{E_{LO}}{k_b T}\right) - 1)$ is the Bose Einstein distribution function for the LO phonons. $E_{LO}$ is an average energy for the weakly dispersive LO phonon branch. We used the same parameters as Ramade *et al.* and plotted three different lines for $B_{LO}$ = 40, 50 and 60 meV. At 78K, the predicted FWHM value for a single NC is ~5-7 meV, which can be translated to a $\Delta\lambda$ of ~ 2 nm. Therefore, every NC that has FWHM linewidth ≤ 2nm can be considered to be a single NC.

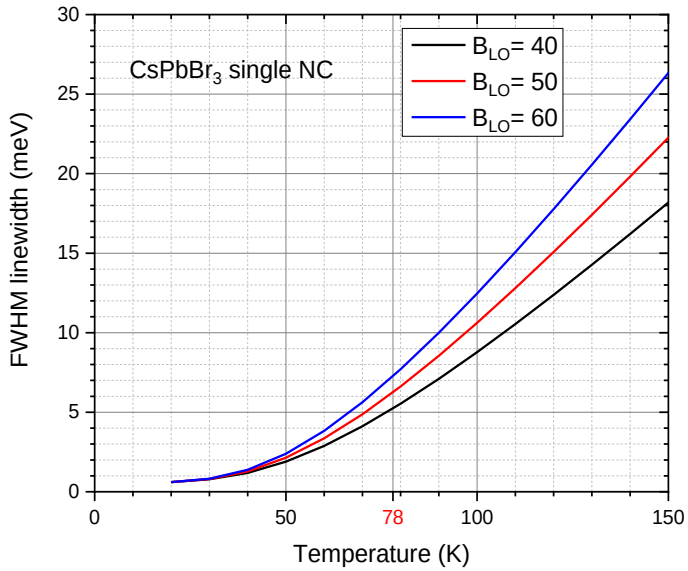


*Figure 5.5: Plot of FWHM linewidth for a single $CsPbBr_3$ NC at different temperatures assuming three different charge phonon $B_{LO}$ constants.*

In **Figure 5.6** the blue dots represent NCs without polystyrene and their spectral emission extends from 510nm to 540nm with average linewidths of ~5nm. On the other hand, the orange dots represent NCs inside polystyrene and their emission wavelength

ranges from 495nm to 520nm with average linewidths of 2nm. Based on the previously mentioned "selection rule" one can be tempted to say that NCs inside PS can be considered "mostly" single NCs, despite the fact that their spectral position is not at ~530nm at T=78K, as it should be, indicating some possible modification of their actual size. On the other hand, the NCs without polystyrene cannot be separated and form mostly clusters of single NCs, which in most cases form aggregates that are more difficult to undergo degradation so their emission stays centered about ~530nm.

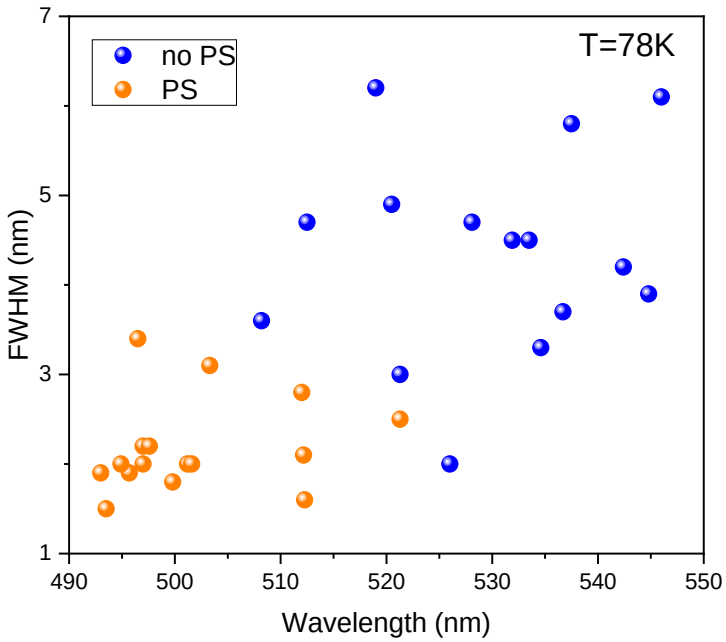


*Figure 5.6: Scatter plot of emission FWHM versus the position of the central peak for different single NCs spined **with** (orange) and **without** (blue) polystyrene*

### 5.3.7 Device fabrication

To apply electric field, a specially patterned substrate had to be designed and fabricated. The ideal design for electric field application is an interdigitated pattern very similar to that typically used for RF and sensing applications. The typical pattern used is shown **Figure 5.7a**. The ''writing'' of the mask and the lithography process was made using e-beam lithography. The substrate is divided in periods with interdigitated structures and distinguishing numbers on top, while the distance between electrodes is ~1.5μm as shown in **Figure 5.7b**. This enables to generate large values of electric field by applying relatively small voltages between the electrodes.

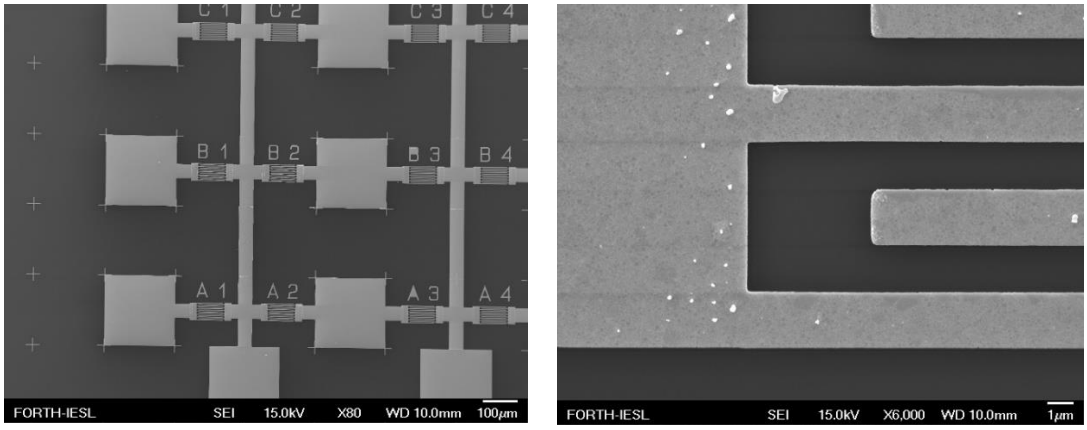


*Figure 5.7: a) SEM image of the metal fingers with numbering notation over them. B) Larger magnification SEM image showing metal finger distance of ~1.5μm.*

The NC solution was spin coated all over the patterned substrate using polystyrene for passivation and NC dispersion and only the NCs that were randomly positioned between the metal "fingers" were studied. To apply electric field special packages were used. The square metal pads of the sample were bonded with the package as **Figure 5.8a** shows, allowing the application of voltage difference in different areas of the sample. To mount the whole device inside the cryostat the package is attached on the cold finger using a specially designed base (**Figure 5.8b**) with electrical leads, having the ability to reload packages without any soldering and being fully compatible with cryogenics. The electric field is applied to the devices using vacuum-compatible and electrically-insulated copper wires.

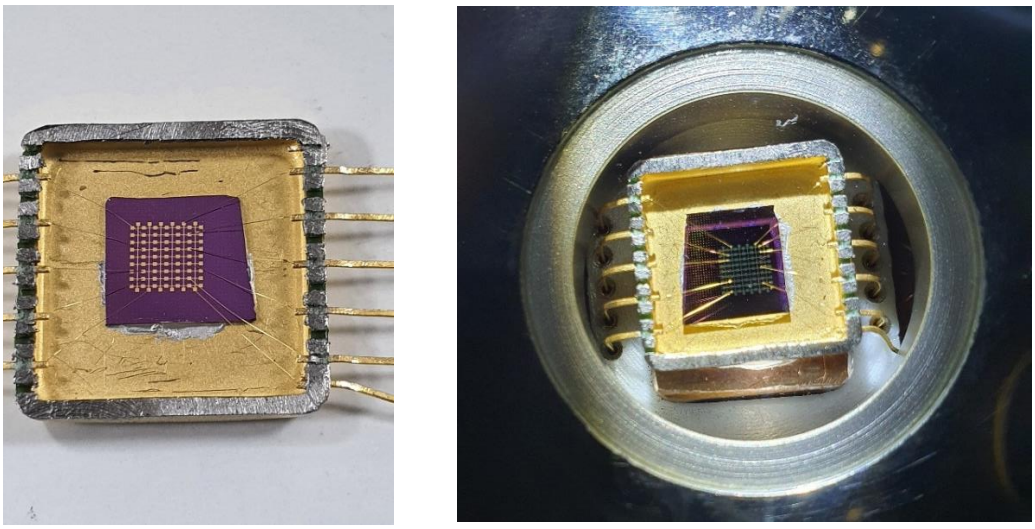

*Figure 5.8: a) Image of a spin coated substrate being bonded with the contacts of the package. b) Image of the package mounted on the cold finger having its contacts impeded in a special designed base (white) inside the cryostat.*

### 5.3.8 Photoluminescence under constant electric field

In **Figure 5.9a** the μPL spectra for a single NC embedded in polystyrene at different applied voltages is shown. The maximum bias volage range was from -40V to +40V resulting to an applied electric field of ± 100KV/cm on each NC taking into account the dielectric constant of the polystyrene which is ~ 2.6[35]. The black perpendicular line in the same figure represents the center of the peak at 0V acting as a reference. It is clear from the different spectra that there is no significant Stark-shift in the emission energy of the single NC. In this particular NC, we observe only a minor redshift of the emission line for positive and negative values of electric field. These small shifts in each case are depicted in **Figure 5.9b** where the maximum energy shift is less than 1meV.

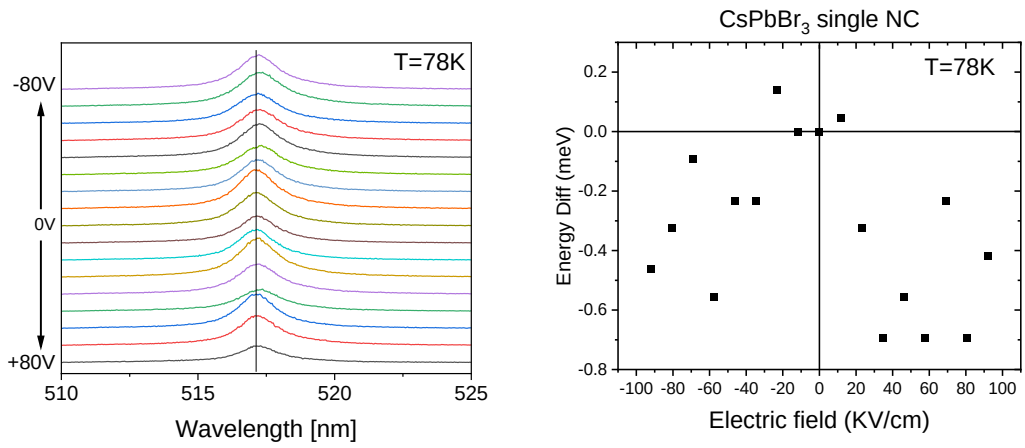


*Figure 5.9: a) Plotted μPL spectra of a single NCs at different applied voltages, b) Scatter plot for the energy shift for the single NC at different applied electric fields*

The same picture is observed also in a larger number of studied NCs. In **Figure 5.10** the energy shift versus applied electric field is plotted in a scatter form for different single NCs. Each color in the scatter plot represents a different single NC. The "direction" of the energy shifting behavior of the single NCs cannot be predicted as there are NCs that redshift while others blueshift regardless the positive or negative sign of the bias. Also, despite the large number of studied NCs none showed energy shift greater than 1meV. This value is comparable to the statistical noise due to the spectral diffusion of the lines and suggests a strongly suppressed Stark effect in our system. Finally, we note the photodegradation of the single NC after a long period of

light exposure time which makes impossible to perform repetitive biased measurements for multiple times on a single NC.

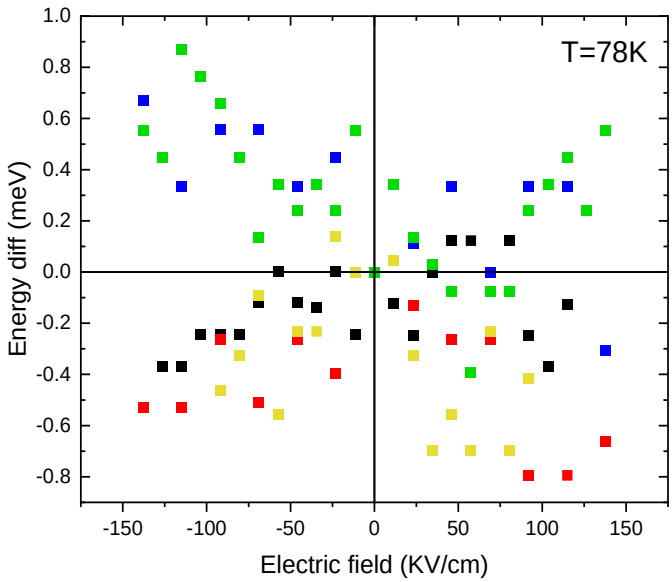


*Figure 5.10: Scatter plot of different studied NCs showing variable energy shifts at bias voltage ranging from -150 to 150 kV/cm electric field*

Finally, the question which rises is why there is no significant QCSE observed in our $CsPbBr_3$ single NCs. We have already applied hundreds of KV/cm, which is more than enough to observe Stark shifts for classic semiconductor NC systems [11]. One possible explanation is that there are dipoles around the NC (such as the protective ligands) that are able to screen the applied electric field almost instantaneously. If this hypothesis is valid, the next question is how fast this screening mechanism is, and whether it is possible to prevent it. An ideal experiment would be to apply a pulsed electric field in the form of ultra-fast pulses with very fast rise time. The biggest challenge at the moment is the realization of a pulse generator with these fast characteristics, assuming that the screening mechanism has a response time shorter than nanosecond.

### 5.3.9 Time resolved Photoluminescence under electric field

To explore further the effect of electric field on the emission of the single $CsPbBr_3$ NCs and examine whether transient effects are observable, we performed TRPL measurements on a single NC under external electric field. For TRPL

measurements, the same setup described in Chapter 3 was used with different excitation source. Here a 400nm femtosecond pulsed laser, originating from a nonlinear crystal (doubler) was used with 80MHZ repetition rate. In **Figure 5.11a** different spectra under pulsed excitation from a single NC under electric field are shown. The energy shift of the emission lines follows the same behavior as with the CW excitation described in previous section, showing energy shifts less than 1meV (**Figure 5.11b**).

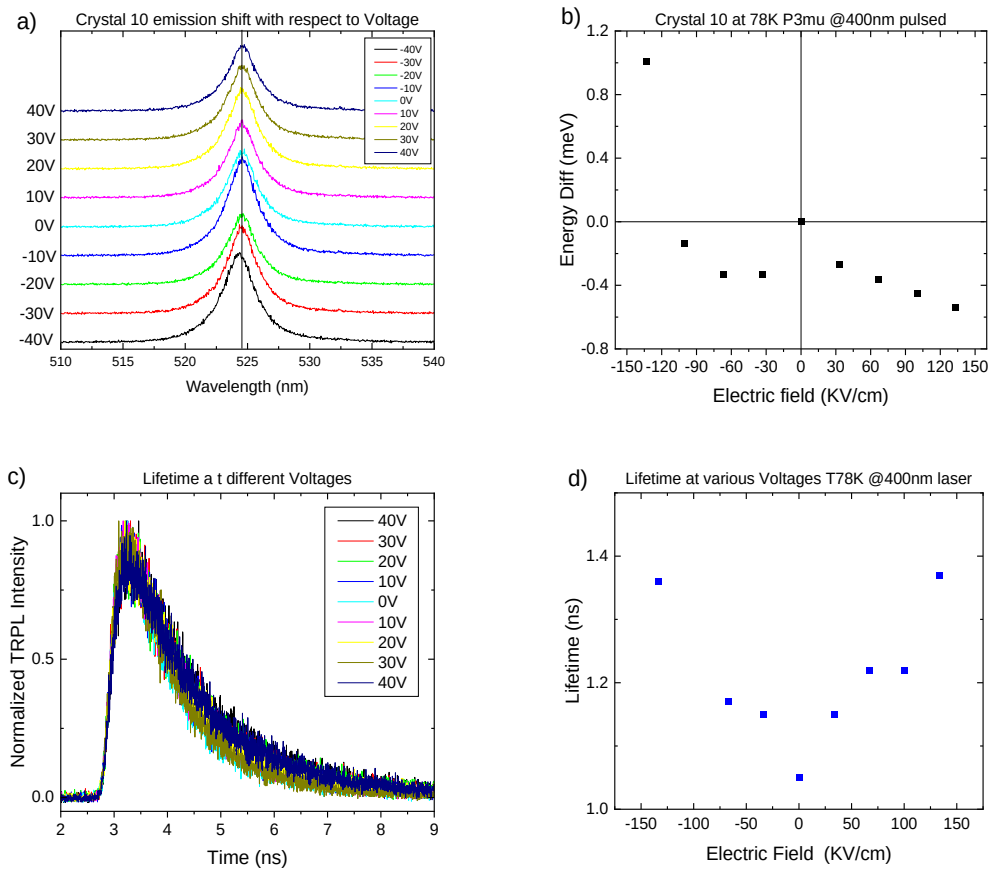


*Figure 5.11: a) μPL spectra under pulsed excitation of single $CsPbBr_3$ NC at different applied voltages, b) Energy shift at different applied electric field, c) Lifetime measurements at different applied voltages d) Lifetime measurements at different applied electric fields*

The lifetime measurements at different applied voltages in **Figure 5.11c** show small changes in the recombination times of the carriers inside the crystal. This is shown in **Figure 5.11d** where all the measured lifetimes are plotted versus the applied electric field. For non-zero electric field the carrier lifetime is increased suggesting that even if the Stark effect is not shown as emission shift in the μPL spectra, the electric field has an effect on single $CsPbBr_3$ NCs. However, this effect was not observed systematically, as in other NCs shorter lifetimes were observed with increasing electric field. In

addition, our experiments could not lead to some safe conclusions as we were bothered by photodegradation phenomena making it impossible to repeat the same experiment on the same NC twice.

## 5.4 Light Collection Strategies

Photons which are produced by single photon sources like semiconductor QDs have in general very low extraction efficiency. When a QD is embedded in a high index material only a fraction of the emission escapes the surface as $1/2n^2$, where $n$ is the refractive index of the material. For a QD embedded into GaAs for example this amount is ~4% while the rest of the light (above $\theta_c$) is reflected back into the substrate as **Figure 5.12** shows. To enhance the emission of a QD, a microcavity designed to operate at the emitter's wavelength can be used[36]. Also, changing the geometry of the microcavity by using micropillars[37], can effectively increase the collection efficiency of the emitted light. To further increase the collection efficiency, another geometrical approach can be utilized which is the use of immersion lenses[38]. The idea is to reduce the refractive index difference of the emitter and its immediate surroundings. To achieve that, immersion lenses can be used made either from oil or solid materials. Suitable oil immersion lenses have relatively low refractive indices in the range of 1.3-1.75 while their solid counterparts can reach values up to 3.5. Using high refractive index material translates via Snell's law into larger collection angle. This means that the photons in large angles are not totally reflected back to the substrate but can escape and be collected from the collective lens (objective).

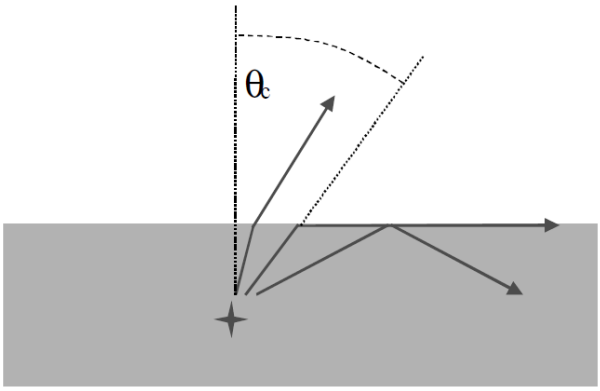


*Figure 5.12: Schematic illustration of the light emission from an emitter embedded in a high index material. For every angle larger than $\Theta_c$ there is a total reflection back to the substrate. Reprinted from W.L.Barnes et al.*[38]

In **Figure 5.13** the collection efficiency for different numerical aperture (NA) of the collection optics is plotted using the equation proposed by W.L.Barnes *et al.*[38]. In **Figure 5.13a**, the calculated efficiency for our microscope objective with 0.6 NA is ~1% for the no-lens geometry (inset). On the other hand, if an immersion lens is used with the characteristics shown the theoretical collection efficiency is ~5% which is 5 times larger.

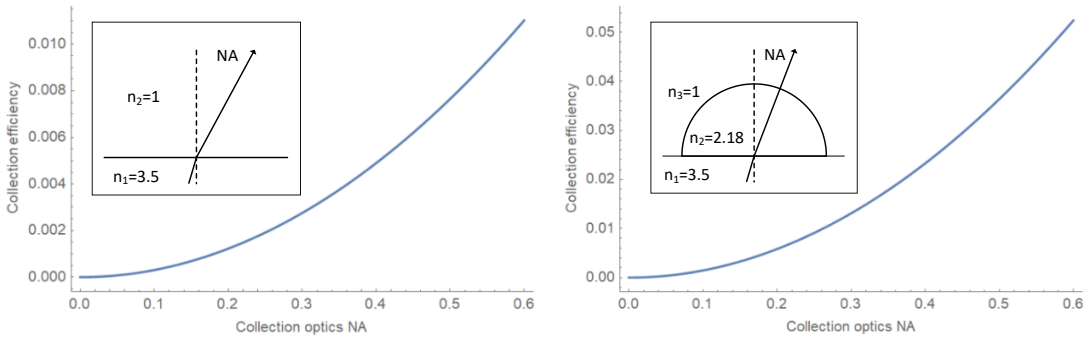


*Figure 5.13: a) Calculated collection efficiency for different collection optics numerical aperture through a planar bulk GaAs dielectric with refractive index $n_1$=3.5. b) Calculated collection efficiency for the same planar GaAs dielectric with $n_1$=3.5 covered by a solid immersion len with $n_2$=2.18. The inset figures represent the two different geometries used for the calculations.*

### 5.4.1 Micro photoluminescence measurements

To estimate how much more light can actually be collected by using solid immersion lenses (SIL), we decided to use half-ball lenses of 500µm diameter made from cubic zirconia ($ZrO_2$) with refractive index of ~2.18. These lenses were used on top of three different samples containing InAs QDs. As excitation source a tunable pulsed Ti:sapphire laser at 740nm was used. The first sample was unprocessed and without microcavity, the second sample was processed with micropillars geometry and no microcavity and the third sample was processed with micropillars geometry and microcavity.

**Half-ball lens on as grown sample without microcavity (MC)**

**Figure 5.14** shows the µPL spectra of different single QDs with and without lens on top of them, for two different excitation powers. The QDs with lens on top of them show enhanced µPL signal compared to the QDs without. Because it is not possible to locate a single QD on the surface of an unprocessed sample, different QDs were randomly selected and their different emissions were taken into consideration to

extract an average emission intensity value. Overall, the μPL was enhanced by a factor of ~5, when using half ball lens.

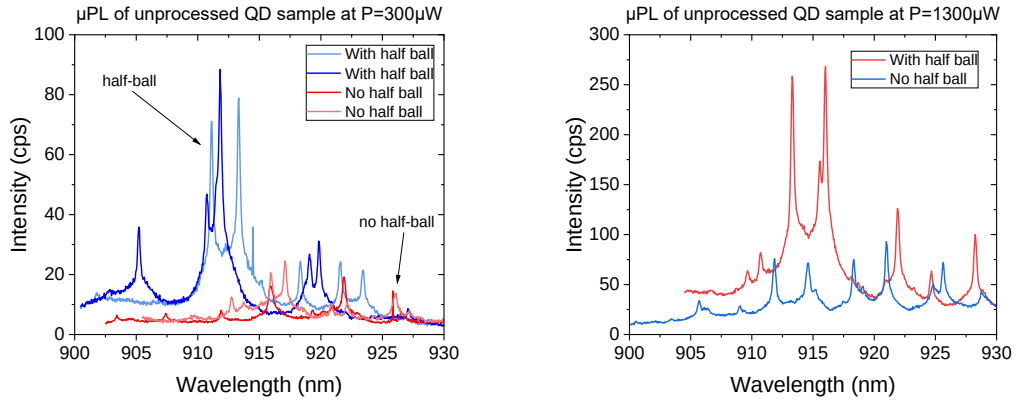


*Figure 5.14: μPL from different single QDs with and without half ball lens on top at a) 300μW and b) 1300μW excitation power.*

**Half-ball lens on processed with micropillars sample without MC**

In the second case where the QDs are inside micropillars it was possible to locate the same single QD and measure it before and after capping it with half ball lens. In **Figure 5.15** the signal of the μPL is enhanced by a factor of ~7. Interestingly, the calculated ratio of the X and XX emission intensity remains the same in each case indicating that the enhanced emission of the single QD does not originate from increased excitation of the dot, following the assumption that the incident beam is focused in a smaller area through the half-ball lens.

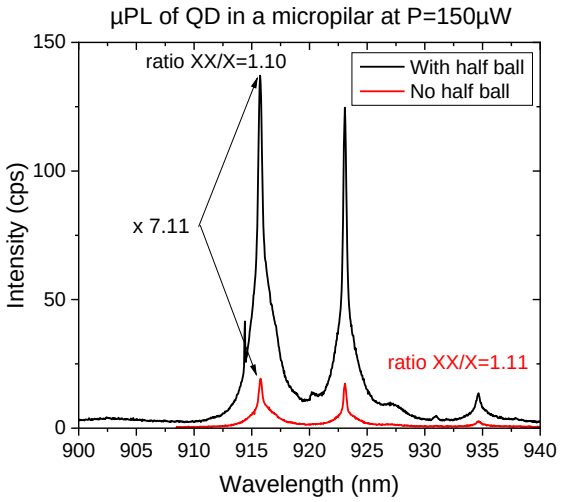


*Figure 5.15 μPL from a single QD showing the X and XX emission with and without half ball lens on top of the processed sample with micropillar geometry. Here the calculated ratio of X/XX in each case indicates that the QD excitation is the same in the two experiments.*

**Half-ball lens on processed with micropillars sample with a MC**

In the third case, a single QD inside a MC was located and measured before and after capping it with half-ball lens. The emission intensity for X and XX was increased by a factor of ~2.3 for the case of lens and their intensity ratio remains the same as in the case of **Figure 5.15**.

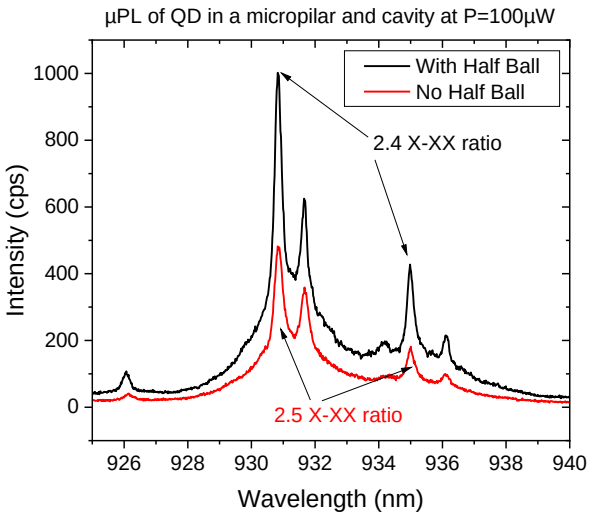


*Figure 5.16: µPL from a single QD showing the X and XX emission with and without half-ball lens on top of the processed sample with micropillar geometry and microcavity. The calculated X/XX ratio indicates no change in the excitation condition of the QD.*

Overall, the emission intensity from single QDs was increased systematically when using immersion lens on top of the sample. In the first case, where the experimental geometry is the same as the theoretical, the enhancement was of the order of x5, in good agreement with the theoretical prediction of **Figure 5.13**. In the second case, the enhancement was larger than x5 indicating that the geometry of the pillars has a further enhancing effect on the collection efficiency. Finally, in the last sample the enhancement was less than theoretical but still significant. It is possible for the light coming out of the cavity to be better confined in the collection direction so that the losses coming from the refractive index difference, compare to the other cases, to be smaller compared to the other no-cavity cases.

## 5.5 Conclusions

In this chapter of prospective work, the effect of external electric field on single solution-processable perovskite NCs was studied and a new way to increase the

collection efficiency of the quantum emitter was tested. Quantum confined stark effect was found insignificant in our case of $CsPbBr_3$ NCs, implying that there is probably an efficient screening mechanism that cancels out the applied electric field. More experiments need to be done to explore what is behind this behavior. More specifically, an experiment with a fast AC electric field must be properly designed and realized. The challenge for this is to have a generator that can apply voltage pulses faster than the supposed screening dynamics of the system. Concerning the light collection, it was possible to extract more light from single semiconductor QDs. The geometry of the structure, where the emitter is embedded, plays significant role on the amount of enhancement that solid immersion lens can offer. Nevertheless, SILs are easy to use, requiring no further sample processing, and when choosing the right refractive index of lens, it is possible to extract more light from various semiconductor nanostructures, making this strategy ideal for applications where the amount of collected light is important.

# References


1. Park, Y. S., Guo, S., Makarov, N. S. & Klimov, V. I. Room Temperature Single-Photon Emission from Individual Perovskite Quantum Dots. *ACS Nano* **9**, 10386–10393 (2015).
2. Rainoì, G. *et al.* Single Cesium Lead Halide Perovskite Nanocrystals at Low Temperature: Fast Single-Photon Emission, Reduced Blinking, and Exciton Fine Structure. *ACS Nano* **10**, 2485–2490 (2016).
3. Yin, C. *et al.* Bright-Exciton Fine-Structure Splittings in Single Perovskite Nanocrystals. *Phys Rev Lett* **119**, 026401 (2017).
4. Javaux, C. *et al.* Thermal activation of non-radiative Auger recombination in charged colloidal nanocrystals. *Nature Nanotechnology 2013 8:3* **8**, 206–212 (2013).
5. Fu, M. *et al.* Neutral and Charged Exciton Fine Structure in Single Lead Halide Perovskite Nanocrystals Revealed by Magneto-optical Spectroscopy. *Nano Lett* **17**, 2895–2901 (2017).
6. Ramade, J. *et al.* Exciton-phonon coupling in a CsPbBr3 single nanocrystal. *Appl Phys Lett* **112**, 72104 (2018).
7. Becker, M. A. *et al.* Bright triplet excitons in caesium lead halide perovskites. *Nature 2018 553:7687* **553**, 189–193 (2018).
8. Rainò, G. *et al.* Underestimated Effect of a Polymer Matrix on the Light Emission of Single CsPbBr3 Nanocrystals. *Nano Lett* **19**, 3648–3653 (2019).
9. Miller, D. A. B. *et al.* Band-Edge Electroabsorption in Quantum Well Structures: The Quantum-Confined Stark Effect. *Phys Rev Lett* **53**, 2173 (1984).
10. Högele, A. *et al.* Voltage-controlled optics of a quantum dot. *Phys Rev Lett* **93**, 217401 (2004).
11. Empedocles, S. A. & Bawendi, M. G. Quantum-confined stark effect in single cdSe nanocrystallite quantum dots. *Science (1979)* **278**, 2114–2117 (1997).
12. Bennett, A. J. *et al.* Electric-field-induced coherent coupling of the exciton states in a single quantum dot. *Nature Physics 2010 6:12* **6**, 947–950 (2010).
13. Ghali, M., Ohtani, K., Ohno, Y. & Ohno, H. Generation and control of polarization-entangled photons from GaAs island quantum dots by an electric field. *Nature Communications 2012 3:1* **3**, 1–6 (2012).

14. Wang, H. *et al.* On-Demand Semiconductor Source of Entangled Photons Which Simultaneously Has High Fidelity, Efficiency, and Indistinguishability. *Phys Rev Lett* **122**, 113602 (2019).
15. Muller, J. *et al.* Wave function engineering in elongated semiconductor nanocrystals with heterogeneous carrier confinement. *Nano Lett* **5**, 2043–2049 (2005).
16. Vietmeyer, F., Tchelidze, T., Tsou, V., Janko, B. & Kuno, M. Electric field-induced emission enhancement and modulation in individual cdse nanowires. *ACS Nano* **6**, 9133–9140 (2012).
17. Achtstein, A. W. *et al.* Electroabsorption by 0D, 1D, and 2D nanocrystals: A comparative study of CdSe colloidal quantum dots, nanorods, and nanoplatelets. *ACS Nano* **8**, 7678–7686 (2014).
18. Scott, R. *et al.* Time-Resolved Stark Spectroscopy in CdSe Nanoplatelets: Exciton Binding Energy, Polarizability, and Field-Dependent Radiative Rates. *Nano Lett* **16**, 6576–6583 (2016).
19. Rothenberg, E., Kazes, M., Shaviv, E. & Banin, U. Electric field induced switching of the fluorescence of single semiconductor quantum rods. *Nano Lett* **5**, 1581–1586 (2005).
20. Becker, K. *et al.* Electrical control of Förster energy transfer. *Nature Materials 2006 5:10* **5**, 777–781 (2006).
21. Steinberg, H. *et al.* Electrical current switching in single CdSe nanorods. *Nano Lett* **10**, 2416–2420 (2010).
22. Park, K., Deutsch, Z., Li, J. J., Oron, D. & Weiss, S. Single molecule quantum-confined Stark effect measurements of semiconductor nanoparticles at room temperature. *ACS Nano* **6**, 10013–10023 (2012).
23. Kraus, R. M. *et al.* Room-temperature exciton storage in elongated semiconductor nanocrystals. *Phys Rev Lett* **98**, 017401 (2007).
24. Rowland, C. E. *et al.* Electric Field Modulation of Semiconductor Quantum Dot Photoluminescence: Insights into the Design of Robust Voltage-Sensitive Cellular Imaging Probes. *Nano Lett* **15**, 6848–6854 (2015).
25. Protesescu, L. *et al.* Nanocrystals of Cesium Lead Halide Perovskites (CsPbX3, X = Cl, Br, and I): Novel Optoelectronic Materials Showing Bright Emission with Wide Color Gamut. *Nano Lett* **15**, 3692–3696 (2015).

26. Sharma, D. K., Hirata, S. & Vacha, M. Single-particle electroluminescence of CsPbBr3 perovskite nanocrystals reveals particle-selective recombination and blinking as key efficiency factors. *Nature Communications 2019 10:1* **10**, 1–9 (2019).
27. Lv, B. *et al.* Probing Permanent Dipole Moments and Removing Exciton Fine Structures in Single Perovskite Nanocrystals by an Electric Field. *Phys Rev Lett* **126**, 197403 (2021).
28. Sharma, D. K., Hirata, S., Biju, V. & Vacha, M. Stark Effect and Environment-Induced Modulation of Emission in Single Halide Perovskite Nanocrystals. *ACS Nano* **13**, 624–632 (2019).
29. Protesescu, L. *et al.* Nanocrystals of Cesium Lead Halide Perovskites (CsPbX3, X = Cl, Br, and I): Novel Optoelectronic Materials Showing Bright Emission with Wide Color Gamut. *Nano Lett* **15**, 3692–3696 (2015).
30. Bodnarchuk, M. I. *et al.* Rationalizing and Controlling the Surface Structure and Electronic Passivation of Cesium Lead Halide Nanocrystals. *ACS Energy Lett* **4**, 63–74 (2019).
31. Yuan, G. *et al.* The Degradation and Blinking of Single CsPbI3 Perovskite Quantum Dots. *Journal of Physical Chemistry C* **122**, 13407–13415 (2018).
32. Swarnkar, A. *et al.* Colloidal CsPbBr3 Perovskite Nanocrystals: Luminescence beyond Traditional Quantum Dots. *Angewandte Chemie International Edition* **54**, 15424–15428 (2015).
33. Gao, M. *et al.* Controlled synthesis and photostability of blue emitting Cs3Bi2Br9 perovskite nanocrystals by employing weak polar solvents at room temperature. *J Mater Chem C Mater* **7**, 3688–3695 (2019).
34. Ramade, J. *et al.* Exciton-phonon coupling in a CsPbBr3 single nanocrystal. *Appl Phys Lett* **112**, (2018).
35. Debye, P. & Bueche, F. The dielectric constant of polystyrene solutions. *Journal of Physical and Colloid Chemistry* **55**, 235–238 (1951).
36. Schneider, C. *et al.* Single Semiconductor Quantum Dots in Microcavities: Bright sources of indistinguishable Photons. 343–361 (2015) doi:10.1007/978-3-319-19231-4_13.
37. Liu, S. *et al.* Dual-resonance enhanced quantum light-matter interactions in deterministically coupled quantum-dot-micropillars. *Light Sci Appl* **10**, (2021).

38. Barnes, W. L. *et al.* Solid-state single photon sources: light collection strategies. *The European Physical Journal D - Atomic, Molecular, Optical and Plasma Physics 2002 18:2* **18**, 197–210 (2002).

# 6 Conclusions and Future perspectives

One of the main advantages of InAs QDs, grown along a polar direction such as (211)B, is the internal piezoelectric field they carry, which proved to be crucial for single photon emission at high temperatures, as it produces large X-XX splittings, a necessary condition for high temperature operation. This trait along with the use of enhanced barriers in the form of short-period superlattices to strongly confine the carriers in the dots, improved drastically the temperature stability of the QD emission by preventing the carriers from escaping into the wetting layer. A record-high single photon operation was achieved at 230K, a temperature that can be easily provided by relatively inexpensive thermoelectric coolers. In the strongly confined QDs, an counterintuitive finding was that the biexciton and trion lines appeared to be redshifted with respect to the exciton line. The multi-exciton lines were carefully identified and their unexpected line sequence was attributed to exchange correlation effects, enhanced by the strong confinement situation. This strong confinement mechanism represents an appealing way to control the transition energies of QD multi-excitons by appropriate engineering of the surrounding barriers, not only in the (211)B case, but in any crystallographic orientation including the (100) InAs QD system. Finally, the plasmon-emitter interaction between a core-shell nanowire and a gold surface was studied as a function of their relative distance. We showed that by transferring free-standing nanowires on relatively flat gold surfaces, the overall photoluminescence efficiency and recombination dynamics of the nanowires is drastically changed, leading to an increased photoluminescence intensity and reduced lifetimes, suggesting that plasmons can be utilized to manipulate to our advantage, the emitter properties of semiconductor nanowires, with possible applications to single photon emitters. As a prospective work, the Quantum-Confined Stark effect on single solution-processed $CsPbBr_3$ perovskite nanocrystals was studied and was found insignificant. Finally, a simple method to increase the collection efficiency of a quantum emitter by a factor of 2 to 6, using a solid-immersion lens, was demonstrated.

As future work, based on our experimental findings, we would like to mention the following directions. The first direction would be to push the operating temperature of (211)B InAs QDs to room temperature. This is quite feasible, considering that the above QD system is capable, with minor modifications, of single-photon emission at

higher temperatures than 230 K. The main parameters controlling the operating temperature are the average Al-composition in the barriers, the X-XX splitting in the dot and the position of the cavity mode. If for example, the cavity mode in the main sample studied in Chapter 2, was shifted to longer wavelengths by merely 50 nm, room temperature operation would already be achievable. The second direction would be to apply strong-confinement in (100) InAs/GaAs QDs, in view of obtaining large XX-X splittings, and thus, the possibility for high-temperature single-photon emission in a QD system which is more appealing and acceptable for industrial applications. A third direction would be to theoretically understand and model the plasmonic enhancement in the metal/semiconductor nanowire system and to find ways to design an experiment where the distance of a single nanowire from a metallic surface would be precisely controlled. This way it would be no longer necessary to make statistical measurements on a large number of nanowires and it would be much easier to interpret the results without worrying about the inhomogeneous characteristics of the nanowire ensemble.